J. Astrophys. Astr. (2003) **24,** 1

Editorial

This issue of the *Journal of Astrophysics and Astronomy* (JAA) marks the entry of a new Editorial Board. Prof. G. Srinivasan, who had served as Editor from January 1992, handed over charge at the beginning of 2003. This is the right place to express appreciation of his untiring efforts to sustain the journal over a long period. One new feature which we hope will make the journal more attractive to contributors as well as readers, namely availability of the full article on the Academy website (*www.ias.ac.in/jaa*) and the website of the Astrophysics Data System (ADS), is the outcome of efforts in his tenure. I would like to thank the distinguished astronomers who served on the previous Editorial Board, and hope that we can continue to count on their interest and participation in matters related to the JAA.

Readers will notice both continuity and change in the composition of the new Editorial Board. Astronomy remains the most international in spirit of the sciences, in terms of contacts between individuals and co-operation, direct or via the IAU, between institutions and between nations. It was gratifying that colleagues from many countries agreed to serve on the Editorial Board, as they indeed have in the past. The Board also reflects the growing strength and maturity of the astronomy community in India, when compared to 1980, when the journal was started. This community is of course still small, when compared to that in other subjects in the country. This is one, but not the only, reason for the small current inflow of articles into the journal, which continues to be a matter of concern.

Given the problem of small size, it is worth going over some of the reasons why the **Indian Academy of Sciences** continues to encourage us at JAA. Like the Academy physics journal, *Pramana*, JAA has brought out special issues and covered conferences which are of special interest to readers in India. It has attracted articles describing in detail new facilities and instrumentation developed in the country. It is hoped that the results obtained with some of these new facilities, such as the GMRT (the Giant Metrewave Radio Telescope), and the HCT (Himalayan Chandra Telescope), will also find their way to JAA.

With the wide use of the e-print archive, an article becomes accessible to the worldwide community, and its search engines, irrespective of the journal in which it finally appears. In this situation, JAA can provide an attractive option which at its best can reduce delay (and page charges!) while retaining visibility and serious refereeing. A by-product of sustaining this option is the growth of a peer group via the process of refereeing and other editorial activities – a group not necessarily confined to India. Any healthy journal is the nucleus of an invisible college of a kind that is relevant to astronomy, with its unique global character. And especially in astronomy, a certain diversity is needed “ . . . lest one good custom should corrupt the world”. I look forward to working with authors, referees, colleagues on the Editorial Board, and readers, to help JAA find its place in the stars.

Rajaram Nityananda
Editor

J. Astrophys. Astr. (2003) **24,** 3–10

Is the Age Problem Resolved?

Ali Akbar Navabi[1] & Nematollah Riazi[2]
[1]*Institute for Advanced Studies in Basic Sciences, Zanjan, Iran.*
[2]*Physics Department and Biruni Observatory, Shiraz University, Shiraz 71454, Iran,*
and *IPM, Farmanieh, Tehran, Iran.*
email: riazi@physics.susc.ac.ir

Received 2001 October 8; accepted 2003 January 16

Abstract. The cosmological, astrophysical, and nucleocosmochronological methods for estimating the age of the universe and the corresponding uncertainties are comparatively studied in the present paper. We are led to the conclusion that the new measurements of cosmological parameters, and the recent estimates of the age of globular clusters have led to the gradual disappearance of the age problem from the arena of modern cosmology.

Key words. Cosmology: age of the universe, cosmological parameters.

1. Introduction

Three main streams of research seem to have converged to consistent estimates of the age of the universe within the corresponding uncertainties. First, recent observational measurements of matter density parameter give (Coles & Ellis 1994):

$$\Omega_m = 0.1 - 0.4. \tag{1}$$

This range epitomizes the result of a variety of methods for calculating Ω_m, as reviewed by Coles & Ellis (1994). These include gravitational lensing, galaxy clustering observations, measurements of the peculiar velocities of galaxies, and dipole analysis of cosmic background radiation. Secondly, the recent Boomerang experiment provides us with (deBernandis *et al.* 2000):

$$0.88 < \Omega_o < 1.12, \tag{2}$$

where $\Omega_o = \Omega_m + \Omega_\Lambda$, and Ω_Λ is the vacuum energy density parameter related to the cosmological constant, Λ , by $\Omega_\lambda = \frac{\Lambda c^2}{3H_o^2}$. Since $\Omega_o = 1$ corresponds to a flat universe, the Boomerang experiment shows the flatness of the universe to a fairly good degree of accuracy. Thirdly, the Hipparcos parallax catalog, together with other techniques (Chaboyer *et al.* 1998), indicates that globular clusters are farther away than previously believed, implying a reduction in the age estimates. Moreover, studies of high redshift supernovae have led to a non-vanishing cosmological constant, which affects the cosmological age estimates. In the following sections we discuss these issues in more detail.

2. Cosmological estimates of the age of the universe

In the context of current cosmological theory, which is based on the validity of the cosmological principle, the cosmic time elapsed since the big bang singularity is approximately given by (Riazi 1991):

$$\tau_c = \frac{1}{H_o} \int_o^1 \frac{\sqrt{r} dr}{\sqrt{\Omega_m + (1 - \Omega_m - \Omega_\Lambda) r + \Omega_\Lambda r^3}}. \tag{3}$$

This equation involves an approximation, because it is the result of integration of the Friedmann's equations after recombination (i.e., by neglecting the quantum and radiation dominated era). The approximation holds because the value which the integral assumes by the insertion of customary values of H_o, Ω_m, and Ω_Λ in the above integral is considerably larger than the Planck time (10^{-43}s) and the age of the early universe before recombination ($\simeq 10^5$ yr). Setting aside the logical and physical controversies underlying the conception of a beginning for the universe, and ignoring our lack of knowledge as to what happened to the universe during the Planck era, when a quantum theory of gravity predominated, modern cosmologists have come to call τ_c "the age of the universe". According to equations (1) and (2), the energy density of vacuum has had a paramount role in the evolution of the universe. This leads, according to equation (3), to a considerable increase of the age of the universe as compared to the age of a flat universe without a cosmological constant (which is 8.6 Gyr for $H_o = 75\,\mathrm{kms}^{-1}\mathrm{Mpc}^{-1}$). The matter density parameter can be decomposed according to

$$\Omega_m = \Omega_b + \Omega_{cdm} + \Omega_{hdm}, \tag{4}$$

where Ω_b, Ω_{cdm}, and Ω_{hdm} denote the density parameter of baryonic matter, cold dark matter, and hot dark matter, respectively. Assuming the existence of hot dark matter and a flat universe for which $\Omega_o = 1$, Novosyadlyj and his coworkers (2000) have recently embarked on a thoroughgoing statistical analysis of cosmological parameters on the basis of a wide set of observational data including the Abell-ACO cluster power spectrum and mass function, peculiar velocities of galaxies, the distribution of $Ly - \alpha$ clouds, and CMB temperature fluctuations. Using a χ^2 minimization method, Novosyadlyj *et al.* (2000) argue that the cosmological parameters which match observational data best are

$$\begin{aligned} h_o &= H_o/100 = 0.70 \pm 0.12 \text{ km s}^{-1} \text{ Mpc}^{-1}, \\ \Omega_m &= 0.41 \pm 0.11 \;\; (\Omega_\Lambda = 0.59 \pm 0.11), \\ \Omega_{cdm} &= 0.31 \pm 0.15, \;\; \Omega_{hdm} = 0.059 \pm 0.028, \end{aligned}$$

and

$$\Omega_b = 0.039 \pm 0.014.$$

In each of these equalities, the first number indicates the most probable value and the second number is the corresponding standard error. For $\Omega_o = 1$, the cosmological age integral reduces to

$$\tau_c = \frac{2}{3 H_o \Omega_\Lambda^{1/2}} \sinh^{-1} \left(\frac{\Omega_\Lambda}{\Omega_m} \right)^{1/2}, \tag{5}$$

which by insertion of the data obtained by Novosyadlyj *et al.* leads to

$$\tau_c = 12.3\,\mathrm{Gyr}. \tag{6}$$

According to a well known theorem in the theory of errors (Barford 1995), the standard error of $z = f(x, y, ...)$ is related to the standard errors of $x, y, ...$ according to

$$S(z) = \left[\left(\frac{\partial f}{\partial x}\right)^2_{x=x_o, y=y_o, ...} S^2(x) + \left(\frac{\partial f}{\partial y}\right)^2_{x=x_o, y=y_o, ...} S^2(y) + ... \right]^{1/2}. \tag{7}$$

Hence, if we rewrite (5) by using $\Omega_o = 1$ as

$$\tau_c = \frac{2}{3H_o\Omega_\Lambda^{1/2}} \sinh^{-1}\left(\frac{\Omega_\Lambda}{1-\Omega_\Lambda}\right)^{1/2}, \tag{8}$$

then, based on Novosyadlyj's data,

$$\frac{\partial\tau_c}{\partial H_o} = -\frac{2}{3H_o^2\Omega_\Lambda^{1/2}} \sinh^{-1}\left(\frac{\Omega_\Lambda}{1-\Omega_\Lambda}\right)^{1/2} = -172.8\ \mathrm{Gyr}^2, \tag{9}$$

and

$$\frac{\partial\tau_c}{\partial\Omega_\Lambda} = -\frac{1}{3H_o\Omega_\Lambda}\left[\frac{1}{(1-\Omega_\Lambda)^{1/2}(2\Omega_\Lambda^2 - 2\Omega_\lambda + 1)^{1/2}} - \frac{1}{\Omega_\Lambda^{1/2}} \sinh^{-1}\left(\frac{\Omega_\Lambda}{1-\Omega_\Lambda}\right)^{1/2}\right] = 6.73\ \mathrm{Gyr}. \tag{10}$$

Thus, finally,

$$\tau_c = 12.3 \pm 2.2\ \mathrm{Gyr}. \tag{11}$$

There is a justification for using Novosyadlyj's data as a prototype for the values of cosmological parameters: firstly, the assumption $\Omega_o = 1$ is well corroborated by the Boomerang experiment and the prediction of the inflationary models. Secondly, the analysis is based on a comprehensive set of observational data. Thirdly, the most probable value of Ω_m which ensues from the analysis lies within the range of variation of Ω_m as given by equation (1). Fourthly, the average value of Ω_m which results from equation (1) lies within the range of variation of Ω_m as given by Novosyadlyj. Finally, Novosyadlyj's value for h_o is consistent with the value newly obtained by the Hubble Space Telescope: $h_o = 0.71 \pm 0.06\ \mathrm{kms}^{-1}\mathrm{Mpc}^{-1}$ (Mould *et al.* 2000).

3. Astrophysical estimates of the age of the universe

It was first suggested by Peebles & Dicke (1968) that the globular clusters have about the same mass as the Jeans's mass at recombination. They are thus considered as the successors of the first generation of gravitationally bound systems formed in the early universe. On this basis, they are reckoned as the oldest structures in the universe, the age of which gives the most stringent lower limit on the age of the universe. The most comprehensive statistical analysis of the effect of systematic errors included in the age estimation of globular clusters is the Monte Carlo analysis of Chaboyer *et al.* (1996a, 1996b, 1996c). Owing to the essential dependence of the analysis on the techniques of distance estimation, their analysis underwent a revision with the release of the Hipparcos catalogue for field subdwarf parallaxes, which via the main sequence fitting method, leads to a higher estimate for the distance of globular clusters and thus, a lower estimate for their age. Chaboyer *et al.*'s (1998) final result for the age of seventeen of the oldest clusters in our galaxy is

$$\tau_{gc} = 11.5 \pm 1.3\ \text{Gyr}. \tag{12}$$

Chaboyer *et al.* (1998) are among five different research groups which used the Hipparcos database for this purpose: Reid (1997, 1998); Gratton *et al.* (1997); Grundahl *et al.* (1998); Pont *et al.* (1998); and Chaboyer *et al.* (1998). Based on a sample of five globular clusters, Reid's analysis of 1998 leads to "age estimates of no more than 11 Gyr for any of the clusters included in the sample". Pont *et al.* (1998) report an age near 14 Gyr for M92 but their method mainly depends on the agreement between the shapes of the theoretical isochrones and the data near the turnoff and it overlooks the uncertainties due to convection and helium diffusion. From a fit to the main sequence of metal poor subdwarfs with Hipparcos parallaxes, Grandahl *et al.* (1998) derive an age near 12 Gyr for M13, assuming $[\mathrm{Fe/H}] = -1.61$ and $[\alpha/\mathrm{Fe}] = 0.3$. Gratton *et al.* (1997) based their former analysis on main sequence fitting for main clusters, six of which are included among Reid's (1997) analysis. In a revision of this work, Carretta, Gratton, and their co-workers (2000) have recently reported the age

$$\tau_{gc} = 12.9 \pm 2.9\ \text{Gyr}, \tag{13}$$

for galactic globular clusters, by a reconciliation of short and long distance scales to the Large Magellanic Cloud (Carretta *et al.* 2000). To make our comparison exhaustive, we must also mention the analysis of Salaris & Weiss (1997), who applied a combination of Iben's method and a method based on the color difference between the turnoff and the base of the red giant branch to a sample of twenty five clusters. They concluded

$$\tau_{gc} = 11.8 \pm 0.9\ \text{Gyr}, \tag{14}$$

or,

$$\tau_{gc} = 12.3 \pm 2.9\ \text{Gyr} \tag{15}$$

if the clusters Arp 2 and Rup 106 are not included in the sample. We must further point, in passing, to the idiosyncratic method of Jimenez (1996), who by using the horizontal branch morphology for a sample containing eight clusters, has come up with the final result

$$\tau_{gc} = 13.5 \pm 2\ \text{Gyr}. \tag{16}$$

According to Peebles & Dicke (1968), "the globular clusters formed (as gas clouds) before the galaxies appeared". However, what is meant by "age" in the above result is the time elapsed since the stars in the cluster became mature enough to start their main sequence life. Multiple observational evidence (Sandage 1993), together with the theories of galaxy formation (Coles & Lucchin 1997), point to the fact that the time of maturity of galaxy components corresponds to a redshift as high as $z_{pg} \simeq 10$, where pg denotes a protogalaxy. This leads, by a simple calculation similar to the one in section 2, to the "age" of a protogalaxy elapsed since the big bang singularity

$$\tau_{pg} = 0.4 \pm 0.07 \text{ Gyr}. \tag{17}$$

Combining this with the astrophysical estimates of globular cluster ages gives the astrophysical estimates of the age of the universe

$$\tau_A = \tau_{pg} + \tau_{gc}. \tag{18}$$

A problem now arises: How can we combine different astrophysical estimates of the age of the universe? Since the error of τ_A encompasses both statistical and systematic errors, the statistical combination of different astrophysical estimates of the age of the universe seems to be illegitimate. The only path open is to consider each single τ_A in its own right.

4. Nucleocosmochronology

Nucleocosmochronology derives the time-scales for the nucleosynthesis of solar system elements from the abundance and production ratios of radioactive nuclides and from a model for the chemical evolution of the Galaxy. Both of these sources of knowledge, are nevertheless also sources of ignorance, for they give rise to considerable uncertainties in the age determinations. Fowler & Hoyle (1960) first derived an age of the order of 15 Gyr for the Galaxy, by using an exponentially decaying model for the chemical evolution. Schramm & Wassenberg's (1970) research was original, in that it involved a calculation of the mean age of r-process elements independently of the model for the chemical evolution of the Galaxy. This mean age provides a lower limit for the Galactic age. Meyer & Schramm's (1986) quest for a lower and upper limit on the age of the galaxy which are independent of both the evolution function of the galaxy and the uncertainties in cosmochronological input data culminated in

$$8.9 \text{ Gyr} \le \tau_g \le 28.1 \text{ Gyr} \tag{19}$$

which, in view of some questions about β-delayed fission, some uncertainties in the decay rate of ^{187}Re caused by thermal resonance, and discussions about the Th/Nd abundance in stars, was changed into (Schramm *et al.* 1996):

$$9.6 \text{ Gyr} \le \tau_g \le 28.1 \text{ Gyr}. \tag{20}$$

The zero of time in the above estimates of the age of the Galaxy is the time when the first generation stars in the Galaxy became mature enough to start their nucleosynthesis. By combining (20) and (17) we thus arrive at the nucleocosmochronological estimate of the age of the universe

$$\tau_N = 19.3 \pm 9.3 \text{ Gyr}. \tag{21}$$

Recent spectral studies of the star CS31082-001 in the Galactic halo, in which an ionized uranium transition was detected, led to the simultaneous determination of the abundances of thorium and uranium, enabling the authors to obtain more accurate age estimates (Cayrel *et al.* 2001).

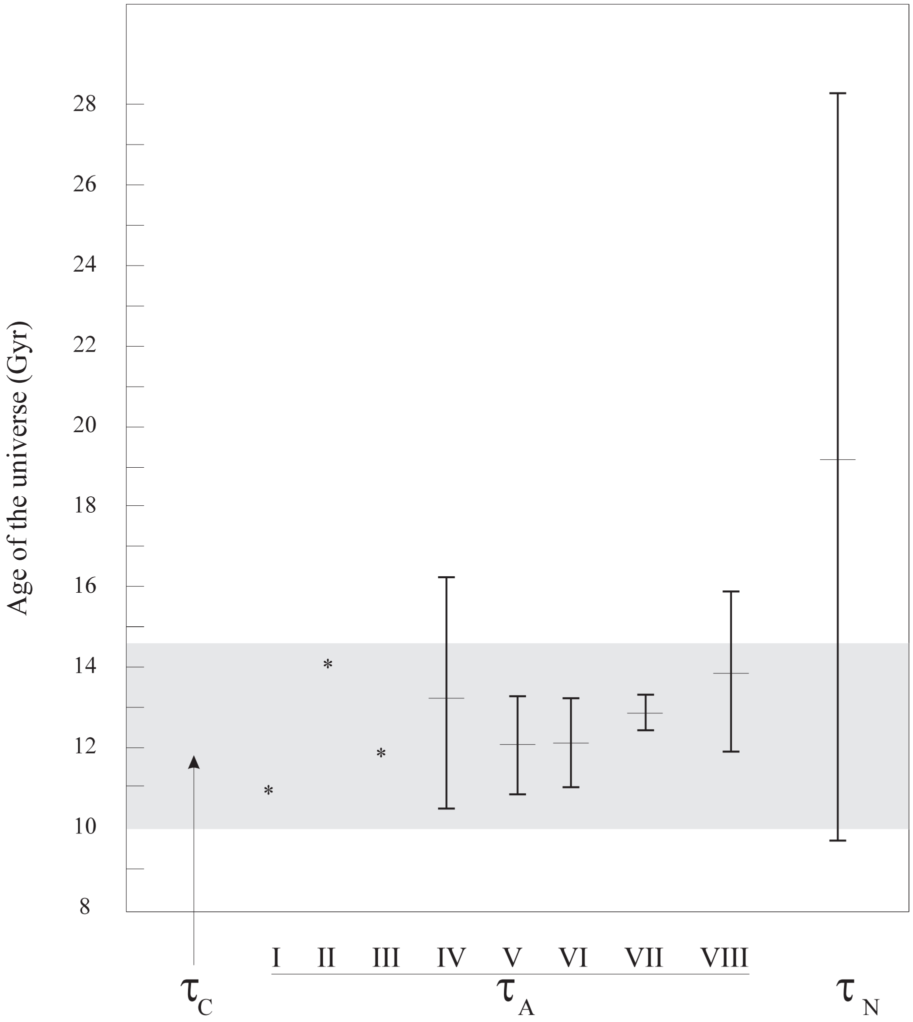

Figure 1. Comparison between different estimates of the age of the universe. References: **I:** Reid (1998), **II:** Pont *et al.* (1998), **III:** Grundahl *et al.* (1998), **IV:** Gratton *et al.* (1997), **V:** Chaboyer *et al.* (1998), **VI:** Salaris & Weiss (1997), Rup 106 and Arp 2 excluded, **VII:** Salaris & Weiss (1997), Rup 106 and Arp 2 included, **VIII:** Jimenez *et al.* (1996).

5. Discussion and conclusion

The results mentioned in the previous sections may be brought together using the diagram illustrated in Fig. 1. We refrain from a statistical combination of astrophysical estimates, the justification for which was given in section 3. The shaded area in the diagram corresponds to the plausible range of the cosmological age estimates based on Novosyadlyj's data as a prototype. An argument in favor of choosing Novasyadlyj's data as a prototype was given in section 2. Finally, the nucleocosmochronological result of Meyer and Schramm given by equation (21) is depicted in the diagram, as an archetype of a host of nucleocosmochronological ages with broad error ranges (Clayton 1996). Due to these broad ranges of error, the nucleocosmochronological ages defy any useful comparison with the astrophysical and cosmological age, but a plausible comparison between the astrophysical estimates and the cosmological estimate seems to be possible. Let us define the range of variation of τ_A and τ_c as

$$R_{\tau_A} \equiv \left[\tau_{A,O} - E_{\tau_A}, \tau_{A,O} + E(\tau_A)\right], \tag{22}$$

and

$$R_{\tau_C} \equiv \left[\tau_{C,O} - E_{\tau_C}, \tau_{C,O} + E(\tau_C)\right], \tag{23}$$

where O and E denote the most probable value and the corresponding error respectively. The diagram in Fig. 1 then shows clearly that

$$\tau_{A,O} \in R_{\tau_C}, \tag{24}$$

and

$$\tau_{C,O} \in R_{\tau_A}. \tag{25}$$

The above two relations authenticate the consistency of the cosmological and astrophysical estimates of the age of the universe within the range of the corresponding errors and substantiate the claim that modern observational and theoretical techniques are leading to the gradual disappearance of the longstanding age problem from the scene of cosmological debates. However, in spite of its plausible appearance, we should take this final result with some scruples as to the fundamentals of the cosmological theory within which this final conclusion is arrived at. To take the cosmological principle first, the wonderful discovery of the Great Wall in the late eighties has cast a shadow of doubt on the validity of this principle. It is possible to redeem the principle by posing the existence of non-baryonic dark matter, which may remedy the inhomogeneity betrayed by the Great Wall or other very large-scale structures, by a disguised homogeneity. Nevertheless, the existence of non-baryonic dark matter in itself is amenable to criticism, for the simple reason that, except for the massive neutrinos in the recent Super-Kamiokande and Sudbury experiments (Fukuda *et al.* 1998) which is still open to doubt, none of the exotic elementary particles proposed as candidates for non-baryonic matter have been detected yet. Secondly, our analysis was entirely based on the validity of the general theory of relativity. It may turn out that a more fundamental theory (such as the string theory or non-commutative geometry) will provide a better framework for doing cosmological calculations. The solution of the age problem has thus been accomplished within the context of the big bang model and not by a critical analysis of the model itself. The big bang model, whatever it may be, is not the final theory of the universe, and like every scientific theory, is susceptible of a fundamental criticism.

References

Barford, N. C. 1995, *Experimental Measurements: Precision, Error, and Truth* (John Wiley and Sons) p. 43.

Carretta, E., Gratton, R. G., Clementini, G., Pecci, F. F. 2000, *Astrophys. J.,* **535,** 215.

Chaboyer, B. Demarque, P. Kernan, P. J., Krauss, L. M. 1998, *Astrophys. J.,* **494,** 96.

Chaboyer, B., Demarque, K., Kernan, P. J., Krauss, L. M. 1996a, *Science,* **271,** 957.

Chaboyer, B. *et al.* 1996b, *Mon. Not. R. Astr. Soc.,* **283,** 683.

Chaboyer, B. Demarque, K., Sarajedini, A. 1996c, *Astrophys. J.*. **459,** 558.

Clayton, D. D. 1996, in *Astronomy and Astrophysics Encyclopedia*, Stephan P. Martan (ed.), (Cambridge University Press) p. 156.

Coles, P., Ellis, G. 1994, *Nature*, **370,** 609.

Coles, P., Lucchin, F. 1997, *Cosmology*, (John Wiley and Sons) pp. 426–431.

deBernandis, P. *et al.*, *Nature*, **404,** 955, 2000.

Fowler, W. A., Hoyle, F. 1960, *Ann. Phys.*, **10,** 280.

Fukuda, Y. *et al.* 1998, *Phys. Rev. Lett.*, **81,** 1562.

Grundahl, F., VandenBerg, D. A., Anderson, M. 1998, *Astrophys. J.*, **500,** L179.

Gratton *et al.*, R. G. 1997, *Astrophys. J.*, **491,** 749.

Jimenez, R. *et al.* 1996, astro-ph/9602132.

Meyer, B. S., Schramm, D. N. 1986, *Astrophys. J.*, **311,** 406.

Mould, T.R., *et al.* 2000, *Astrophys. J.*, **529,** 786.

Novosyadlyj, B. *et al.*, 2000, *Astron. Astrophys.*, **356,** 418.

Peebles, P. J. E., Dicke, R. H. 1968, *Astrophys. J.*, **154,** 891.

Pont, F., Mayor, M., Turon, C., VandenBerg, D. A. 1998, *Astron. Astrophys.*, **329,** 87.

Riazi, N., 1991, *Mon. Not. R. Astr. Soc.*, **248,** 555.

Reid, I. N., 1997, *Astron. J.*, **114,** 161.

Reid, I. N. 1998, *Astron. J.*, **115,** 204.

Salaris, M., Weiss, A. 1997, *Astron. Astrophys.*, **327,** 107.

Sandage, A. 1993, *Astron. J.*, **106,** 719.

Schramm, D. N., Copi, C., Shi, X. 1996, in *Proceeding of the Eighth physics Summer School*, B. A. Robson, N. Visvanathan, and W.S. Woolcock (eds), (World Scientific Publishing Company)

Schramm, D. N., Wassenberg, G. J. 1970, *Astrophys. J.*, **162,** 57.

J. Astrophys. Astr. (2003) **24,** 11–21

The Hubble Relation for a Comprehensive Sample of QSOs

D. Basu *Department of Physics, Carleton University, Ottawa, ON K1S 5B6, Canada.*
e-mail: basu@physics.carleton.ca

Received 2002 December 11; accepted 2003 May 31

Abstract. A correlation between redshifts (z) and apparent magnitudes (V) (Hubble relation) of Quasi Stellar Objects (QSOs) has long been sought. Such a correlation exists for galaxies whose redshifts are of cosmological origin. However, a plot of the two quantities representing the Hubble diagram for QSOs exhibits, in general, a wild scatter. This raises the question whether redshifts of QSOs are cosmological. On the other hand, most luminous QSOs in groups, and subsamples with particular properties, have been reported to show the Hubble relation. In the present paper, we analyse all optically non-variable QSOs in a comprehensive sample. In our analysis we grouped the objects into certain intervals of apparent magnitudes. Correlations obtained between redshifts and magnitudes are all statistically robust. Also, the Hubble relation in the usual form $V = 5\log z + C$ is obeyed very convincingly for QSOs with $V < 19.5$.

Key words. Cosmology—Hubble relation—quasi stellar objects or QSOs—redshifts.

The debate over the origin of redshifts of Quasi Stellar Objects (QSOs) still continues as to whether it is cosmological, intrinsic or both. One of the tests to check the origin is to look for the correlation between their apparent magnitudes and redshifts exhibited by the linearity of a plot of the two quantities. It is known that such plots for galaxies show linearity and a significant correlation. As such a correlation between redshifts (z) and apparent magnitudes (V, m_B, M_v, m_v, B_{AV}, different symbols used by different authors) of QSOs has been sought since a long time. Sandage (1965) was probably the first to attempt a Hubble diagram for 10 QSOs then known between $17.32 < V < 18.21$, that showed "a relatively small scatter about a mean $[m, z]$ line whose equation is $m_B = 5\log z + 18.186$". However, a plot of $(1 + \log z)$ against M_v, between $15 < M_v < 19.5$, for "all quasi-stellar objects and N-type galaxies for which data are available" by Hoyle & Burbidge (1966) demonstrated a large scatter and was inconclusive with no correlation. On the other hand, the analysis by Longair & Scheuer (1967) showed a significant correlation between $\log z$ and m_v for a sample of 75 QSOs ($15.5 < m_v < 19.5$, except 3C 273). Again, a plot of $\log z$ against $\log f(2500)$, $f(2500)$ being the flux density at the emitted frequency 2500 Å, by Schmidt (1968) for 40 3CR QSS exhibited a large scatter with no correlation.

Based on a suggestion by McCrea (1972) "that the brightest quasar at each redshift might have a significant Hubble relation", Bahcall & Hills (1973) analysed 105 QSOs

($m_v < 19.5$). A plot of $\log z$ against m_{2500} for seven of the brightest objects yielded a slope of 5.0. However, a somewhat different analysis of "all QSOs from the list of De Veny *et al.* (1971) for which at least certain photoelectric magnitude is given" ($V < 19.25$), led Burbidge & O'Dell (1973) to obtain a slope of 4.3 for the most luminous, and 3.1 and 3.2 for second and third most luminous QSOs respectively. On the other hand, in a sample of 130 QSOs ($15 < B_{AV} < 19$), brightest objects at each redshift were found by Pica & Smith (1983) "to obey the Hubble's relation quite well when variability is accounted for".

It is known that, in general, QSOs exhibit a wild scatter in plots of apparent magnitudes against redshifts. Nevertheless, subsamples with particular properties of QSOs have exhibited much less scatters and significant correlations. Thus, Setti & Woltjer (1971) demonstrated that the scatter is appreciably reduced when objects with steep radio spectra and extended structures are only plotted. Such an analysis was repeated by Stannard (1973) for 166 QSOs ($15.5 < V < 19$) who found a significant correlation between $\log z$ and V for flat radio spectra QSOs and no correlation for concave radio spectra QSOs. On the other hand, two separate subsamples of QSOs, one exhibiting radio polarization and the other exhibiting optical polarization, have been shown by Basu (1993) to obey the Hubble diagram at high levels of significance.

Any statistically significant correlation between redshifts and optical magnitudes of QSOs has thus been exhibited only by limited samples, by brightest sources, or by particular subsamples. The two main reasons for the lack of correlation in the general sample are attributed to either that the redshifts of these objects are non-cosmological, or that the luminosity functions of QSOs evolve with epochs. Possibility of at least a certain fraction of QSOs being actually blueshifting (Basu & Haque-Copilah 2001) should also be borne in mind in this respect.

However, analyses of possible evolution of luminosity functions of QSOs have so far been performed with non-Λ cosmology. As such, the question remains open as to whether the QSO redshift is of cosmological origin. We were therefore prompted to analyse QSO data with a view to find out any correlation between their redshifts and apparent magnitudes which may throw light on the cosmological origin of redshifts of QSOs. The purpose of the present paper is to report the outcome of an analysis that yields a highly significant correlation between redshifts and apparent magnitudes of QSOs, the sample used being that of Hewitt & Burbidge (1993, HB).

The HB sample is one of the largest collection of QSOs with available information of a wide range of properties. While HB by no means, presents a complete sample, it certainly represents a comprehensive sample. The most important advantage of the HB sample for the present investigation is that it provides information of the optical variability of the objects. For an analysis where the quantity apparent magnitude of the object is one of the only two parameters used, optical variability is an essential property to be taken into account. The significance of this measure is further revealed by the findings in Pica & Smith (1983) mentioned earlier, which clearly shows that optical variability is a significant criterion for studies in the redshift-magnitude relation of QSOs. The other samples that are currently available, e.g., the 2dF or SDSS, may have a relatively larger number of objects, but lack in information on variability, and, as such, are unsuitable for such studies.

The HB sample lists 7315 objects. We eliminated all BL Lac objects, all optically variable QSOs, all QSOs with doubtful redshift values, and were left with 6146 non-variable QSOs with confirmed redshifts. Although somewhat smaller than the 2dF sample or SDSS, this is certainly a huge and statistically meaningful data set. No K-correction or galactic extinction correction has been applied, since these corrections are known to be small for QSOs (Sandage 1966).

Figure 1 shows the apparent magnitude (V) distribution of the sample, at intervals of 0.5 in V, viz., $14.0 \leq V < 14.5$, $14.5 \leq V < 15.0$, etc. Figures 2(a) to 2(c)

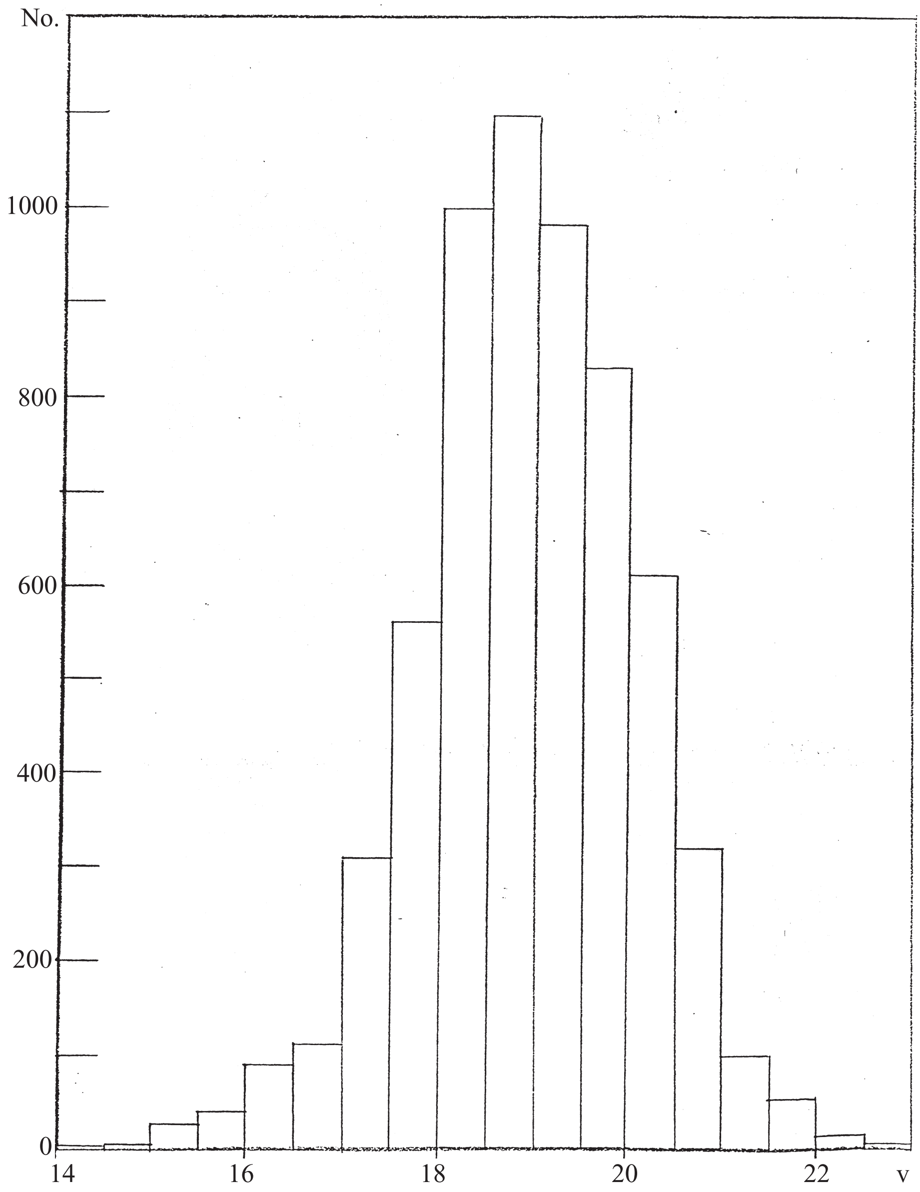

Figure 1. Distribution of apparent magnitudes (V) of non-variable QSOs with confirmed redshifts from Hewitt & Burbidge (1993, HB).

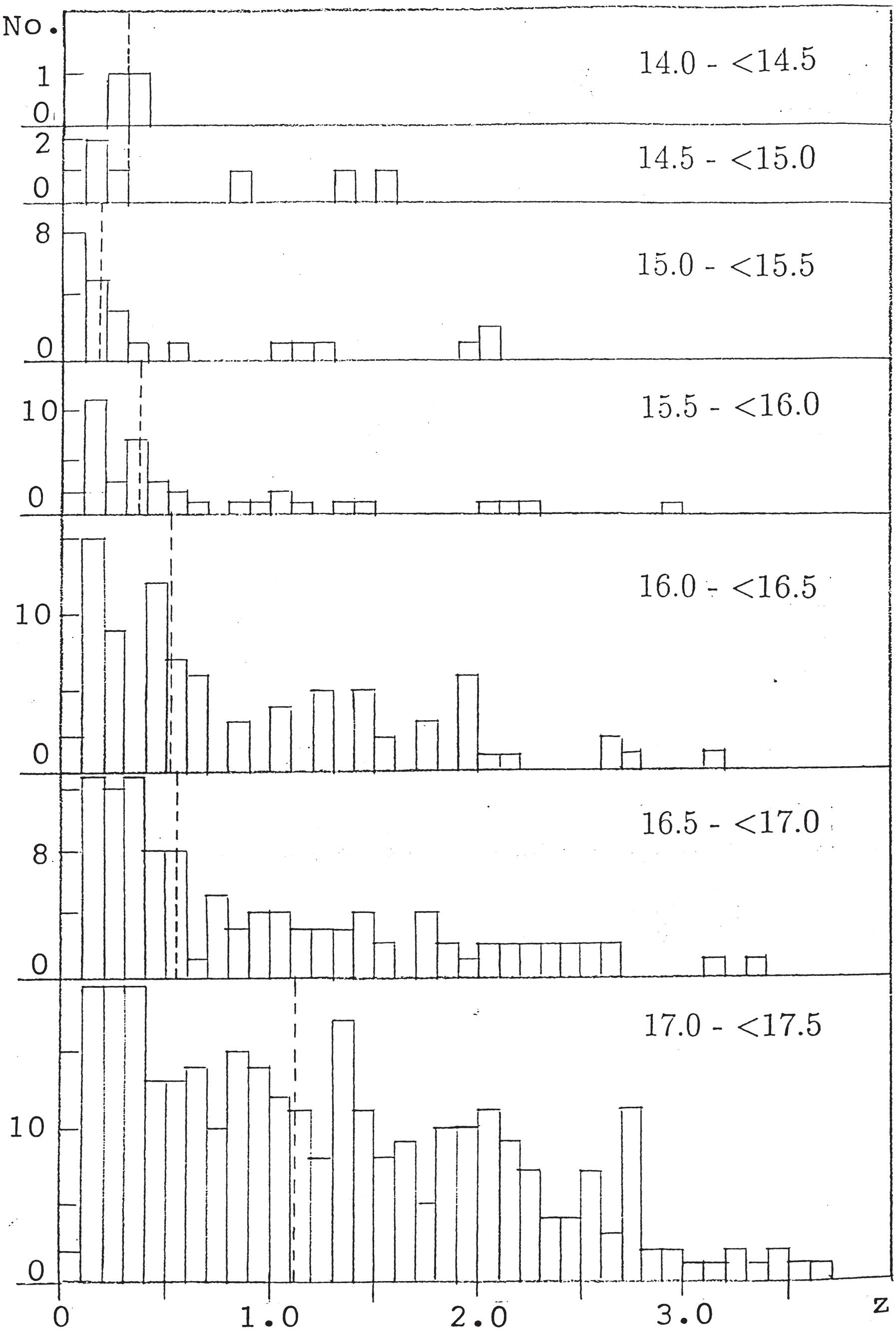

Figure 2(a). Redshift (z) distribution of our sample of QSOs (as in Fig. 1) for the apparent magnitude (V) intervals indicated in each panel. Note that each redshift bin denotes values $0 \leq z < 0.1$, $0.1 \leq z < 0.2$, etc. The dotted line indicates the position of the median ($\tilde{z}$) of the distribution.

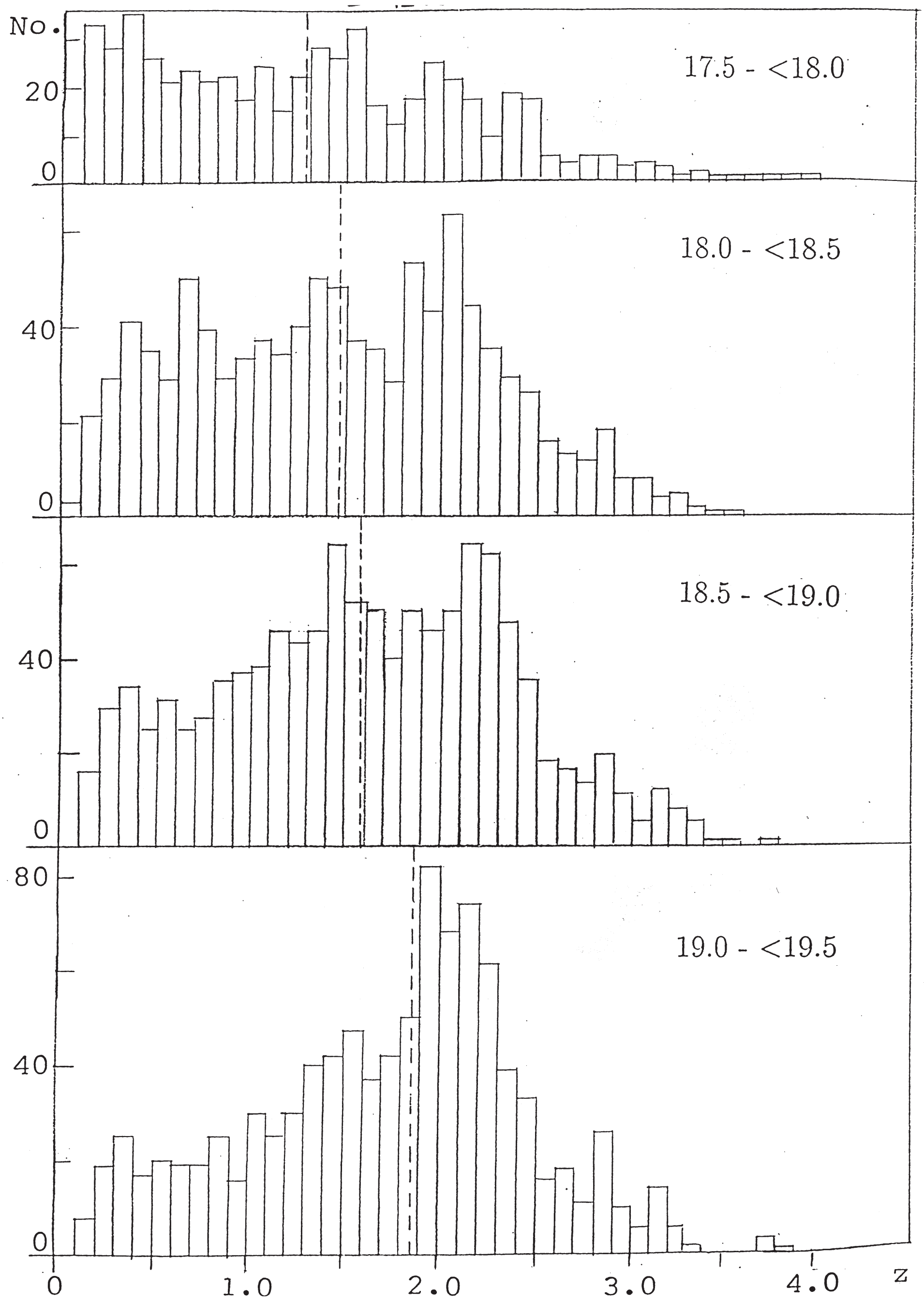

Figure 2(b). Same as in Figure 2(a).

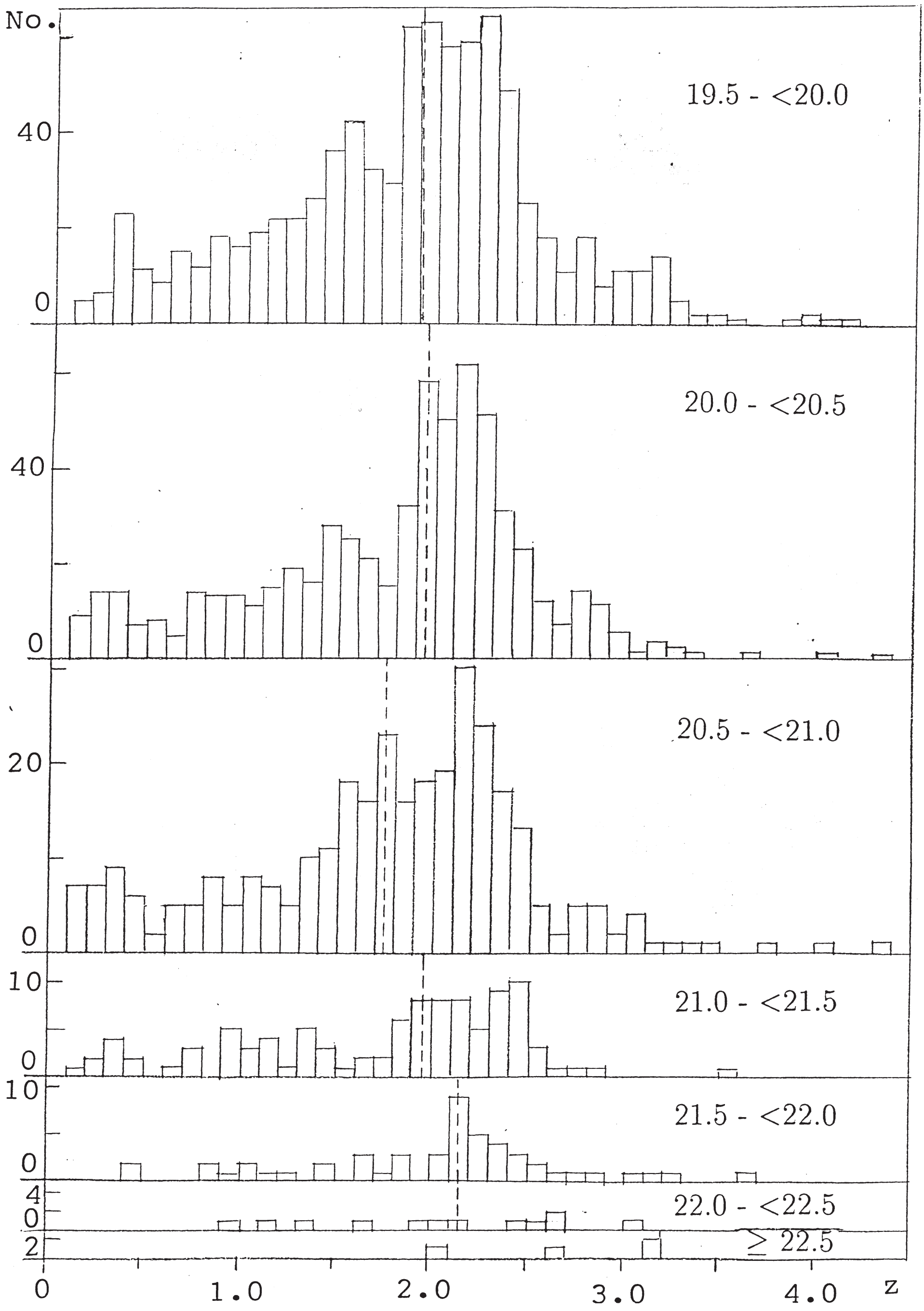

Figure 2(c). Same as in Figure 2(a). One QSO in the bin $4.7 \leq z < 4.8$, V-interval 20-<20.5, is out of scale and not shown.

show the redshift distribution of QSOs in each V-interval at bins $0 < z < 0.1$, $0.1 \leq z < 0.2$, etc. The most striking feature exhibited by Figs. 2(a) to 2(c) is that the distributions are largely asymmetrical or skewed. Moreover, the asymmetry or the skewness changes from positive to negative in the sense that the number of objects increases quite remarkably from lower redshifts to higher redshifts as one proceeds from V-intervals with smaller values of V to V-intervals with larger values of V. This led us to examine the matter further.

The central tendency of a distribution is given by the average value. Among the various measures of the average, the median is a better index of the central tendency than the arithmatic mean in the distributions of Figs. 2 that are largely asymmetrical or skewed. Additional special advantage is that the median is known not to depend on extreme values of the distribution, while the mean cannot be calculated in case of a distribution with open ends. The position of the corresponding median value ($\tilde{z}$) in each distribution is shown in Figs. 2(a) to 2(c). Furthermore, the 95% confidence limits ($\pm c_{95}$), which is a measure of the probability that 95% of the data are collected within these limits, have been calculated by using the formula (Sachs 1984)

$$c_{95} = 1.58(Q_3 - Q_1)/\sqrt{n},$$

where Q_1 and Q_3 are the first and the third quartiles respectively and n is the total number of objects in the distribution.

Table 1 shows the median ($\tilde{z}$) and the confidence limits ($\pm c_{95}$) of the distribution for each V-interval. Table 1 and Figs. 2(a) to 2(c) clearly demonstrate the trend that

Table 1. Median ($\tilde{z}$) and confidence limits ($\pm c_{95}$).

V-interval	$\tilde{z}$	$\pm c_{95}$
14.0-< 14.5	0.3000	0.1117
14.5-< 15.0	0.3000	0.8869
15.0-< 15.5	0.1800	0.1693
15.5-< 16.0	0.3571	0.0287
16.0-< 16.5	0.5214	0.1556
16.5-< 17.0	0.5625	0.1731
17.0-< 17.5	1.1364	0.1244
17.5-< 18.0	1.2795	0.0833
18.0-< 18.5	1.4615	0.0623
18.5-< 19.0	1.5923	0.0759
19.0-< 19.5	1.8590	0.2693
19.5-< 20.0	1.9135	0.0467
20.0-< 20.5	1.9466	0.0545
20.5-< 21.0	1.7469	0.0761
21.0-< 21.5	1.9524	0.1914
21.5-< 22.0	2.1500	0.1600
22.0-< 22.5	2.1500	0.4218
≥ 22.5	3.2000	0.7505

Table 2. Correlation coefficient (r), slope (s) and constant (A).

Range $14.0 \leq V$	r	s	A
< 19.5	0.9429	4.9826	17.6393
< 20.0	0.8432	6.2112	18.1261
< 20.5	0.9428	5.6338	17.8569
< 21.0	0.9303	6.1728	18.0111
< 21.5	0.9232	6.6534	18.1324
< 22.0	0.9196	7.0922	18.2348
< 22.5	0.9194	7.5873	18.3460
≥ 22.5	0.9274	7.8186	18.3776

the quantity $\tilde{z}$ increases with the quantity V in a systematic manner. This led us to pursue the matter in more detail.

We plotted $\log \tilde{z}$ against V_{mp}, where V_{mp} is the mid-point of the corresponding V-interval, viz., $V_{\text{mp}} = 14.25$ for the interval $14.0 \leq V < 14.5$, $V_{\text{mp}} = 14.75$ for the interval $14.5 \leq V < 15.0$, etc. The relationship was found to be linear. We therefore computed the correlation coefficient (r) between $\log \tilde{z}$ and V_{mp}, and the equation of the best fitting least square regression line for the linear relation for all the individual V-ranges, viz., between $V = 14.0$ and $V < 19.5$ to $V \geq 22.5$ in steps of 0.5 in V. The values of r, and the Hubble slope (s) and the corresponding constant (A) for the line defining the Hubble relation

$$V_{\text{mp}} = s \log \tilde{z} + A$$

are given in Table 2.

It is enlightening to notice in Table 2 that all the correlations yield very high values and are statistically significant at 99.99% level, the correlation coefficient having the maximum value for the V-range $14.0 \leq V < 19.5$. It is very unlikely that such statistically robust correlations have appeared by chance. The comprehensive sample of QSOs therefore demonstrate a highly significant relationship between confirmed redshift values and non-variable apparent magnitudes. If there is no other major factor involved, viz., luminosity evolution, the above findings would imply that QSO redshifts are of cosmological origin.

An additional feature noticed in Table 2 is that, for the V-range $14.0 \leq V < 19.5$ which yields the maximum value of the correlation coefficient, the slope (s) is very close to 5.0. Fig. 3 shows the plot of $\log \tilde{z}$ against V_{mp} for the V-range $14.0 \leq V < 19.5$ and the corresponding best fitting least square regression line. The line for the slope $s = 5.0$ is also shown in the figure. The closeness of the two lines is at once evident. It should be noted that $s = 5.0$ is the slope expected “from the expansion of the universe if luminosities are evaluated assuming quasars are at cosmological distances” (Bahcall & Hills 1971).

To investigate the matter further, we performed the usual t-test to test the validity of the hypothesis that the slope exhibited by the line for the V-range $14.0 \leq V < 19.5$ is *not* statistically different from 5.0 magnitude per decade, where

$$t = (5 - s)/\sigma_s.$$

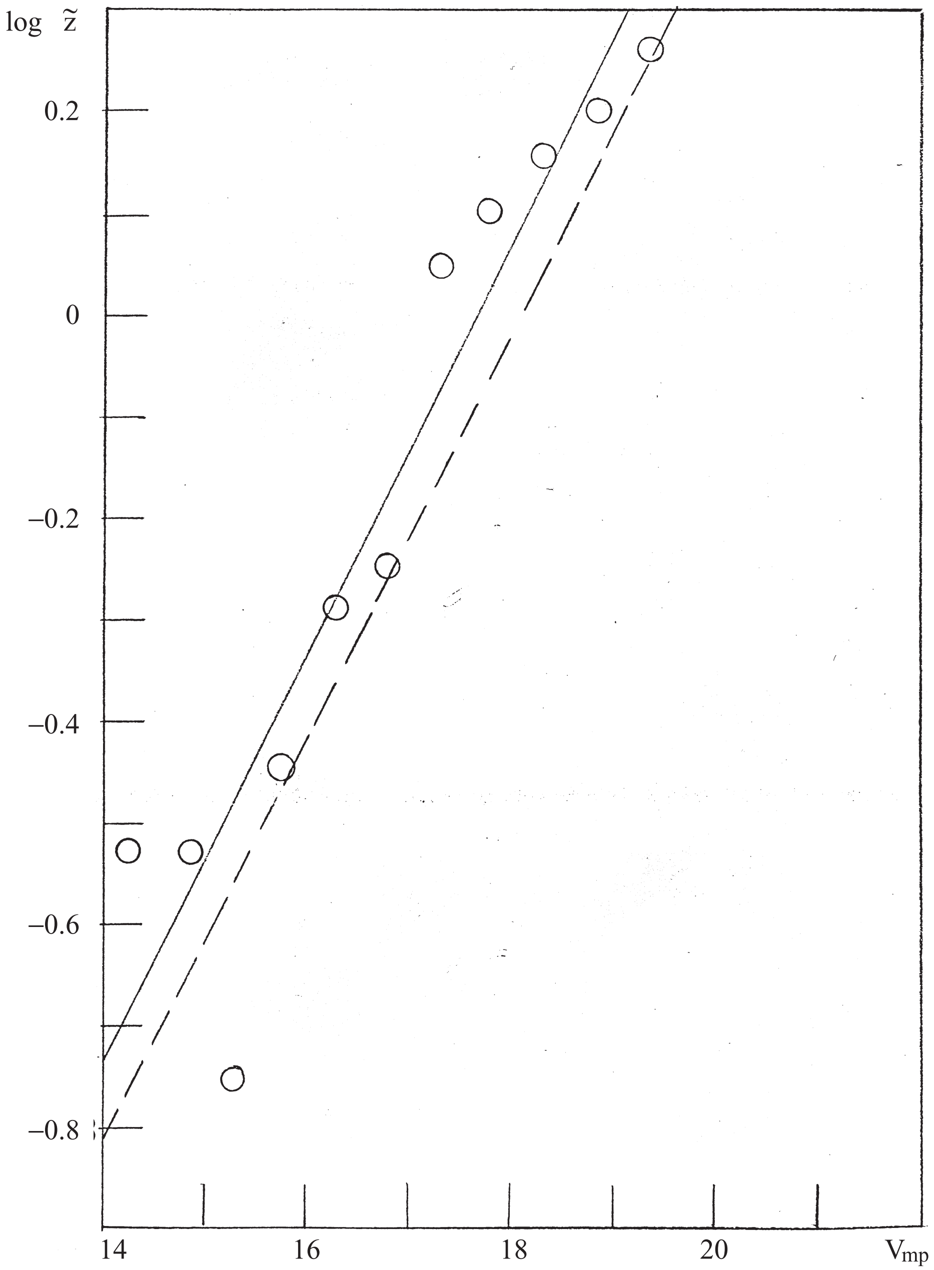

Figure 3. Plots of log $\tilde{z}$ against V_{mp} (the mid-point of each V-interval in Figures 2) for the V-range $14.0 \le V < 19.5$. The solid line is the best fitting least square regression line $V_{\mathrm{mp}} = 4.9826 \log \tilde{z} + 17.6393$, and the dotted line represents the Hubble relation $V = 5 \log z + 18$.

σ_s is the root mean square of the vertical deviations of the observed $\log \tilde{z}$ values from the best fitting least square line. It is estimated as

$$\sigma_s = [(D_1^2 + {D_2}^2 + \ldots D_N^2)/N]^{1/2},$$

where $D_1, D_2, \ldots D_N$ $(N = 11)$ are the differences between the values of $\log \tilde{z}$ observed and those calculated from the fitted straight line for each $V_{\rm mp}$ plotted in the Fig. 3. With $\sigma_s = 0.1118$ and 9 degrees of freedom, the value of $t = 0.1556$ is significant only at 55% level, indicating that the departure of the slope from the value of 5.0 is *not* statistically significant. The t-test for all other V-ranges in Table 2 yielded significance levels above 95% (not shown here), indicating that the departures are statistically significant.

It appears from Table 1 that the confidence limits of $\tilde{z}$ are rather high for the V interval $14.5 \leq V < 15.0$, and are also somewhat high for two others, viz., $14.0 \leq V < 14.5$ and $15.0 \leq V < 15.5$. Any possible error involved in the determination of $\tilde{z}$ implied by these few higher values of confidence limits may alter the corresponding correlation coefficients presumably by certain small amounts, but would have little impact on the relationship reported here, since the values of the correlation coefficient are already very high. The same is true for the closeness of the Hubble slope (s) to the value of 5. The significance level of the t-test for the interval $14.0 \leq V < 19.5$ is quite low. A small change in the value of t due to any similar error and the consequent change in the significance level would not have any appreciable effect on the result. The conclusion reached in the present analysis therefore will not change, although values of r, s, t and σ_s may change slightly. Having said that, it should be noted that the comparitively higher values of confidence limits in the few cases mentioned above are due to the nature of the distribution produced by a rather small number of objects at those V-intervals as can be seen in Fig. 2(a). It is expected that additional objects will be discovered in future, and the matter should be followed up.

The investigation presented above demonstrates that redshifts of QSOs are correlated with their apparent magnitudes. Further, such correlation exists over the entire range of apparent magnitudes studied here, viz., $14.0 \leq V \geq 22.5$. Results of the analysis suggest that redshifts of QSOs are of cosmological origin, similar to redshifts of galaxies. The importance of the present study is that it has been done for a comprehensive sample, representing the general population of QSOs, as opposed to studies in subsamples, limited samples, or specially selected samples mentioned earlier.

Furthermore, the study also finds that QSOs with $14.0 \leq V < 19.5$ obey the Hubble relation of the form $V = 5 \log z + C$ very convincingly, while significant departures from this relation is noticed as more and more weaker sources are added to the analysis. It may be noted that $V = 19.5$ may be the "selection limit" (Longair & Scheur 1967). As for the sample used in the present analysis, an inspection of Fig. 1 would show that the number of QSOs fall off very rapidly at $V \geq 19.5$. There appears to be a relative paucity of data for weaker QSOs. It will be of great interest to see the outcome of such analysis as future observations yield data of more and more weaker sources.

Finally, in view of the findings of the present analysis, evolution of the luminosity function should be reexamined in the light of the currently developed Λ-cosmology. This is of course out of scope of this work.

Acknowledgement

The author thanks an anonymous referee for helpful suggestions.

References

Bahcall, J., Hills, R. 1973, *Astrophys. J.* **179,** 699.
Basu, D. 1993, *Ap. Letts. & Comm.* **29,** 249.
Basu, D., Haque-Copilah, S. 2001, *Phys. Scr.* **63,** 425.
Burbidge, G., O'Dell, S. 1973, *Astrophys. J.* **183,** 759.
De Veny, J., Osborne, W., Janes, K. 1971, *Publ. Astron. Soc. Pac.* **83,** 611.
Hoyle, F., Burbidge, G. 1966, *Nature* **210,** 1346.
Hewitt, A., Burbidge, G. 1993, *Astrophys. J. Suppl.* **87,** 451 (HB).
Longair, M., Scheur, P. 1967, *Nature* **215,** 919.
McCrea, W. 1972, *External galaxies and Quasi Stellar Objects, IAU Symposium No. 44*. (ed.) D. S. Evans (Dordrecht: Reidel).
Pica, A., Smith, A. 1983, *Astrophys. J.* **272,** 11.
Sachs, L. 1984, *Applied Statistics: A Handbook of Techniques*, (New York: Springer Verlag).
Sandage, A. 1965, *Astrophys. J.* **141,** 1560.
Sandage, A. 1966, *Astrophys. J.* **146,** 13.
Schmidt, M. 1968, *Astrophys. J.* **151,** 393.
Setti, G., Woltjer, L. 1971, *Astrophys. J.* **181,** L61.
Stannard, D. 1973, *Nature* **236,** 295.

J. Astrophys. Astr. (2003) **24,** 23–35

HI Fluctuations at Large Redshifts: II – the Signal Expected for the GMRT

Somnath Bharadwaj[1] & Sanjay K. Pandey[2]

[1]*Department of Physics and Meteorology & Center for Theoretical Studies,*
I.I.T. Kharagpur 721 302, India. e-mail: somnath@phy.iitkgp.ernet.in
[2]*Department of Mathematics, L.B.S. College, Gonda 271 001, India.*
e-mail: spandey@iucaa.ernet.in

Received 2003 May 17; accepted 2003 June 4

Abstract. For the GMRT, we calculate the expected signal from redshifted HI emission at two frequency bands centered at 610 and 325 MHz. The study focuses on the visibility-visibility cross-correlations, proposed earlier as the optimal statistical estimator for detecting and analyzing this signal. These correlations directly probe the power spectrum of density fluctuations at the redshift where the radiation originated, and thereby provide a method for studying the large scale structures at large redshifts. We present detailed estimates of the correlations expected between the visibilities measured at different baselines and frequencies. Analytic fitting formulas representing the salient features of the expected signal are also provided. These will be useful in planning observations and deciding an optimal strategy for detecting this signal.

Key words. Cosmology: theory, observations, large scale structures—diffuse radiation.

1. Introduction

In two earlier papers (Bharadwaj, Nath & Sethi 2001; hereafter referred to as paper I and Bharadwaj & Sethi 2001; hereafter referred to as paper II) we have studied the possibility of detecting redshifted 21 cm emission from neutral hydrogen (HI) at high redshift sand using these observations to probe large scale structures. Our approach has been based on the fact that the HI density in the redshift range $1 \leq z \leq 3.5$ is known from observations of Lyman-α absorption lines seen in quasar spectra. These observations currently indicate $\Omega_{\rm gas}(z)$, the comoving density of neutral gas expressed as a fraction of the present critical density, to be nearly constant at a value $\Omega_{\rm gas}(z) \sim 10^{-3}$ for $z \geq 1$ (Peroux *et al.* 2001). The bulk of the neutral gas is in clouds which have HI column densities greater than 2×10^{20}atoms/cm^2 (Peroux *et al.* 2001, Storrie-Lombardi, McMahon & Irwin 1996; Lanzetta, Wolfe & Turnshek 1995). These high column density clouds are responsible for the damped Lyman-α absorption lines observed along lines of sight to quasars. The flux of HI emission from individual clouds ($< 10\,\mu$Jy) is too weak to be detected by existing radio telescopes unless the image of the cloud is significantly magnified by an intervening cluster gravitational lens (Saini, Bharadwaj & Sethi 2001). Although we may not be able to detect individual clouds, the redshifted HI emission from the distribution of clouds will appear as a background radiation in low frequency radio observations. In the two earlier papers, and in the present paper we investigate issues related to calculating the expected signal and detecting it.

The hope of detecting this signal lies in the fact that the distribution of the HI clouds is expected to be clustered. The clustering pattern of the HI clouds will be reflected in the angular and spectral distribution of the redshifted 21 cm emission. It is the aim of this paper, and the two previous papers, to characterize the expected properties of this signal and to propose an optimum statistical estimator to extract this signal from the various foregrounds and the system noise which will also be present in any low frequency observation. In paper II we proposed the cross-correlations between the visibilities measured at different baselines and frequencies as a statistical estimator to optimally detect the HI signal. This has the advantage that the system noise contribution to visibilities measured at different baselines and frequencies are uncorrelated. Further, in paper II we showed that the visibility-visibility cross-correlations directly probes the power spectrum of density fluctuations at the epoch where the HI emission originated. In this paper we present results of a detailed investigation of the signal expected for this statistical estimator for observations with the GMRT.

We next present a brief outline of this paper. In section 2 we review the formalism used to calculate the visibility-visibility cross-correlations. In section 3 we present the values of a set of useful parameters to do with the GMRT (Swarup *et al.* 1991), the cosmological model chosen for these investigations and the HI distribution. In section 4 we present the results of our investigations, and in section 5 we discuss the results and present conclusions.

2. Formalism

We consider a situation where an interferometric array of N antennas is used to carry out low frequency radio observations. The observations are carried out at NC frequency channels $\{\nu_1, \nu_2, \nu_3, ..., \nu_{NC}\}$ covering a frequency band B centered at the frequency ν_c. For the purpose of this paper we assume that the antennas are distributed on a plane, and the position of each antenna is denoted by a two dimensional vector $\mathbf{d}_i$. The antennas all point in the same direction along the unit vector $\mathbf{n}$ which we take to be vertically upwards. The beam pattern $A(\vec{\theta})$ quantifies how the individual antenna, pointing upwards, responds to signals from different directions in the sky. This is assumed to be a Gaussian $A(\vec{\theta}) = e^{-\theta^2/\theta_0^2}$ with $\theta_0 \ll 1$ i.e., the beam width of the antennas is small, and the part of the sky which contributes to the signal can be well approximated by a plane.

The quantity measured in interferometric observations is the visibility $V(\mathbf{U}, \nu)$ which is recorded for every independent pair of antennas (baseline) at every frequency channel in the band. For any pair of antennas, the visibility depends on the vector $\mathbf{d} = \mathbf{d}_i - \mathbf{d}_j$ joining the position of the two antennas. It is convenient to express the visibility as a function of the variable $\mathbf{U}$ which is $\mathbf{d}$ expressed in units of the wavelength i.e., $\mathbf{U} = \mathbf{d}/\lambda$. Typically, the visibility is recorded for $\mathbf{U}$ in a range $U_{\rm min} \leq \mid \mathbf{U} \mid \leq U_{\rm max}$. The visibility corresponding to $\mathbf{U} = 0$ is the flux measured by a single antenna, and this is usually not recorded in an interferometric array.

In paper II we calculated the HI contribution to the visibility $V(\mathbf{U}, \nu)$. This can be expressed as

$$V(\mathbf{U}, \nu) = \bar{I}_\nu \int \frac{d^3k}{(2\pi)^3} \Delta^s_{\mathrm{HI}}(\mathbf{k}, \nu) e^{-ik_\parallel r_\nu} a_\nu \left(\mathbf{U} - \frac{\mathbf{k}_\perp r_\nu}{2\pi}\right) . \tag{1}$$

The frequency ν appears in many of the terms on the right hand side of equation (1) to indicate that these are to be evaluated at the redshift $z = \nu_e/\nu - 1$ where the radiation originated. The first term $\bar{I}_\nu$ is the specific intensity of the redshifted HI emission expected if the HI were uniformly distributed. This is given to be (from equation (3) of paper II)

$$\bar{I}_\nu = \frac{2.7\,\mathrm{Jy}}{\mathrm{degree}^2}\, h\, \Omega_{\mathrm{gas}}(z) \left[\frac{H_0}{H(z)}\right], \tag{2}$$

where $H(z)$ is the Hubble parameter, and H_0 is its present value.

It should be noted that equation (14) of paper II is incorrect. Equation 3 of paper II is correct. The error came about when expressing $\bar{n}_{\mathrm{HI}}(z)$, the comoving number density of HI atoms in terms of Ω_{HI}. As a result of this and an error in the computer programs that were used, the predictions for 610 MHz in paper II are also incorrect.

The HI emission originates from the gas located at a distance r_ν in the direction $\mathbf{n}$. The term $\Delta^s_{\mathrm{HI}}(\mathbf{k}, \nu)$ in equation (1) is the Fourier transform of the density contrast of the HI distribution in redshift space. Any Fourier mode $\mathbf{k}$ can be decomposed into two parts, a component $k_\parallel$ parallel to $\mathbf{n}$ and a component $\mathbf{k}_\perp$ perpendicular $\mathbf{n}$. Assuming that the HI density fluctuations evolve according to linear theory, and that these may be related to the fluctuations in the underlying dark matter distribution through a linear bias parameter $b(z)$, we have

$$\Delta^s_{\mathrm{HI}}(\mathbf{k}, \nu) = b(z) D(z) \left[1 + \beta(z) \frac{k_\parallel^2}{k^2}\right] \Delta(\mathbf{k}), \tag{3}$$

where $D(z)$ is the growing mode of density perturbations (Peebles 1980), $\beta(z) = f(\Omega_m, \Omega\Lambda)/b(z)$ (Lahav *et al.* 1991) is the linear redshift distortion parameter, and $\Delta(\mathbf{k})$ is the Fourier transform of the density fluctuations of the dark matter distribution at the present epoch.

We also have

$$\langle \Delta(\mathbf{k}) \Delta^*(\mathbf{k}') \rangle = (2\pi)^3 \delta^3(\mathbf{k} - \mathbf{k}') P(k), \tag{4}$$

where $\langle\rangle$ denotes ensemble average, and $P(k)$ is the power-spectrum of dark matter fluctuations at the present epoch.

The quantity $a_\nu(\mathbf{U})$ in equation (1) is the Fourier transform of $A(\theta)$, the beam pattern. For a Gaussian beam, the Fourier transform also is a Gaussian and we have

$$a_\nu \left(\mathbf{U} - \frac{\mathbf{k}_\perp r_\nu}{2\pi}\right) = \pi \theta_{0\nu}^2 \exp\left[-\pi^2 \theta_{0\nu}^2 \left(\mathbf{U} - \frac{\mathbf{k}_\perp r_\nu}{2\pi}\right)^2\right]. \tag{5}$$

This function is sharply peaked around $\mathbf{k}_\perp = 2\pi \mathbf{U}/r_\nu$, and only values of $\mathbf{k}_\perp$ in the interval $\mid \Delta\mathbf{k}_\perp \mid < 1/(r_\nu \theta_{0\nu})$ centered around this value will contribute to the integral in equation (1). It follows that the visibility $V(\mathbf{U}, \nu)$ picks up contributions only from those fluctuations $\Delta^s_{\rm HI}(\mathbf{k}, \nu)$ for which $\mathbf{k}_\perp \approx 2\pi \mathbf{U}/r_\nu$.

A point to be noted is that in the Gaussian model for the beam pattern its Fourier transform is also a Gaussian which is a non-compact function. In reality, the Fourier transform of the beam pattern is compact and it is zero outside a radius D/λ i.e., $a_\nu(\mathbf{U} - \frac{\mathbf{k}_\perp r_\nu}{2\pi}) = 0$ for $\mid \mathbf{U} - \frac{\mathbf{k}_\perp r_\nu}{2\pi} \mid > D/\lambda$. This fact plays a role in the later discussion and we shall refer back to it at the appropriate place.

In this paper we shall study in some detail the cross-correlation $\langle V(\mathbf{U}_1, \nu_1) V^*(\mathbf{U}_2, \nu_2)\rangle$ between the visibilities measured at two different baselines and frequencies. Using equations (1), (3), (4), this turns out to be

$$\langle V(\mathbf{U}_1, \nu_1) V^*(\mathbf{U}_2, \nu_2)\rangle = \left[\bar{I} D b\right]_1 \left[\bar{I} D b\right]_2 \int \frac{d^3k}{(2\pi)^3} P(k) \left[1 + \beta_1 \frac{k_\parallel^2}{k^2}\right]$$
$$\times \left[1 + \beta_2 \frac{k_\parallel^2}{k^2}\right] \cos[k_\parallel (r_1 - r_2)]\, a_1\left(\mathbf{U}_1 - \frac{\mathbf{k}_\perp r_1}{2\pi}\right) a_2^*\left(\mathbf{U}_2 - \frac{\mathbf{k}_\perp r_2}{2\pi}\right), \qquad (6)$$

the imaginary part being zero. We shall use equation (6) to calculate the correlations between the visibilities at different baselines and frequencies. We next discuss a few approximations which can be used to simplify equation (6) and which help in interpreting this equation. We test the range of validity of these approximations and comment on this later in the paper.

Typically, the bandwidth B is small compared to the central frequency ν_c, and the quantities I_ν, $b(z)$, $D(z)$, $\beta(z)$, $\theta_{0\nu}$ and r_ν in equation (6) do not vary substantially across the band. We can evaluate these at ν_c instead of calculating them separately at ν_1 and ν_2, and at some instances we do not explicitly show the subscript ν_1 or ν_2 for these quantities. The term $\cos[k_\parallel(r_1 - r_2)]$ is an exception because $k_\parallel(r_1 - r_2)$ may be large even if $\Delta\nu = \nu 2 - \nu_1 \ll \nu_c$. This term may be approximated as $\cos[k_\parallel r_\nu^{'} \Delta\nu]$, where $r_\nu^{'} = dr_\nu/d\nu$.

The term $a_1(\mathbf{U}_1 - \frac{\mathbf{k}_\perp r}{2\pi}) a_2^*(\mathbf{U}_2 - \frac{\mathbf{k}_\perp r}{2\pi})$ in equation (6) is a product of two functions, one sharply peaked at $\mathbf{k}_\perp = 2\pi \mathbf{U}_1/r$ and another at $\mathbf{k}_\perp = 2\pi \mathbf{U}_2/r$. The two peaks have very little overlap if $\mid \mathbf{U}_1 - \mathbf{U}_2 \mid \gg 1/\theta_0$, and the visibilities measured at two such baselines will be uncorrelated. There will be correlations only between visibilities measured at different frequencies for nearby baselines, i.e., $\mid \mathbf{U}_1 - \mathbf{U}_2 \mid \leq 1/\theta_0$. For the situation where $\mathbf{U}_1 = \mathbf{U}_2 \gg 1/\theta_0$, we may use the approximation (paper II)

$$\mid a_1\left(\mathbf{U}_1 - \frac{\mathbf{k}_\perp r}{2\pi}\right) \mid^2 \approx \left(\frac{2\pi^3 \theta_0^2}{r^2}\right) \delta^2\left(\mathbf{k}_\perp - \frac{2\pi}{r}\mathbf{U}_1\right) \qquad (7)$$

whereby equation (6) is considerably simplified and we have

$$\langle V(\mathbf{U}, \nu) V^*(\mathbf{U}, \nu + \Delta\nu)\rangle = \frac{[\bar{I} b D \theta_0]^2}{2r^2} \int_0^\infty dk_\parallel P(k) \left[1 + \beta \frac{k_\parallel^2}{k^2}\right]^2 \cos(k_\parallel r^{'} \Delta\nu) \quad (8)$$

where $k = \sqrt{(2\,\pi\, U/r)^2 + k_\parallel^2}$.

Table 1.

Frequencies ν_c (MHz)	610 325
Possible bandwidths - B (MHz)	16 8 4 2 1 0.5
No. of channels - NC	128
Antenna separations - d (m)	$\mathrm{d_{min}} \sim 60$ $\mathrm{d_{max}} \sim 25 \times 10^3$

Table 2.

ν_c	$U_{\min}$	$U_{\max}$	$\theta_0 \approx 0.6 \times \theta_{\mathrm{FWHM}}$
610	123	51×10^3	0.54°
325	65	27×10^3	1.08°

Equation (8) provides considerable insight on the visibility-visibility cross-correlation in the situation where $\mathbf{U}_1 = \mathbf{U}_2 = \mathbf{U}$. The point to note that the visibility signal measured at a baseline $\mathbf{U}$ receives contributions only from the fluctuations $\Delta(\mathbf{k})$ for which $\mathbf{k}_\perp = (2\pi\,\mathbf{U})/r$, i.e., $\mathbf{k}_\perp$ is fixed but $k_\parallel$ can have any value. As a consequence the correlation $\langle V(\mathbf{U},\nu)V^*(\mathbf{U},\nu+\Delta\nu)\rangle$ directly probes the power spectrum $P(k)$ at all Fourier modes $k > k_{\min} = 2\pi U/r$.

In the next sections of this paper we use the formulas presented here to investigate the HI signal expected for the GMRT and study how this is related to the large-scale structures at the redshift where the HI emission originated. We also compare the predictions of equation (6) with those of (8) and test the range of validity of the approximations discussed above.

3. Some useful parameters

3.1 *GMRT*

The Giant Meterwave Radio Telescope (GMRT) has 30 radio antennas of 45 m diameter each. We present below, in tabular form (Tables 1 and 2), some of the parameters relevant for the proposed HI observations. We have restricted our analysis to only two of the GMRT frequencies which correspond to HI in the range $1 \le z \le 3.5$.

3.2 *Cosmological model*

For the background cosmological model we have used $H_0 = 100\,h$ km/s/Mpc with $h = 0.7$, $\Omega_{m0} = 0.3$, $\Omega_{\Lambda 0} = 0.7$, $\Omega_{\mathrm{Baryon}\,0} = 0.015\,h^{-2}$ and $\Omega_{\mathrm{gas}} = 1. \times 10^{-3}$. The power spectrum of dark matter density fluctuations is normalized to COBE (Bunn & White 1996), and its shape is determined using the analytic fitting form for the CDM power spectrum given by Efstathiou, Bond & White (1992). The value of the shape parameter turns out to be $\Gamma = 0.2$ for the set of cosmological parameters used here. The power spectrum is shown in Fig. 1.

Very little is known about the bias b which relates the HI fluctuations to the dark matter fluctuations, and we have used a fixed value $b = 1$ throughout.

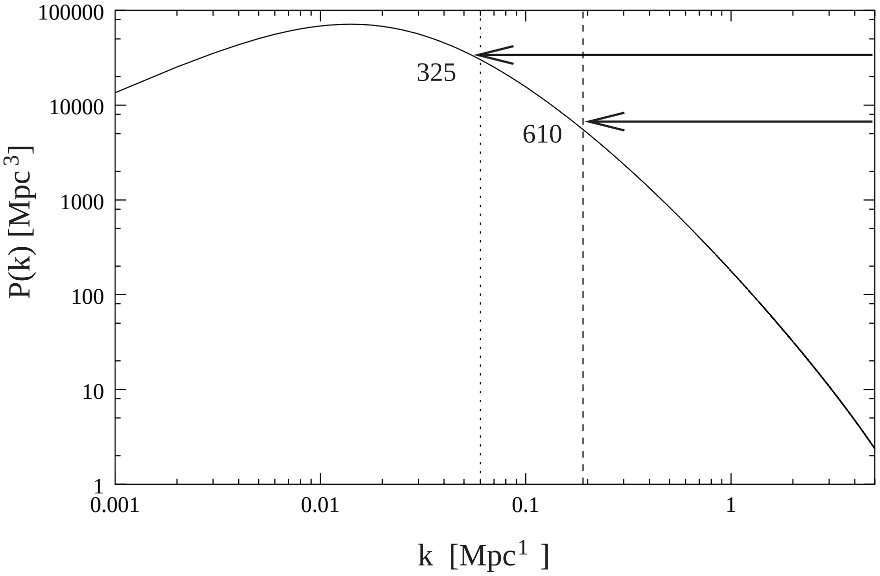

Figure 1. This shows the part of the power spectrum probed by the smallest baselines in GMRT for the two frequencies indicated in the figure. The power spectrum is normalised to COBE and is shown for $z = 0$.

Table 3.

ν_c	z	r (Mpc)	$\bar{I}$ (Jy/deg^2)	r' (Mpc/MHz)	$k_{\rm min}$ (Mpc^{-1})
610	1.33	4030	9.0×10^{-4}	7.7	0.16
325	3.37	6686	3.7×10^{-4}	11.3	0.09

3.3 *HI*

We first present the values of the redshift, comoving distance and the expected specific intensity of the HI distribution for the two GMRT frequencies of our interest (Table 3). We also show values of $r' = dr/d\nu$ which are useful in calculating the comoving separation corresponding to a given frequency interval i.e., $\Delta r = r' \Delta\nu$. The last column in Table 3 shows the value of $k_{\rm min}$ for the baseline $U = 100$. This represents the smallest Fourier mode probed by this baseline.

In Fig. 1 we show the part of the power spectrum which will be probed by $U_{\rm min}$ the smallest baseline available on GMRT. The value of $k_{\rm min}$ will be higher for the larger baselines and these will probe a smaller part of the power spectrum.

4. Results

4.1 *Single dish observations*

It is possible to use the GMRT as a set of 30 single dish antennas instead of an interferometric array. In such observations the flux incident on each antenna is recorded

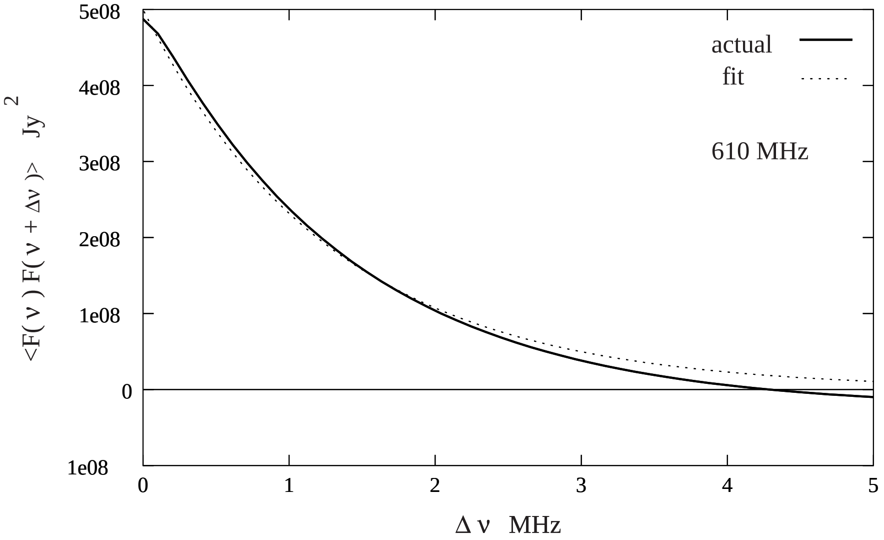

Figure 2. This shows the contribution from redshifted HI emission to the correlation between the flux expected at two different frequencies in the 610 MHz band for single dish observations using GMRT. The analytic fit (equation 9) is also shown.

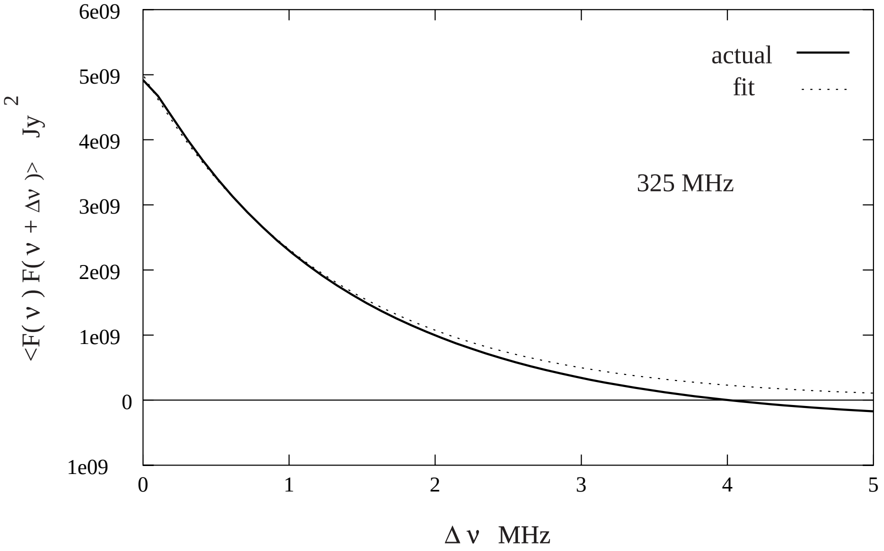

Figure 3. This shows the contribution from redshifted HI emission to the correlation between the flux expected at two different frequencies in the 325 MHz band for single dish observations using GMRT. The analytic fit (equation 9) is also shown.

and the signal from the 30 antennas is combined. The flux $F(\nu)$ is the visibility $V(\mathbf{U}, \nu)$ at $\mathbf{U} = 0$, and the flux expected from the redshifted HI emission can be calculated using equation (1). We use equation (6) to calculate the correlation between the flux measured at different frequencies $\langle F(\nu)F(\nu + \Delta\nu)\rangle$. The results for the two GMRT bands of interest are shown in Figs. 2 and 3. The approximate formula (equation 8) is valid only when $\mid \mathbf{U} \mid \gg 1/\theta_0$, and this cannot be used here.

We find that the HI flux at neighbouring frequencies are correlated. The correlation signal in the 610 MHz band is nearly an order of magnitude higher than the correlation signal in the 325 MHz band. In both the bands the correlation falls exponentially as $\Delta\nu$ is increased. For $\Delta\nu \leq 2$ MHz, the correlation can be very well approximated by the fitting formula

$$\langle F(\nu)F(\nu+\Delta\nu)\rangle = C_\nu \exp\left(\frac{-\Delta\nu}{1.3\text{MHz}}\right) \qquad \begin{cases} C_{610} = 5\times10^{-8}\text{Jy}^2 \\ C_{325} = 5\times10^{-9}\text{Jy}^2. \end{cases} \tag{9}$$

The fitting formula (equation 9) fails at larger $\Delta\nu$ where $\langle F(\nu)F(\nu+\Delta\nu)\rangle$ becomes negative indicating that the fluxes have a weak anti-correlation for $\Delta\nu > 4$ MHz.

4.2 *Interferometric observations*

We next consider interferometric observations with GMRT. The correlation $\langle V(\mathbf{U}_1,\nu_1)V^*(\mathbf{U}_2,\nu_2)\rangle$ is maximum when $\mathbf{U}_1 = \mathbf{U}_2$, and we consider this situation first. In addition, it is a good approximation to represent the correlation as a function of $\Delta\nu = \nu_2 - \nu_1$, provided ν_1 and ν_2 are in the same GMRT band, Our results are shown in Figs. 4 and 5.

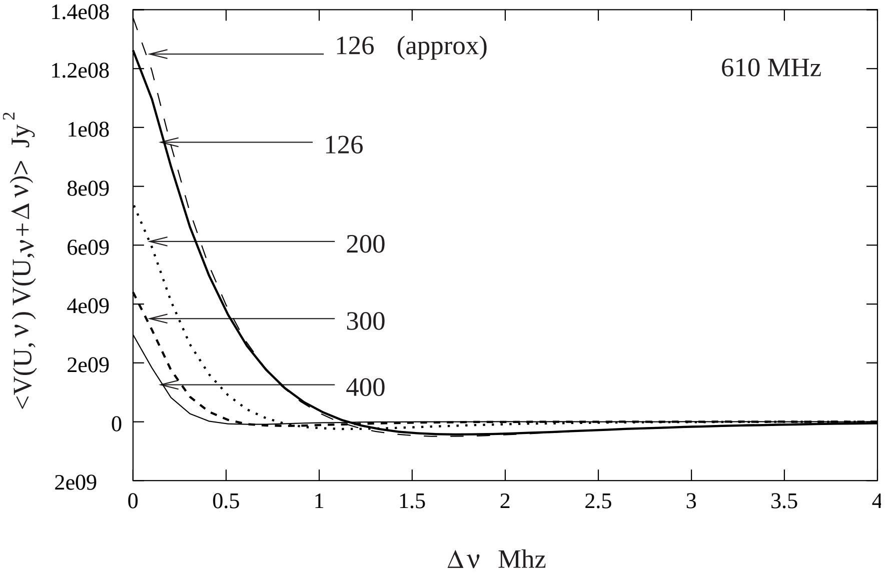

Figure 4. This shows the correlation between the visibilities $V(\mathbf{U},\nu)$ and $V(\mathbf{U},\nu+\Delta\nu)$ expected for the same baseline $\mathbf{U}$ at two different frequencies. The results are shown for different values of U (shown in the figure) starting from $U_{\rm min}$ for the 610MHz band. The results have been calculated using equation (6), the predictions of the approximate formula (equation (8) are also shown for $U_{\rm min}$.

We have calculated the correlations using two different formulas i.e., equations (6) and (8). The latter can only be used when $\mathbf{U}_1 = \mathbf{U}_2 = \mathbf{U}$, and it is based on an approximation which is valid only when $\mathbf{U} \gg 1/\theta_0$. We find that the approximate

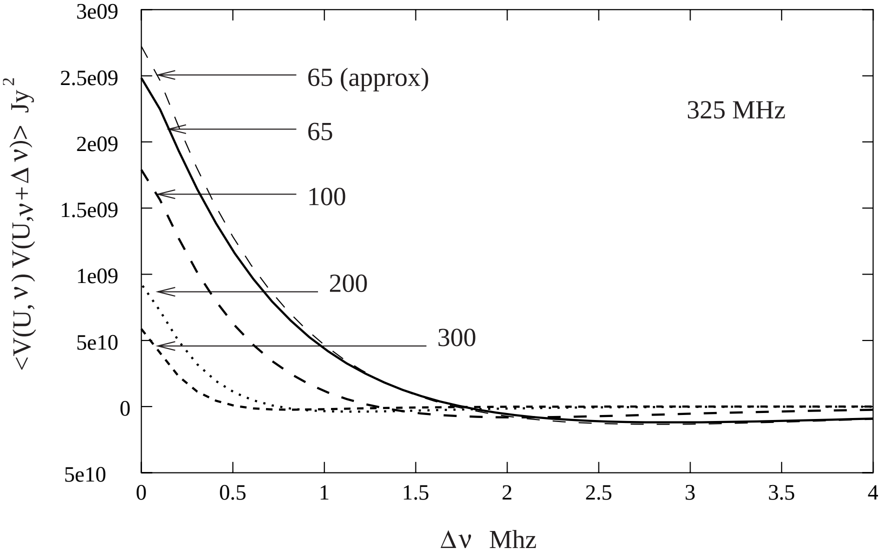

Figure 5. This shows the same thing as figure 4 but for the 325MHz band.

formula (equation 8) matches equation (6) quite well ($\sim 10\%$) at the smallest baseline $U_{\rm min}$ for both 610 MHz and 325 MHz (Figs. 4 and 5). The agreement is better than 10% for the larger baselines.

The correlation signal is the strongest at the smallest baseline $U_{\rm min}$ and falls quickly for the larger values of U. The larger baselines receive contributions from a smaller part of the power spectrum (Fig. 1) and the fall-off with U reflects the shape of the power spectrum at the mode $k \sim (2\pi U/r)$. At a fixed U, the visibilities at adjacent frequencies are correlated, the correlation falls approximately exponentially with increasing $\Delta\nu$. At the larger baselines the correlation decreases faster with increasing $\Delta\nu$. At all baselines, the correlation crosses zero and there are anti-correlations for large $\Delta\nu$. We find that in the range of U and $\Delta\nu$ where the visibility-visibility correlation signal is large, it can be approximated by the fitting formula

$$\langle V(U,\nu)V^*(U,\nu+\Delta\nu)\rangle = C_\nu \exp\left(\frac{-\Delta\nu\, u^{0.8}}{0.7}\right)\frac{\sin\left(2\,\Delta\nu\, u^{1.2}\right)}{2\,\Delta\nu\, u^{1.2}}, \tag{10}$$

$$C_{610} = 1.6\times 10^{-8}{\rm Jy}^2 u^{-1.2} \qquad\qquad C_{325} = 1.8\times 10^{-9}{\rm Jy}^2 u^{-0.9}$$

where $u = (U/100)$ and $\Delta\nu$ is in MHz.

We next calculate the correlation $\langle V(\mathbf{U},\nu)V^*(\mathbf{U}+\Delta\mathbf{U},\nu+\Delta\nu)\rangle$ between the visibilities at two different baselines and frequencies. We use equation (6) to calculate this. In general, the behaviour of the correlation will depend on both, the magnitude and the direction of $\Delta\mathbf{U}$. We have separately considered two situations (1) $\Delta\mathbf{U}$ parallel to $\mathbf{U}$ and (2) $\Delta\mathbf{U}$ perpendicular to $\mathbf{U}$. The results are presented in Figs. 6 and 7 for $U = 200$. The results are similar for other values of U.

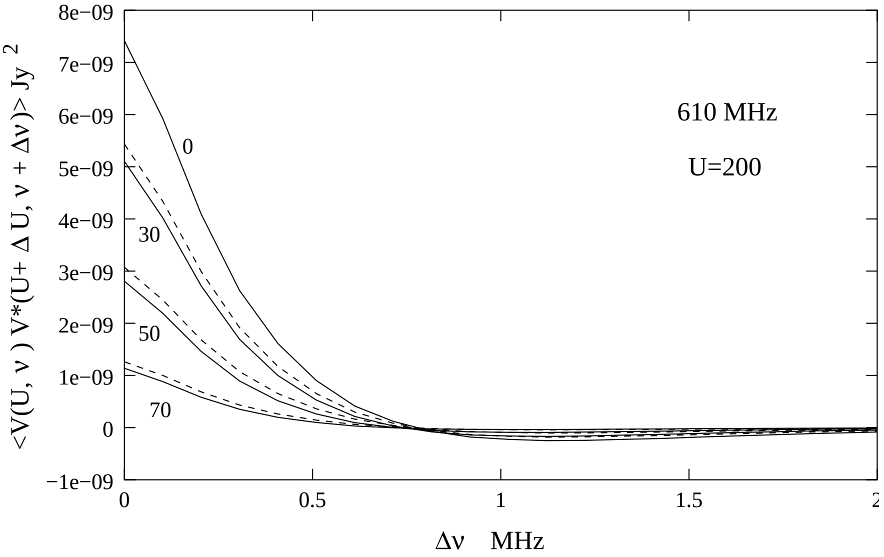

Figure 6. This shows the expected correlation between the visibilities $V(\mathbf{U}, \nu)$ and $V(\mathbf{U}+\Delta\mathbf{U}, \nu+\Delta\nu)$ at two different baselines and frequencies. The results are shown at $U = 200$ for different values of ΔU (shown in the figure), when $\Delta\mathbf{U}$ is parallel to $\mathbf{U}$ (solid line) and $\Delta\mathbf{U}$ is perpendicular to $\mathbf{U}$ (dashed line). These results are for the 610MHz band.

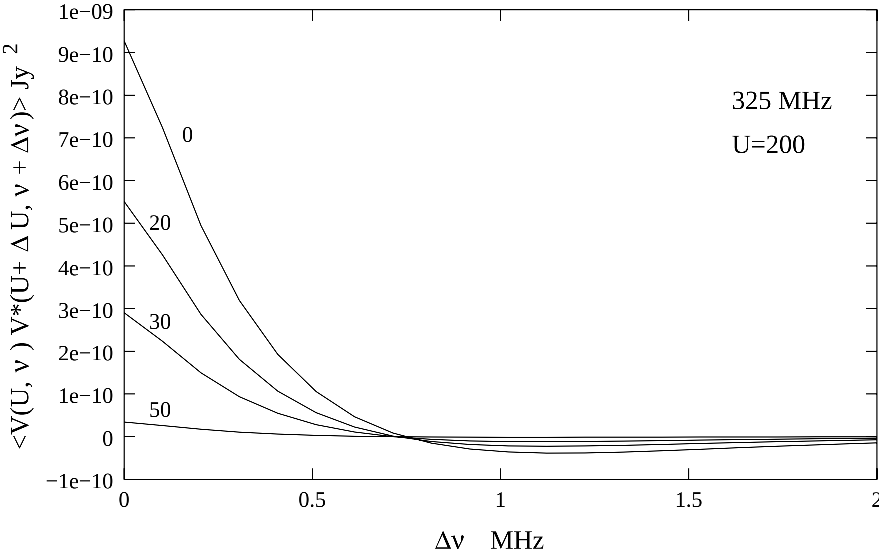

Figure 7. This is the same as figure 6 except that it is for the 325MHz band. Here the results do not depend on whether $\Delta\mathbf{U}$ is parallel or perpendicular to $\mathbf{U}$.

We find that the correlation falls rapidly as $\Delta\mathbf{U}$ increases. The $\Delta\mathbf{U}$ dependence is found to be anisotropic for the 610 MHz band. The correlation falls faster when $\Delta\mathbf{U}$ is parallel to $\mathbf{U}$ than when it is perpendicular to $\mathbf{U}$. The $\Delta\mathbf{U}$ dependence is found to be isotropic for the 325 MHz band, in both the bands the $\Delta\mathbf{U}$ dependence can be well approximated by a Gaussian

$$\begin{aligned}\langle V(\mathbf{U},\nu)V^*(\mathbf{U}+\Delta\mathbf{U},\nu+\Delta\nu)\rangle &= \exp\left[-\left(\frac{\Delta U_{\parallel}}{a_\nu}\right)^2-\left(\frac{\Delta U_{\perp}}{b_\nu}\right)^2\right]\\ &\quad\times\langle V(U,\nu)V^*(U,\nu+\Delta\nu)\rangle \qquad (11)\\ a_{610}=50,\ b_{610}=53 \qquad & a_{325}=b_{325}=28,\end{aligned}$$

where $\Delta U_{\parallel}$ is the component of $\Delta\mathbf{U}$ parallel to $\mathbf{U}$, and $\Delta U_{\perp}$ is the component perpendicular to $\mathbf{U}$. This fitting function is found to be a very good approximation over a large range of of $\mathbf{U}$, $\Delta\mathbf{U}$ and $\Delta\nu$.

It should be noted that contrary to the predictions of our fitting formula (equation 11), the cross-correlations between the different baselines is *exactly zero* i.e., $\langle V(\mathbf{U},\nu)V^*(\mathbf{U}+\Delta\mathbf{U},\nu+\Delta\nu)\rangle = 0$ if $\mid \Delta\mathbf{U} \mid > D/\lambda$. This is a consequence of the fact that we have modeled the Fourier transform of the beam pattern as a Gaussian whereas it actually has compact support (discussed in section 2). The cross-correlations are zero for $\mid \Delta\mathbf{U} \mid > 90$ at 610 MHz and $\mid \Delta\mathbf{U} \mid > 50$ at 325 MHz. This discrepancy does not significantly change our results as the Gaussian function in equation (11) is extremely small ($< 1\%$) at the values of $\mid \Delta\mathbf{U} \mid$ where the cross-correlations vanish.

5. Discussion and conclusions

We have investigated in detail the redshifted HI emission signal expected in GMRT observations in the 325MHz and the 610MHz frequency bands. The properties of the visibility-visibility cross-correlation $\langle V(\mathbf{U},\nu)V^*(\mathbf{U}+\Delta\mathbf{U},\nu+\Delta\nu)\rangle$ which we propose as a statistical estimator for detecting and analyzing the signal have been studied. The signal is maximum at $U_{\rm min}$, and we find that $\langle V(\mathbf{U}_{\rm min},\nu)V^*(\mathbf{U}_{\rm min},\nu)\rangle$ is $\sim 1.3\times10^{-8}{\rm Jy}^2$ at 610 MHz and $\sim 2.5\times10^{-9}{\rm Jy}^2$ at 325 MHz. The signal falls at larger baselines, and it drops by an order of magnitude by $U\sim 10\times U_{\rm min}$. Fourteen of the thirty GMRT antennas are located within 1km. These baselines could be used for detecting the signal whereas the larger baselines where there is very little signal could be used as a control to test that what we detect is actually the HI signal and not an artifact.

The correlation $\langle V(\mathbf{U},\nu)V^*(\mathbf{U},\nu+\Delta\nu)\rangle$ fall exponentially with increasing $\Delta\nu$, the width being around 0.5 MHz at $U_{\rm min}$. The correlations fall faster at the larger baselines. The $\Delta\nu$ dependence of the correlation will be crucial in detecting the HI signal, for neither the system noise nor the galactic/extragalactic continuum radiation are expected to have such a feature.

The correlation $\langle V(\mathbf{U},\nu)V^*(\mathbf{U}+\Delta\mathbf{U},\nu+\Delta\nu)\rangle$ falls rapidly with increasing $\Delta\mathbf{U}$, the $\Delta\mathbf{U}$ dependence being well described by a Gaussian. The correlation falls by 50% when $\mid \Delta\mathbf{U} \mid\sim 42$ at 610MHz and $\mid \Delta\mathbf{U} \mid\sim 23$ at 325MHz. The correlation falls by 10% when $\mid \Delta\mathbf{U} \mid\sim 16$ at 610MHz and $\mid \Delta\mathbf{U} \mid\sim 9$ at 325MHz. The $\Delta\mathbf{U}$ dependence plays an important role in three different contexts in this discussion.

- For a pair of antennas at a separation $\mathbf{d}$, the value $\mathbf{U}=\mathbf{d}/\lambda$ changes as ν varies across the frequency band. The correlation between the visibilities measured by this pair of antennas at two different frequencies will be $\langle V(\mathbf{U},\nu)V^*(\mathbf{U}+\Delta\mathbf{U},\nu+\Delta\nu)\rangle$, where $\Delta\mathbf{U} = -(\Delta\nu/\nu)\,\mathbf{U}$ arises due to the change in wavelength. For $U \leq 500$ and $\Delta\nu \leq 1$MHz, which is the range where there is significant correlation, we find $\mid \Delta\mathbf{U} \mid < 2$. Our investigations show that this effect will cause the correlation to fall by a factor less than 10% from $\langle V(\mathbf{U},\nu)V^*(\mathbf{U},\nu+\Delta\nu)\rangle$, and we can ignore the change in **U** due to the change in frequency.

- The rotation of the earth causes all the baselines to change in time and for a time interval Δt we have $\Delta\mathbf{U} = \Delta t\,\vec{\omega}\times\mathbf{U}$. This has to be taken into account when deciding on the time interval Δt over which the visibility can be integrated without its value changing significantly. Our analysis shows that the correlation in the visibility falls by 10% or less if $\Delta U \leq 10$ and we use this as a criteria to determine Δt. In the range $U \leq 500$ where we expect most of the signal we obtain $\Delta t \sim 5\,\mathrm{min}$.
- As the earth rotates, GMRT observations will produce visibility data for a very large number of baselines **U**. The values of **U** will not be uniformly distributed in the plane of the array, and there will be regions which are more densely sampled than others. It will be useful to reduce the volume of data by combining the data in the densely sampled regions and thereby produce a set of values of the visibility on a regular grid of **U** values. Our analysis shows that the grid has to be at an interval $\Delta U \sim 40$ at 610MHz and ~ 25 at 325MHz, the visibility signal gets uncorrelated after this interval.

Two issues, the system noise and the contribution of the galactic and extragalactic continuum sources have not been addressed here. Further, we have modeled the HI gas as having a continuous distribution, whereas in reality the HI gas is in discrete, small clouds. Investigations are currently underway on these issues and the results will be communicated in forthcoming publications.

Finally, the visibility-visibility correlation signal depends on the equation of state of the dark matter and the dark energy at the epoch when the HI emission originated. This dependence comes in through the redshift space distortion parameter, the comoving distance and its derivative, all of which depend on the equation of state of the universe. We shall address the possibility of using HI observations to probe the equation of state of the universe at high redshifts in a future paper.

Acknowledgement

SB would like to thank Jayaram N Chengalur and Shiv K Sethi for useful discussions. SB would also like to acknowledge financial support from BRNS, DAE, Govt. of India, for financial support through sanction No. 2002/37/25/BRNS. SKP would like to acknowledge the Associate Program, IUCAA for supporting his visit to IIT, Kgp and CTS, IIT Kgp for the use of its facilities.

References

Bharadwaj, S., Nath, B., Sethi, S. K. 2001, *JApA*. **22,** 21.
Bharadwaj, S., Sethi, S. K. 2001, *JApA*, **22,** 293.
Bunn, E. F., White, M. 1996, *Astrophys. J.*, **460,** 1071.
Efstathiou, G., Bond, J. R., White, S. D. M. 1992, *MNRAS*, **250,** 1p.

Lahav, O., Lilje P. B., Primack J. R., Rees M., 1991, *MNRAS*, **251,** 128.
Lanzetta, K. M., Wolfe, A. M., Turnshek, D. A. 1995, *Astrophys. J.*, **430,** 435.
Peebles, P. J. E. 1980, *The Large-Scale Structure of the Universe* (Princeton: Princeton University Press)
Péroux, C., McMahon, R. G., Storrie-Lombardi, L. J., Irwin, M. J. 2001, *MNRAS* astro-ph/0107045
Saini, T., Bharadwaj, S., Sethi, K. S. 2001, *Astrophys. J.*, **557,** 421.
Storrie–Lombardi, L. J., McMahon, R. G., Irwin, M. J. 1996, *MNRAS*, **283,** L79.
Swarup, G., Ananthakrishan, S., Kapahi, V. K., Rao, A. P., Subrahmanya, C. R., Kulkarni, V. K. 1991, *Curr. Sci.*, **60,** 95.

J. Astrophys. Astr. (2003) **24,** 37–43

GMRT Detection of HI 21 cm Associated Absorption towards the $z = 1.2$ Red Quasar 3C 190

C. H. Ishwara-Chandra[1], K. S. Dwarakanath[2] & K. R. Anantharamaiah[2]*

[1]*National Center for Radio Astrophysics, TIFR, Post Bag 3, Ganeshkhind, Pune 411 007, India. e-mail: ishwar@ncra.tifr.res.in*
[2]*Raman Research Institute, Sadashivanagar, Bangalore 560 080, India.*
e-mail: dwaraka@rri.res.in

Received 2003 March 27; accepted 2003 June 5

Abstract. We report the GMRT detection of associated HI 21 cm-line absorption in the $z = 1.1946$ red quasar 3C 190. Most of the absorption is blue-shifted with respect to the systemic redshift. The absorption, at ~ 647.7 MHz, is broad and complex, spanning a velocity width of $\sim 600\,\mathrm{km s^{-1}}$. Since the core is self-absorbed at this frequency, the absorption is most likely towards the hotspots. Comparison of the radio and deep optical images reveal linear filaments in the optical which overlap with the brighter radio jet towards the south-west. We therefore suggest that most of the HI 21 cm-line absorption could be occurring in the atomic gas shocked by the south-west jet.

Key words. Galaxies: active—quasars: absorption lines—radio lines: galaxies—quasars: individual (3C190).

1. Introduction

It was suggested more than three decades ago that the study of HI 21 cm-line absorption at high redshifts would provide interesting and important information regarding the distribution and kinematics of neutral hydrogen at earlier epochs (Bahcall & Ekers 1969). The central regions of active galactic nuclei (AGN) are important in understanding many aspects of AGN phenomena like the fueling on to the accretion disk and the obscuration of the nuclei as proposed in the unified scheme. One way to study the central region in AGNs is to search for HI 21 cm-line absorption at the redshift of the AGN host galaxy against the radio source. The absorption can be due to a variety of phenomena like tori, outflows, the inter stellar medium (ISM), cold clouds and cold gas stirred up during merging of neighbors with the host galaxy (cf. Morganti *et al.* 2001).

The red quasars have generated interest particularly since the work of Webster *et al.* (1995) claiming that a large fraction ($\sim 80\%$) of quasars could be missed from optical surveys due to dust extinction. It is believed that in this class of quasars, the extinction

---

*Since deceased.

due to dust is higher (Webster *et al.* 1995); however, there are claims that red quasars are not necessarily dusty (e.g., Benn *et al.* 1998). If the red quasars are dusty, then the number of high column density absorption-line systems seen towards optically selected quasars will also be an underestimate. Carilli *et al.* (1998; hereinafter C98) have searched for HI 21 cm-line absorption in a radio-loud red quasar subsample at moderate redshifts ($z \sim 0.7$) to address whether the 'red' AGNs are intrinsically red or reddened by dust. In their sample of five red quasars, four showed significant HI absorption, suggesting the presence of large amounts of gas and associated dust. Even though the number is small, this study showed that the success rate for detecting HI 21 cm-line absorption in radio-loud red quasars is higher (80%) compared to an optically selected sample of radio-loud quasars with Mg II or Lyman alpha absorption (C98, Carilli *et al.* 1999). This opens up a new class of objects which can be studied in 21-cm absorption at higher redshifts, where the optically selected sample has strong bias against high column density systems with high dust-to-gas ratios (Fall & Pei 1993, 1995).

We have started a program to search for HI 21 cm-line absorption in a sample of high redshift ($z > 1$) radio-loud 'red' quasars and galaxies with the Giant Meterwave Radio Telescope (GMRT, Swarup *et al.* 1991). At higher redshifts, the optical/IR morphologies of the host galaxies tend to be more complex, possibly due to ongoing merging activity leading to the formation of massive ellipticals at later epochs (Chambers & Miley 1990). Such activity (i) might enhance the probability of detecting HI 21 cm-line absorption (e.g., Carilli & van Gorkom 1992) and (ii) could also contribute to reddening.

3C 190 is a compact steep spectrum (CSS) radio source. Its largest angular size is 4.0 arcsec and corresponding linear size is 33 kpc (assuming $H_\circ = 71\,\mathrm{kms}^{-1}$, $\Omega_m = 0.27$ and $\Omega_{\mathrm{vac}} = 0.73$). The bright hotspots are separated by 2.6 arcsec, or a linear size of 22 kpc which means the hotspots may be just within the envelope of the host galaxy (Spencer *et al.* 1991). Compact steep spectrum sources and compact symmetric objects appear to show a high incidence of HI absorption (Conway 1996). High resolution radio observations of 3C 190 suggest one-sided jet-like structure towards the south-west of the core (Spencer *et al.* 1991). The large scale jet in this direction is also brighter. The core is self-absorbed at 608 MHz (Nan Rendong *et al.* 1991). There appears to be significant bending between the milli-arcsec scale jet and the kpc scale jet. The milli-arcsec scale jet is directed towards the west (Hough *et al.* 2002), while on larger scales the jet has bent towards south-west ending with multiple hotspots. The diffuse lobe in this direction is further towards south-west (~ 1.5 arcsec) and also misaligned (Spencer *et al.* 1991). This is suggestive of the presence of a dense inter stellar medium (ISM) causing the jet to bend. Recent detailed optical spectroscopy of this object showed narrow [O II], [Ne III] and C III] emission lines, which provide a redshift of 1.1946 ± 0.0005 (Stockton & Ridgway 2001). In addition, Mg I, Fe II and strong Mg II absorption has also been detected, but at a slightly higher redshift of 1.19565 ± 0.00004, corresponding to an infall velocity of 145 kms^{-1} in the quasar frame (Stockton & Ridgway 2001). We adopt the redshift of 1.1946 ± 0.0005 determined from narrow emission lines as the systemic redshift of the quasar. Its optical to infrared continuum falls steeply, causing it to be classified as a "red" quasar (Simpson & Rawlings 2000; Smith & Spinrad 1980). The presence of strong Mg II absorption close to the systemic redshift suggests the presence of intervening gas and dust, which may also be responsible for reddening the quasar spectrum and causing the bending of radio jets. A higher chance of detection of HI 21 cm-line absorption from 3C 190 was foreseen due to two factors: (i) it is a CSS radio source. Associated optical/UV absorption is most common in CSS quasars among radio-loud quasars (Baker *et al.* 2002), and CSS also shows a higher chance of detecting HI 21 cm-line absorption (Conway 1996), (ii) it is also a "red" quasar which again shows a higher chance of detecting HI 21 cm-line absorption (C98).

In this paper, we report the detection of HI 21 cm-line absorption from the red quasar 3C 190, which is blue-shifted with respect to the systemic redshift. In section 2 observations and results are presented. The HI 21 cm-line absorption detected in 3C 190 is discussed in section 3. Conclusions are presented in section 4.

2. Observations and results

The observations were carried out using the Giant Meterwave Radio Telescope (GMRT) during September 2001. The first set of observations adopted a bandwidth of 4 MHz centered at 647.5 MHz. Subsequently, two sets of observations each with a bandwidth of 8 MHz centered at 646.7 MHz and 648.7 MHz were repeated to confirm the detection from the first set of observations. The integration time on source was ~ 3 hr in each set of observations. The velocity resolutions were $\sim 29\,\mathrm{kms}^{-1}$ and $\sim 14.5\,\mathrm{kms}^{-1}$ for bandwidths of 8 MHz and 4 MHz respectively. The flux densities were estimated by observing the standard primary calibrators 3C 286 or 3C 48. The bandpass calibrators 3C 48, 3C 147 and 3C 286 were observed at the beginning as well as at the end of the observation in order to check for bandpass stability with time. Phase calibrators were observed for 10 minutes every 30 minutes.

The data obtained from the GMRT were converted to FITS and analysed using the Astronomical Image Processing System (AIPS) following standard procedures. About 20 line-free channels were collapsed to obtain a continuum image. A few iterations of phase-only self-calibration were performed followed by amplitude and phase self-calibration. These calibrations were then applied to the spectral line data. The continuum flux density of 3C 190 at 647 MHz is 5.69 Jy. The continuum flux density for subtracting from the spectral data was obtained by averaging several line-free channels. The final spectral cube was made from this continuum subtracted data.

Initially, individual spectra were obtained from the two 8 and one 4 MHz observations to check for consistency. The individual spectra were then averaged to obtain the final spectrum which is presented in Fig. 1. The systemic redshift and the relative velocity of the associated optical absorption system (Stockton & Ridgway 2001) are marked in Fig. 1. The RMS noise in the averaged spectrum is ~ 2 mJy/beam/channel. We have used the standard GIPSY package to fit Gaussians to the observed spectra. A minimum of 5 Gaussians were required to minimise the residuals. The estimated parameters of the fit are given in Table 1.

The most interesting finding from our observations is that most of the HI 21 cm-line absorption in 3C 190 is blue-shifted with respect to the systemic redshift (Fig. 1). The peak of the absorption occurs at a velocity of $-210\,\mathrm{kms}^{-1}$, but the overall absorption is very broad, extending from $-400\,\mathrm{kms}^{-1}$ to $+200\,\mathrm{kms}^{-1}$. The velocity uncertainties in systemic redshift is $68\,\mathrm{kms}^{-1}$ and that of Mg II absorption system is $5.5\,\mathrm{kms}^{-1}$. The components 1, 2 and 3 are significantly blue-shifted with respect to the systemic redshift, while component 4 is within the uncertainty in the systemic redshift. Component 5 at $127\,\mathrm{kms}^{-1}$ is outside the uncertainty in the Mg II absorption system and

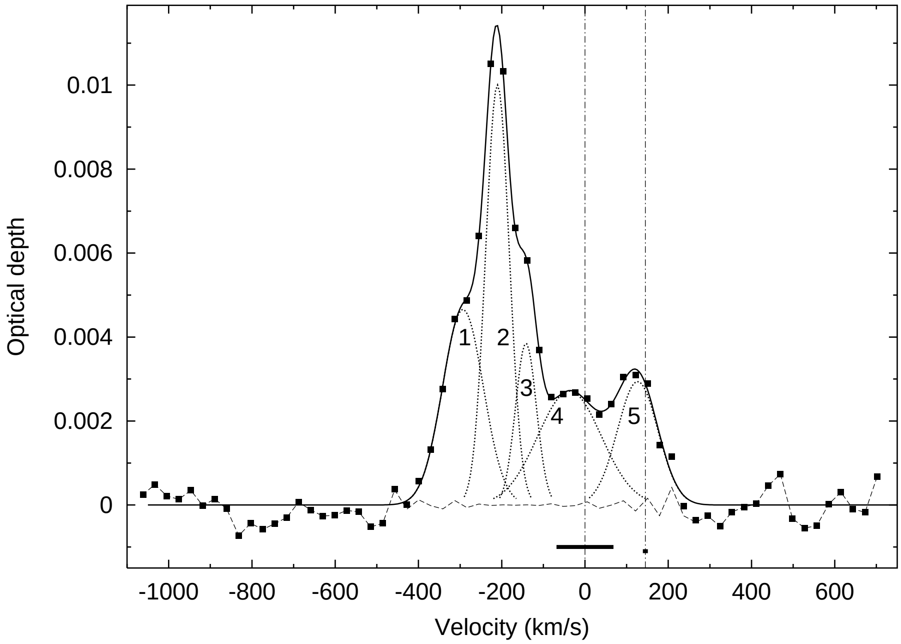

Figure 1. The HI absorption spectrum toward the red quasar 3C 190 (indicated by filled squares). The solid line is the five component Gaussian fit to the data and the dotted lines are the individual Gaussian components which are numbered. Dashed line is the residual to the fit. The optical depth was estimated using the peak flux of 5.69 Jy. The systemic redshift is taken as 1.1946 ± 0.0005 obtained from narrow [O II], [Ne III] and C III] emission lines, which is indicated as dot-dashed vertical line at the velocity of 0 kms^{-1}. Similar vertical line at a velocity of 145 kms^{-1} corresponds to the Mg II absorption. Thick horizontal lines centered at 0 and 145 kms^{-1} indicates one sigma range of velocity at systemic redshift and that at Mg II absorption.

Table 1. Parameters derived from the Gaussian fitting to the optical depth profile towards 3C 190. Zero velocity corresponds to the systemic redshift of 1.1946.

Line	Velocity (kms^{-1})	FWHM (kms^{-1})	τ
Comp 1	-293.1 ± 2.8	115.1 ± 6.9	0.0047 ± 0.0002
Comp 2	-210.2 ± 1.0	66.8 ± 2.2	0.0100 ± 0.0003
Comp 3	-141.8 ± 2.2	59.4 ± 5.0	0.0043 ± 0.0003
Comp 4	$-\ 37.1 \pm 5.7$	179.4 ± 13.3	0.0027 ± 0.0002
Comp 5	126.5 ± 4.2	114.6 ± 9.8	0.0029 ± 0.0002

the uncertainty in the systemic redshift. The three blue-shifted lines also have larger optical depths than lines 4 and 5. Component 1 at $-293\,\text{kms}^{-1}$ has an optical depth of ~ 0.005 and the second component at $-210\,\text{kms}^{-1}$ has an optical depth of ~ 0.01. The optical depth of component 3 is comparable to that of component 1, but FWHM is nearly half of component 1. Components 2 and 3 have comparable FWHM, but optical depth of component 3 is less than half of component 2. The FWHM of fifth component is comparable to component 1, with optical depth nearly half. Component 4 is well within uncertainty in the systemic redshift, and is the broadest of all components with FWHM of 179 kms^{-1}.

3. Discussion

A few cases of blue-shifted HI 21 cm-line absorption with respect to the systemic redshift are reported in the literature. A nearby CSS ($z = 0.06393$) PKS B1814–63, exhibits an HI absorption spectrum similar to that seen in 3C 190, viz., a broad shallow feature and blue-shifted deep absorption (Morganti *et al.* 2001). A similar absorption profile is also seen in the radio galaxy 4C 12.50 (Mirabel 1989) where the overall absorption extends over 900 kms^{-1}. Another compact radio galaxy, 3C 459, also shows HI absorption blue-shifted with respect to systemic redshift, though weaker than PKS 1814–63 (Morganti *et al.* 2001). The authors suggest that the blue-shift could be due to outflow, possibly associated with the jet/lobes, and the shallow component seen at the systemic redshift is due to a circumnuclear disk. Significantly blue-shifted HI 21 cm-line absorption has also been seen in several Seyfert galaxies. In IC 5063, the HI 21 cm-line absorption is blue-shifted by more than 600 kms^{-1} (Oosterloo *et al.* 2000) with respect to the systemic redshift. They suggest that the HI 21 cm-line absorption could be occurring from the gas which has been shocked by the western radio jet. The moderate blue-shift of HI 21 cm-line absorption observed in NGC 1068 and NGC 3079 is suggested to be due to neutral gas participating in the outflow (Gallimore *et al.* 1994).

In the case of 3C 190, the striking aspect is that the HI 21 cm-line absorption is broad and complex and most of the absorption is blue-shifted with respect to systemic redshift (Fig. 1). The total velocity extent is about 600 kms^{-1}. The absorption is not against the core because the core is self-absorbed at this frequency. The flux limit for the core is < 4 mJy (Nan Rendong *et al.* 1991), whereas the absorbed flux is up to 70 mJy. In the current observations, 3C 190 remains unresolved. In the arcsec resolution map of 3C 190, there are two hotspots in the south-west direction, and are brighter than the north-east hotspot (Spencer *et al.* 1991). The fluxes of individual hotspots are about a Jy and more at 608 MHz (Nan Rendong *et al.* 1991). The total projected extent of hotspots in the south-west and north-east is about 22 kpc, hence these hotspots may lie within the envelope of the host galaxy environment. At this linear scale, there is also evidence for diffuse radio emission (Pearson *et al.* 1985) which is mostly north of the radio core. Significant HI 21 cm-line absorption can occur against one or all of these. The diffuse lobe in the south west is further away (1.5 arcsec) from bright hotspots (Pearson *et al.* 1985), and may lie outside the host galaxy, hence it is less likely to expect HI 21 cm-line absorption against this diffuse lobe.

Even though it is not possible to say which absorption-line is towards which radio component, we can draw indirect conclusions from the known radio and optical morphologies and properties. From the radio image at arc-sec resolution, we see that the south-west diffuse lobe and the farthest hotspot in this direction are mis-aligned (Spencer *et al.* 1991). The immediate surroundings of 3C 190 have been studied in imaging as well as in spectroscopy in great detail using HST and Keck (Stockton & Ridgway 2001). The most interesting feature revealed from the HST observations is a linear knotty optical filament along north-west, very close to the quasar and overlapping (in projection) with the south-west hotspot. Spectroscopy of the linear filament reveals interesting features. The [O II] line profile clearly divides into low velocity dispersion ($\sigma \sim 40\,\mathrm{kms}^{-1}$) and high velocity dispersion ($\sigma \sim 200\,\mathrm{kms}^{-1}$) groups. The higher velocity dispersion indicates that the gas might have been shocked in some way by the interaction with the jet thereby increasing the turbulent velocity in this region significantly. In the radio map also, there is evidence for jet bending in this region (Stockton & Ridgway 2001), which indicates the presence of a dense medium.

Thus it appears that the overall environment under which the HI 21 cm-line absorption is occurring in 3C 190 appears to be similar to that of IC 5063, where neutral gas has been shocked by the radio jet. Velocities up to $500\,\mathrm{kms}^{-1}$ are expected from shocks (Dopita & Sutherland 1995). Due to shocks, the neutral gas could acquire significant bulk motion but the internal velocities might not increase significantly. Such clouds could produce reasonably narrow lines (FWHM $\sim 100\,\mathrm{kms}^{-1}$ or less), but significantly blue-shifted, such as the lines 1, 2 and 3 in 3C 190 (Table 1), where the FWHM is 115, 67 and $59\,\mathrm{kms}^{-1}$ respectively, but are blue-shifted by 293, 210 and $142\,\mathrm{kms}^{-1}$ with respect to the systemic redshift.

The optical linear filament which shows high velocity dispersion gas overlaps (in projection) with the south-west hotspot (Stockton & Ridgway 2001). This is suggestive of interaction of the jet with the dense ambient medium responsible for changing the direction of the jet. Thus we can expect that the three blue-shifted absorption-lines (1, 2 and 3) in 3C 190 could be arising from this region. Only one of the absorption-line component (component 4) in 3C 190 is very broad (FWHM of $179\,\mathrm{kms}^{-1}$). This component is well within the uncertainty in the systemic redshift and could be due to more turbulent gas near the region of interaction of radio jet with the ambient medium. Thus, we suggest that lines 1, 2, 3 and 4 are likely to be against the south-west hotspots. The fifth line has a velocity of $127\,\mathrm{kms}^{-1}$, which is outside the uncertainty of Mg II absorption system and the uncertainty in the systemic redshift. Since the FWHM of this line is not too narrow ($115\,\mathrm{kms}^{-1}$), it could be from the ISM of the host galaxy.

4. Conclusions

We have reported the GMRT detection of HI 21 cm-line absorption in the $z = 1.1946$ red quasar 3C 190. The absorption, with peak at ~ 647.7 MHz, is broad and complex, spanning a velocity width of $\sim 600\,\mathrm{kms}^{-1}$. Most of the absorption is blue-shifted with respect to the systemic redshift. 3C 190 is unresolved with the present observations. Since the core is self-absorbed at this frequency the absorption must be towards the hotspots. Comparison of the radio and deep optical images reveals linear filaments in the optical which overlap with the brighter radio jet in the south-west direction. We therefore suggest that the blue-shifted HI 21 cm-line absorption could be occurring in the atomic gas shocked by the south-west jet.

Acknowledgements

We thank Rajaram Nityananda, Jayaram Chengalur and Chris Carilli for comments on the manuscript. We thank the referee for meticulously reading the manuscript and for constructive suggestions. We thank the staff of the GMRT that made these observations possible. GMRT is run by the National Center for Radio Astrophysics of the Tata Institute of Fundamental Research. This research has made use of the NASA/IPAC

Extragalactic Database (NED) which is operated by the Jet Propulsion Laboratory, California Institute of Technology, under contract with the National Aeronautics and Space Administration (NASA).

References

Bahcall, J. N., Ekers, R. D. 1969, *Astrophys. J.*, **157,** 1055.

Baker, J. C., Hunstead, R. W., Athreya, R. M., Barthel, P. D., de Silva, E., Lehnert, M. D., Saunders, R. D. E. 2002, *Astrophys. J.*, **568,** 592.

Benn, C. R., Vigotti, M., Carballo, R., Gonzalez-Serrano, J. I., Sánchez, S. F. 1998, *MNRAS*, **295,** 451.

Carilli, C. L., van Gorkom, J. H. 1992. *Astrophys. J.*, **399,** 373.

Carilli, C. L., Menten, K. M., Reid, M. J., Rupen, M. P., Yun, M. S. 1998, *Astrophys. J.*, **494,** 175.

Carilli, C. L., Menten, K. M., Moore, C. P. 1999, in *Highly redshifted radio lines*, (eds.) C. L. Carilli, S. J. E. Radford, K. M. Menten, G. I. Langston, ASP Conference Series, Vol. 156, p. 171.

Chambers, K. C., Miley, G. K. 1990, in *The Evolution of the Universe of Galaxies*, (eds.) R. G. Kron, ASP Conference Series, Vol. 10, p. 373.

Conway, J. E. 1996, in *The second workshop on Gigahertz Peaked Spectrum and Compact Steep Spectrum Radio Sources*, (eds.) I. A. G. Snellen, R. T. Schilizzi, H. J. A. Rottgering, M. N. Bremer, Leiden Observatory, p. 98.

Dopita, M. A., Sutherland, R. S. 1995, *Astrophys. J.*, **455,** 468.

Fall, S. M., Pei, Y. C. 1993, *Astrophys. J.*, **402,** 479.

Fall, S. M., Pei, Y. C. 1995, in *QSO Absorption Lines*, (eds.) G. Meylan, (Berlin Heidelberg: Springer-Verlag) p. 23.

Gallimore, J. F., Baum, S. A., O'Dea, C. P., Brinks, E., Pedlar, A. 1994, *ApJL*, **422,** L13.

Hough, D. H., Vermeulen, R. C., Readhead, A. C. S., Cross, L. L., Barth, E. L., Yu, L. H., Beyer, P. J., Phifer, E. M. 2002, *Astr. J.*, **123,** 1258.

Mirabel, I. F. 1989, *Astrophys. J.*, **340,** L13.

Morganti, R., Oosterloo, T. A., Tadhunter, C. N., van Moorsel, G., Killeen, N., Wills, K. A. 2001, *MNRAS*, **323,** 331.

Nan Rendong, Schilizzi, R. T., Fanti, C., Fanti, R. 1991, *Astr. Astrophys.*, **252,** 513.

Oosterloo, T. A., Morganti, R., Tzioumis, A., Reynolds, J., King, E., McCulloch, P., Tsvetanov, Z. 2000, *Astr. J.*, **119,** 2085.

Pearson, T. J., Readhead, A. C. S., Perley, R. A., 1985. *Astr. J.*, **90,** 738.

Simpson, C., Rawlings, S. 2000, *MNRAS*, **317,** 1023.

Smith, H. E., Spinrad, H. 1980, *Astrophys. J.*, **236,** 419.

Spencer, R. E., Schilizzi, R. T., Fanti, C., Fanti, R., Parma, P., van Breugel, W. J. M., Venturi, T., Muxlow, T. W. B., Rendong, Nan. 1991, *MNRAS*, **250,** 225.

Stockton, A., Ridgway, S. E. 2001, *Astrophys. J.*, **554,** 1012.

Swarup, G., Ananthakrishnan, S., Kapahi, V. K., Rao, A. P., Subrahmanya, C. R., Kulkarni, V. K. 1991, *Curr. Sci.*, **60,** 95.

Webster, R. L., Francis, P. J., Peterson, B. A., Drinkwater, M. J., Masci, F. J. 1995, *Nature*, **375,** 469.

J. Astrophys. Astr. (2003) **24,** 51–67

Large Scale Magnetic Fields: Density Power Spectrum in Redshift Space

Rajesh Gopal & Shiv K. Sethi *Raman Research Institute, Bangalore 560 080, India.*
e-mail: rajesh@rri.res.in sethi@rri.res.in

Received 2003 September 5; accepted 2004 January 6

Abstract. We compute the density redshift-space power spectrum in the presence of tangled magnetic fields and compare it with existing observations. Our analysis shows that if these magnetic fields originated in the early universe then it is possible to construct models for which the shape of the power spectrum agrees with the large scale slope of the observed power spectrum. However requiring compatibility with observed CMBR anisotropies, the normalization of the power spectrum is too low for magnetic fields to have significant impact on the large scale structure at present. Magnetic fields of a more recent origin generically give density power spectrum $\propto k^4$ which doesn't agree with the shape of the observed power spectrum at any scale. Magnetic fields generate curl modes of the velocity field which increase both the quadrupole and hexadecapole of the redshift space power spectrum. For curl modes, the hexadecapole dominates over quadrupole. So the presence of curl modes could be indicated by an anomalously large hexadecapole, which has not yet been computed from observation.

It appears difficult to construct models in which tangled magnetic fields could have played a major role in shaping the large scale structure in the present epoch. However if they did, one of the best ways to infer their presence would be from the redshift space effects in the density power spectrum.

Key words. Cosmology: theory—large-scale structure of the universe — magnetic fields—MHD.

1. Introduction

Magnetic fields play an important dynamical role in shaping most structures in the universe (see e.g., Parker 1979). The largest scale spatially coherent fields are seen in galaxies and galaxy clusters with coherence lengths $\simeq$ 10–100 kpc (for a recent review see Widrow 2002). Though there is also some evidence of coherent magnetic fields on super-cluster scales (Kim *et al.* 1989), the existence of magnetic fields at larger scales ($\gtrsim 1$ Mpc) cannot generally be inferred from direct observations (for a summary of results see Kronberg 1994; Widrow 2002). The most direct method to infer the presence of intergalactic magnetic fields for $z \lesssim 3$ is to study the Faraday rotation of polarized emission from extra-galactic sources (Rees & Reinhardt 1972;

Kronberg & Simard-Normandin 1976; Vallée 1990; Blasi, Burles & Olinto 1999). The existence of these fields can also be constrained at the last scattering surface from CMBR anisotropy measurements and upper limits on the CMBR spectral distortion (Barrow, Ferreira & Silk 1997; Subramanian & Barrow 1998; Jedamzik, Katalinić & Olinto 2000). Large scale magnetic fields also cause Faraday rotation of the polarized component of the CMBR anisotropies (Kosowsky & Loeb 1996). If magnetic fields existed at even higher redshifts, they can also affect the primordial nucleosynthesis (see e.g., Widrow 2002 for detailed discussion).

The origin of these large scale fields is not clear. They could arise from dynamo amplification of small seed fields (see e.g., Parker 1979; Zeldovich, Ruzmaikin & Sokolov 1983; Ruzmaikin, Sokolov & Shukurov 1988) or these fields have their origin in very early universe and their flux-frozen evolution result in presently observed fields (see e.g., Turner & Widrow 1988; Ratra 1992).

Wasserman (1978) considered the effect of large scale magnetic fields on the formation of structures in the universe. This study showed that nano-gauss fields could provide initial conditions for density and velocity perturbations which could gravitationally collapse to form galaxies at the present epoch. Kim, Olinto & Rosner (1996) calculated the density power spectrum in the presence of magnetic fields. Sethi (2003) studied the effect of magnetic fields on the two-point correlation function of galaxies.

Two-point functions in real and Fourier space remain the most important tools to understand the formation of structures in the universe (see e.g., Peebles 1980). Recently large galaxy survey 2dF (Colless *et al.* 2001) has computed these functions with unprecedented precision. In particular one of the most important results from the 2dF survey is the unambiguous detection of anisotropy in the two-point functions, which is the best statistical evidence of the large scale velocity field (Peacock *et al.* 2001; Hawkins *et al.* 2002). The on-going survey Sloan digital sky survey (SDSS) is likely to improve upon this result owing to its larger size (York *et al.* 2000). The results of 2dF survey show good agreement with the theoretical predictions of variants of CDM models (see e.g., Lahav *et al.* 2002), in which initial density perturbations are produced at the time of inflation in the very early universe. Larger surveys like the on-going SDSS have the potential to uncover the small discrepancy between theory and observations.

In this paper we study the possibility that initial density and velocity perturbations were caused by tangled magnetic fields. In particular we estimate the density power spectrum in redshift space from these perturbations for two classes of models and compare with present observations. In one class of models we assume the magnetic fields to have originated in very early universe; we also consider simple models in which the magnetic fields could be of more recent origin and could have originated by astrophysical processes at $z \lesssim 10$. This study could be considered a continuation of the early studies of Kim *et al.* (1996) who calculated density power spectrum in real space and Sethi (2003) who computed the density two-point correlation function in redshift space.

In the next section we discuss the magneto-hydrodynamics equations and the evolution of density and velocity fields in the presence of tangled magnetic fields. In section 3 we discuss the properties of spatial correlations of the density and velocity fields and their impact on redshift space power spectrum and give our main results. In section 4 we summarize our conclusions. Throughout this paper we use the currently-favoured background cosmological model: spatially flat with $\Omega_m = 0.3$ and $\Omega_\Lambda = 0.7$

(Perlmutter *et al.* 1999; Riess *et al.* 1998). For numerical work we use $\Omega_b h^2 = 0.02$ (Tytler *et al.* 2000) and $h = 0.7$ (Freedman *et al.* 2001).

2. Magneto-hydrodynamics equations

In co-moving coordinates, the equations of magneto-hydrodynamics in the linearized Newtonian theory are (Wasserman 1978):

$$\frac{d(a\mathbf{v}_b)}{dt} = -\nabla\phi + \frac{(\nabla \times \mathbf{B}) \times \mathbf{B}}{4\pi\rho_b}, \tag{1}$$

$$\nabla \cdot \mathbf{v}_b = -a\dot{\delta}_b, \tag{2}$$

$$\nabla^2\phi = 4\pi G a^2 (\rho_{\rm DM}\delta_{\rm DM} + \rho_b\delta_b), \tag{3}$$

$$\frac{\partial(a^2\mathbf{B})}{\partial t} = \frac{\nabla \times (\mathbf{v}_b \times a^2\mathbf{B})}{a}, \tag{4}$$

$$\nabla \cdot \mathbf{B} = 0. \tag{5}$$

In equation (1) the pressure gradient from matter is neglected as it is important at Jeans' length scales ($k \gg 1\,\mathrm{Mpc}^{-1}$ before re-ionization and $\simeq 1\,\mathrm{Mpc}^{-1}$ after re-ionization). Our interest here is to study scales at which the perturbations are linear at the present epoch, $\gtrsim 10\,\mathrm{h}^{-1}$ Mpc or $k \lesssim 0.2\,\mathrm{h\ Mpc}^{-1}$. Equation (1) and equation (2) can be combined to give:

$$\frac{\partial^2\delta_b}{\partial t^2} + 2\frac{\dot{a}}{a}\frac{\partial\delta_b}{\partial t} - 4\pi G(\rho_{\rm DM}\delta_{\rm DM} + \rho_b\delta_b) = \frac{\nabla.[(\nabla \times \mathbf{B}) \times \mathbf{B}]}{4\pi a^2\rho_b}. \tag{6}$$

Here the subscript 'b' refers to the baryonic component and the subscript 'DM' refers to the dark matter component. Fluid equations for the evolution of dark matter perturbations can be obtained from the equations above by dropping the magnetic field terms (Peebles 1980). Wasserman (1978) showed that equation (6) admits a growing solution, i.e., tangled magnetic fields can provide initial conditions for the growth of density perturbations. These solutions are discussed in the next section. In equation (4) we have assumed the medium to have infinite conductivity. It can be simplified further by dropping the right hand side of the equation as it is of higher order, this gives:

$$\mathbf{B}(x, t)a^2 = \text{constant}. \tag{7}$$

We assume the tangled magnetic field to be a statistically homogeneous and isotropic vector random process. In this case the two-point correlation function of the field in Fourier space can be expressed as (Landau & Lifshitz 1987):

$$\langle B_i(\mathbf{q})B_j^*(\mathbf{k})\rangle = \delta_D^3(\mathbf{q} - \mathbf{k})\left(\delta_{ij} - q_iq_j/q^2\right)B^2(q). \tag{8}$$

In addition we assume the tangled magnetic fields to obey Gaussian statistics.

2.1 *Time evolution of density and velocity perturbations*

The space and time dependence in the solution of equation (6) can be separated. Equation (6) contains two source terms: dark matter perturbations and tangled magnetic fields. A similar equation for the dark matter perturbations contains baryonic perturbations as the source term.

$$\begin{aligned}\frac{\partial^2\delta_b}{\partial t^2} &= -2\frac{\dot{a}}{a}\frac{\partial\delta_b}{\partial t} + 4\pi G(\rho_{\mathrm{DM}}\delta_{\mathrm{DM}} + \rho_b\delta_b) + S(t,x),\\ \frac{\partial^2\delta_{\mathrm{DM}}}{\partial t^2} &= -2\frac{\dot{a}}{a}\frac{\partial\delta_{\mathrm{DM}}}{\partial t} + 4\pi G(\rho_{\mathrm{DM}}\delta_{\mathrm{DM}} + \rho_b\delta_b).\end{aligned} \tag{9}$$

Here $S(t, x)$ is the source term from magnetic fields. The dark matter is not directly affected by the magnetic fields. To solve these equations, we define $\delta_m = (\rho_{\mathrm{DM}}\delta_{\mathrm{DM}} + \rho_b\delta_b)/\rho_m$ with $\rho_m = (\rho_{\mathrm{DM}} + \rho_b)$. This leads to:

$$\begin{aligned}\frac{\partial^2\delta_b}{\partial t^2} &= -2\frac{\dot{a}}{a}\frac{\partial\delta_b}{\partial t} + 4\pi G\rho_m\delta_m + S(t,x),\\ \frac{\partial^2\delta_m}{\partial t^2} &= -2\frac{\dot{a}}{a}\frac{\partial\delta_m}{\partial t} + 4\pi G\rho_m\delta_m + \frac{\rho_b}{\rho_m}S(t,x).\end{aligned} \tag{10}$$

The second of these equations can be solved by the usual Green's function methods. Its solution is:

$$\begin{aligned}\delta_m(x,t) = A(x)D_1(t) + B(x)D_2(t) - D_1(t)\int_{t_i}^{t} dt'\frac{S(t',x)D_2(t')}{W(t')}\\ + D_2(t)\int_{t_i}^{t} dt'\frac{S(t',x)D_1(t')}{W(t')}.\end{aligned} \tag{11}$$

Here $W(t) = D_1(t)\dot{D}_2(t) - D_2(t)\dot{D}_1(t)$ is the Wronskian. $D_1(t)$ and $D_2(t)$ are the solutions of the homogeneous part of the δ_m evolution (Peebles 1980). These terms have the space dependence corresponding to initial, presumably originated during inflation, perturbations. There is no reason to expect that there will be any correlation between these perturbations and the tangled magnetic field-induced perturbations. And therefore in the two-point functions these two contributions will add in quadrature. We only consider magnetic field-induced perturbations for our analysis and drop the first two terms from equation (11). In equation (11), t_i corresponds to the epoch of recombination as compressional modes cannot grow before that epoch (see e.g., Subramanian & Barrow 1998). So our initial conditions are: $\delta(t_i) = \dot{\delta}(t_i)$, as is evident from equation (11). The solution to equation (11) can be readily calculated analytically for $\Omega_m = 1$ universe (Wasserman 1978). For the currently favoured cosmological model – spatially flat with non-zero cosmological constant – these solutions have to be found numerically. The evolution of δ_b can be solved from:

$$\frac{1}{a^2}\frac{\partial}{\partial t}\left(a^2\frac{\partial\delta_b}{\partial t}\right) = \frac{3}{2}H^2\delta_m + S(t,x). \tag{12}$$

Here we have used: $H^2 = (8\pi G/3)\rho_m$. At high redshifts, solutions to equation (12) can be found analytically and allow us some insight into the numerical solutions. For $z \gg 1$ the fastest growing solution of equation (12) is $\propto \Omega_b/\Omega_m^2 t^{2/3}$. It shows that in the presence of the dark matter, perturbations in baryonic matter are suppressed by a factor Ω_b/Ω_m^2.

Tangled magnetic fields give rise to both compressional and curl velocity fields. The time dependence of these two modes is different. The time dependence of the compressional velocity mode v_d can be found from the continuity equation (equation 2) and equation (11). For $\Omega_m = 1$ model, the compressional modes grow as $a^{1/2}$. In the presence of dark matter, their growth like the density mode is suppressed by a factor Ω_b/Ω_m^2.

The time evolution of the curl part of the velocity can be found by either taking the curl of equation (1) or in Fourier space project the transverse part of the velocity field (see below). The time dependence of the resulting equation is readily solved:

$$v_c(t) = a(t)^{-1} \int_{t_i}^{t} \frac{dt'}{a^{-3}(t')} S(t', x) \tag{13}$$

v_c doesn't have any growing mode. In the $\Omega_m = 1$ model $v_c \propto a^{-1/2}$. Unlike the density and compressional velocity modes it doesn't suffer any suppression in the presence of dark matter.

The time evolution of density and velocity fields is shown in Fig. 1. In case the tangled magnetic fields originated in the very early universe, the effect of the non-

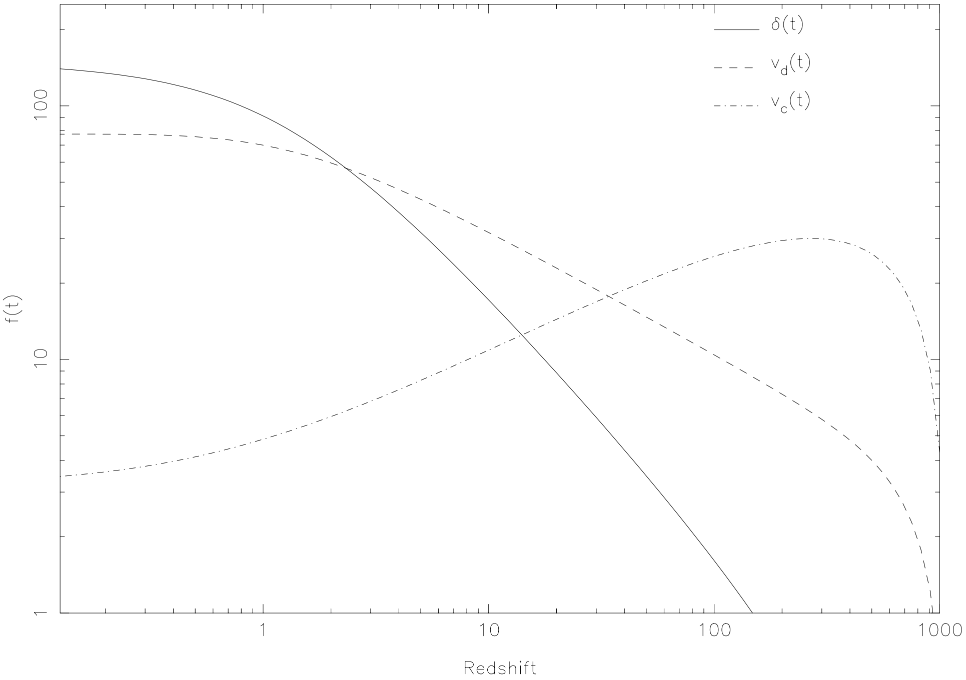

Figure 1. Evolution of density and velocity fields is shown if the tangled magnetic fields existed at the last scattering surface.

compressional modes generated by the magnetic fields would be negligible on the large scale structure at the present epoch, as these modes would have decayed by the present. Only if the magnetic fields are of more recent origin, these modes could have played an important part in the dynamics of large scale structure.

3. Density and velocity fields

The density and velocity fields are statistically homogeneous and isotropic random processes in real space. This allows one to define the power spectrum of the density field, $P(k)$, as (see e.g., Peebles 1980):

$$\langle \delta(\mathbf{k})\delta(\mathbf{k}')\rangle = (2\pi)^3 P(k)\delta_D^3(\mathbf{k}+\mathbf{k}'). \tag{14}$$

In redshift space both statistical homogeneity and isotropy of the density field break down (see e.g., Hamilton 1998). In the plane parallel approximation (Kaiser 1987), the density field is only statistically anisotropic. This is generally a good assumption in analysing large scale data (Hamilton 1998). We make this assumption in our analysis here. In linear theory and in the plane parallel approximation the observed density field, i.e., the redshift space density field, $\delta^s(\mathbf{r})$ can be written in terms of the real space density and velocity field as:

$$\delta^s(\mathbf{r},t) = \delta(\mathbf{r},t) - \hat{\mathbf{z}}.\nabla\hat{\mathbf{z}}.\mathbf{v}_b(\mathbf{r},t). \tag{15}$$

Here $\hat{\mathbf{z}}$ is taken to be the common line of sight to all the objects. In Fourier space equation (15) can be written as:

$$\delta^s(\mathbf{k},t) = \delta(\mathbf{k},t) + ik_z v_z(\mathbf{k},t). \tag{16}$$

Here $k_z = \hat{\mathbf{z}}.\mathbf{k}$ and $v_z = \hat{\mathbf{z}}.\mathbf{v_b}$. The velocity field in the case of tangled magnetic fields has both a divergence and a curl component.

$$\mathbf{v_b} = \mathbf{v_d} + \mathbf{v_c}. \tag{17}$$

Here $\mathbf{v_d}$ and $\mathbf{v_c}$ are the divergence and curl part of the velocity field. Their time evolution is already discussed in the last section. In Fourier space the divergence component points in the direction of the **k** vector, therefore it is convenient to decompose the velocity field parallel and perpendicular to the **k** vector, this gives the velocity field in the Fourier space as:

$$\mathbf{v_d}(\mathbf{k}) = \hat{\mathbf{k}}\hat{\mathbf{k}}.\mathbf{v}(\mathbf{k}), \tag{18}$$

$$\mathbf{v_c}(\mathbf{k}) = \mathbf{v}(\mathbf{k}) - \hat{\mathbf{k}}\hat{\mathbf{k}}.\mathbf{v}(\mathbf{k}), \tag{19}$$

$\mathbf{v_d}$ can readily be solved in terms of the density field using the continuity equation (equation 2):

$$\hat{\mathbf{z}}.\mathbf{v}_{\mathrm{d}}(\mathbf{k}) \equiv v_{dz} = -\frac{i\mu}{k}\delta(\mathbf{k})g_1(t). \tag{20}$$

Here $\mu = k_z/k$ is the angle between the Fourier mode and the line of sight and $g_1(t)$ is the time dependence of the divergence part of the velocity field; it is shown in Fig. 1. Note that we use the same symbols for density and velocity fields in both real and Fourier space. The curl part of the velocity field in the Fourier space is projected out by multiplying the Euler equation (equation 1) by $\delta_{ij} - \hat{\mathbf{k}}_i\hat{\mathbf{k}}_j$, δ_{ij} being the Kronecker delta function. The time dependence of the curl mode $g_2(t)$ is given in equation (13) and shown in Fig. 1.

From equation (14) the redshift space power spectrum can be written as:

$$(2\pi)^3 P_s(\mathbf{k}, t)\delta_D^3(\mathbf{k}+\mathbf{k}') = \langle(\delta(\mathbf{k}, t) + ik_z v_z(\mathbf{k}, t))(\delta(\mathbf{k}', t) + ik'_z v_z(\mathbf{k}', t))\rangle. \quad (21)$$

This can be expanded as:

$$\begin{aligned} P_s(\mathbf{k}, t) = {} & P(k) f^2(t) - g_1(t)k_z^2\langle v_{dz}(\mathbf{k})v_{dz}(-\mathbf{k})\rangle + ig_1(t)f(t)k_z\langle\delta(\mathbf{k})v_{dz}(-\mathbf{k})\rangle \\ & + ig_1(t)f(t)k_z\langle\delta(-\mathbf{k})v_{dz}(\mathbf{k})\rangle - ig_2(t)f(t)k_z\langle\delta(\mathbf{k})v_{cz}(-\mathbf{k})\rangle \\ & + ig_2(t)f(t)k_z\langle\delta(-\mathbf{k})v_{cz}(\mathbf{k})\rangle + g_2^2(t)k_z^2\langle v_{cz}(\mathbf{k})v_{cz}(-\mathbf{k})\rangle \\ & + k_z^2 g_1(t)g_2(t)\langle v_{dz}(\mathbf{k})v_{cz}(-\mathbf{k})\rangle - k_z^2 g_1(t)g_2(t)\langle v_{dz}(-\mathbf{k})v_{cz}(\mathbf{k})\rangle. \quad (22) \end{aligned}$$

Here $P(k) = \langle\delta(\mathbf{k})\delta(-\mathbf{k})\rangle$ is the real space power spectrum. It is derived in Appendix A. $f(t)$ gives the evolution of density perturbations (equation (11) and Fig. 1). The correlations involving the divergence part of the velocity fields can be readily written using the continuity equation (equation 2):

$$\begin{aligned} \langle\delta(-\mathbf{k})v_{dz}(\mathbf{k})\rangle &= -i\frac{k_z}{k^2}P(k), \\ \langle v_{dz}(\mathbf{k})v_{dz}(-\mathbf{k})\rangle &= -\frac{k_z^2}{k^4}P(k). \end{aligned} \quad (23)$$

Equation (23) along with the first four terms of equation (22) give the usual formula of redshift-distortion first derived by Kaiser (1987): $P_s(\mathbf{k}) = (1+\mu^2\beta)^2 P(k)$, where $\beta = g_1(t_0)/f(t_0) \simeq \Omega_m^{0.6}$ (Lahav *et al.* 1991). Analysis of 2dF data suggests that $\beta \simeq 0.4$ (Peacock *et al.* 2001). Tangled magnetic fields also generate curl modes, which give rise to additional terms in the power spectrum in redshift space. We show in Appendix A that:

$$\begin{aligned} \langle\delta(-\mathbf{k})v_{cz}(\mathbf{k})\rangle &= 0, \\ \langle v_{dz}(\mathbf{k})v_{cz}(-\mathbf{k})\rangle &= 0. \end{aligned} \quad (24)$$

The non-trivial contribution comes from the term: $\langle v_{cz}(\mathbf{k})v_{cz}(-\mathbf{k})\rangle$. This can be written as:

$$\langle v_{cz}(\mathbf{k})v_{cz}(-\mathbf{k})\rangle = \langle v_z(-\mathbf{k})v_z(\mathbf{k})\rangle - \frac{k_z^2}{k^4}P(k) + i\frac{k_z}{k^2}\langle v_z(\mathbf{k})\delta(-\mathbf{k})\rangle - i\frac{k_z}{k^2}\langle v_z(-\mathbf{k})\delta(\mathbf{k})\rangle. \quad (25)$$

In Appendix A we show that, $\langle v_z(\mathbf{k})\delta(-\mathbf{k})\rangle = -ik_z/k^2 P(k)$. This simplifies the equation to:

$$\langle v_{cz}(\mathbf{k})v_{cz}(-\mathbf{k})\rangle = \langle v_z(-\mathbf{k})v_z(\mathbf{k})\rangle + 3\frac{k_z^2}{k^4}P(k). \tag{26}$$

The term $\langle v_z(-\mathbf{k})v_z(\mathbf{k})\rangle$ cannot be written in terms of $P(k)$. As shown in Appendix A, it contributes two positive terms proportional to μ^2 (quadrupole) and μ^4 (hexadecapole) with magnitude comparable to $P(k)$ (equation 43). This information along with equation (26) allows us to assess the contribution of the curl component of the velocity field to the redshift space distortion. Its contribution at the present epoch is proportional to $g_2^2(t_0)$. If the magnetic fields originated in the very early universe then the contribution of the curl component of the velocity field is negligible as it doesn't have any growing mode. From Fig. 1, we can see that $g_2(t_0)/g_1(t_0) \ll 1$. However if the magnetic fields have their origin in the recent history of the universe then it is possible to have $g_2(t_0) \simeq g_1(t_0)$. In this case the curl component enhances the contribution in both μ^2 and μ^4 terms. It is interesting to note that unlike the divergence term in which the μ^4 term is smaller than the μ^2 term by a factor of $\beta/2$, the curl contribution is dominated by the μ^4 term. In many models we studied it can be nearly 5 times the μ^2 term. The presence of the curl component leads to the intriguing possibility that the observed redshift space distortion is dominated by the curl mode. In that case it is not possible to infer the value of β from this observation as is usually done (Hamilton *et al.* 2001; Peacock 1998). We illustrate this case in Fig. 2. More realistically however the effect of the curl term might be determined from simultaneously determining the contributions from both the μ^2 and μ^4 terms. It has not so far been possible from observations which have determined only the μ^2 part (Peacock *et al.* 2001). On-going survey SDSS galaxy survey has the potential to test this hypothesis. These redshift space effects are nearly independent of the power spectrum of the tangled magnetic field. We discuss below whether it is possible to construct viable models of density power spectrum from the tangled magnetic field.

For our calculations we take the magnetic field power spectrum to be power law:

$$B^2(k) = Ak^n. \tag{27}$$

We consider the range of k between $k_{\min}$, which is taken to be zero unless specified otherwise, and the approximate scale at which the Alfv́en waves damp in the pre-recombination era (Jedamzik, Katalinic & Olinto 1998; Subramanian & Barrow 1998). Following Jedamzik *et al.* (1998), $k_{\max} \simeq 60\,\mathrm{Mpc}^{-1}(B_0/(3\times10^{-9}\,\mathrm{G})$. B_0, the RMS of magnetic field fluctuations at the present epoch, is defined as:

$$B_0^2 \equiv \langle B_i(\mathbf{x},t_0)B_i(\mathbf{x},t_0)\rangle = \frac{1}{\pi^2}\int_0^{k_c} dkk^2B^2(k). \tag{28}$$

Here $k_c = 1\,h\,\mathrm{Mpc}^{-1}$ (Subramanian & Barrow 2002). This gives:

$$A = \frac{\pi^2(3+n)}{k_c^{(3+n)}}B_0^2. \tag{29}$$

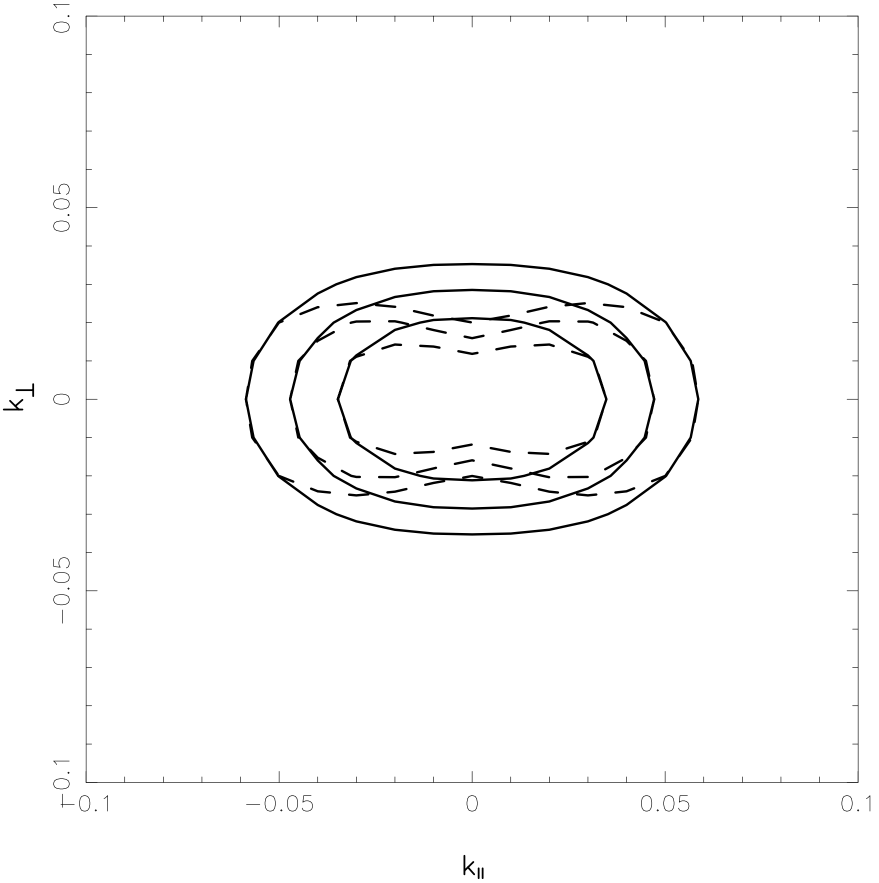

Figure 2. Equal redshift space power spectrum contours are shown. The x- and y-axis correspond to the component of k vector parallel and perpendicular to the line of sight. The solid contours show the contours for $\beta = 0.4$, to match with observations (Peacock *et al.* 2001), with zero curl contribution. The dashed curves correspond to $\beta = 0$ with curl component normalized to give the same quadrupole as in the previous case. Note strong distortions of the curves from the dominant hexadecapole in this case. The contour levels and overall normalization is arbitrary.

3.1 *Power spectrum in real space*

In the previous subsection, we discussed the redshift space effects in the observed power spectrum. Such effects are nearly independent of the power spectrum of the tangled magnetic field. In this section we study the possibility of constructing viable models of density power spectrum from tangled magnetic fields.

It is conceivable that tangled magnetic fields originated in the very early universe during inflationary epoch (Turner & Widrow 1988; Ratra 1992). In this case tangled magnetic fields can have large coherence lengths, or $k_{\rm min} \simeq 0$ in equation (27). On the other hand magnetic fields could be of more recent origin ($z \lesssim 10$). However, recent astrophysical processes do not generate large scale magnetic fields. Quasar outflows (see e.g., Furlanetto & Loeb 2001) might pollute the intergalactic medium sufficiently for it to have magnetic fields with maximum coherence scales $\simeq 2\,$Mpc with magnitudes $\simeq 10^{-9}\,$G. In both cases magnetic fields can have appreciable effect on the large scale structure in the universe at linear scales. We discuss both these possibilities below.

3.1.1 *Early universe magnetic fields*

Kim, Olinto & Rosner (1996) calculated the density power spectrum in the presence of tangled magnetic fields. They concluded that for magnetic field power spectrum index $4 < n < -1$, the density power spectrum scales as k^4. We confirm their result but also consider smaller values of n. The observed power spectrum (Spergel *et al.* 2003) is consistent with $P(k) \propto k$ at large scales ($k \lesssim 0.002$); at smaller scales $P(k)$ turns around and scales as k^p with p changing from 0 to -3 as the scales become smaller (see e.g., Efstathiou *et al.* 1996; Percival *et al.* 2001; Fig. 3). This clearly means that none of the magnetic field power spectrum index n studied by Kim *et al.* (1996) can explain the data, which they also pointed out. To make atleast the slope of $P(k)$ agree with the large scale structure data, one needs to consider smaller value of n. For $n = -2$, $P(k) \propto k^3$, for $n \lesssim -2.5$, the power spectrum turns even shallower. An analytical understanding of this behaviour is given in Appendix A (equation 37). We consider $n = -2.9$, also studied by Subramanian & Barrow (2002); for this value $P(k)$ scales approximately as k. This suggests that the parameter range of interest lies around this value. As we

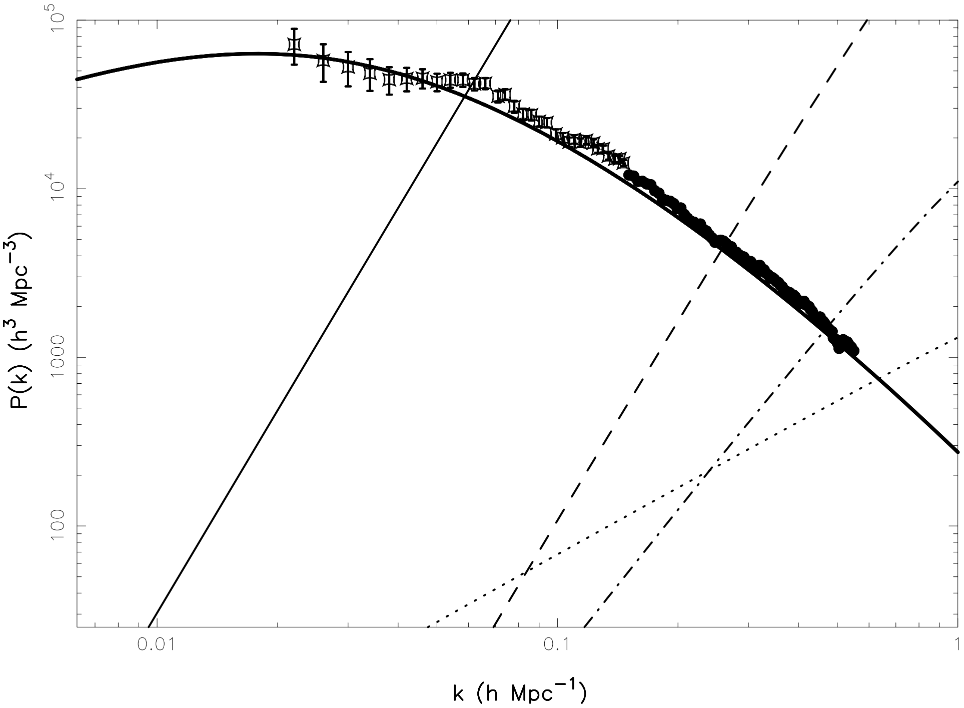

Figure 3. The density power spectrum from tangled magnetic fields is shown along with recent observation of the power spectrum from 2dF galaxy survey (Percival *et al.* 2001) and a variant of CDM model. For all the curves $B_0 = 3 \times 10^{-9}$ G. The curves correspond to different values of n: $n = 0$ (solid line), $n = -1$ (dashed line), $n = -2$ (dot-dashed line), and $n = -2.9$ (dotted line). The thick solid line corresponds to CDM model for a spatially flat universe: $\Omega_m = 0.3$, $\Omega_\Lambda = 0.7$, $\Omega_b = 0.04$.

discussed above that redshift space effects do not change this conclusion. Subramanian & Barrow (2002) showed that this model can lead to CMBR anisotropies $\simeq 10\,\mu$k for angular scales $1000 < \ell < 2000$ for $B_0 = 3 \times 10^{-9}$, G, which is comparable to the observed anisotropies at these scales (Mason *et al.* 2002). We check if this model, with this normalization, can give reasonable effect on the large scale structure at the present epoch. We plot in Fig. 3 the density power spectra for several values of n. The power spectrum for this model is nearly two orders of magnitude below the observed power spectrum at linear scales. Therefore, even though this model leads to the correct shape of power spectrum at large scales, the normalization needed to give the correct CMBR anisotropy level is too low. We should point out that this result is nearly independent of the upper cut-off $k_{\max}$ of the magnetic field power spectrum. Fig. 3 also shows that spectral indices $n \gtrsim -1$ are ruled out by the present data for $B_0 = 3\times 10^{-9}$ G. However the results for models with $n \gtrsim -1.5$ are strongly dependent on $k_{\max}$ and therefore less reliable and they are also likely to give unacceptably large CMBR anisotropies. Therefore we are led to conclude that if tangled magnetic fields existed at the last scattering surface, they are unlikely to have much impact on the large scale structure in the universe at present at linear scales. It should however be noted from Figure 3 that magnetic fields can have significant effect on the non-linear scales; which in particular will lead to early collapse of structures. This may have important implications for the re-ionization of the universe (Sethi & Subramanian 2003). We do not discuss this scenario in detail in this paper.

3.1.2 *Low redshift magnetic fields*

We consider a simple model to assess the effect of low redshift magnetic fields on the large scale structure. We assume these fields were created in the post-reionization epoch $z \lesssim 15$ (Spergel *et al.* 2003) and $k_{\min} = 6\text{h Mpc}^{-1}$ and $k_{\max} = 30\text{h Mpc}^{-1}$, this corresponds roughly to scales between $1\,\text{h}^{-1}$Mpc and $200\,\text{h}^{-1}$kpc. The slope of the magnetic field power spectrum and its strength is to be determined by observations. While our choice of $k_{\min}$ is motivated by the requirement that astrophysical processes are unlikely to generate larger scale magnetic fields, our choice of $k_{\max}$ is largely arbitrary. Our interest is in studying the effect of these fields at scales that are linear at present, i.e., $k \lesssim 0.2$ Mpc. We show in Appendix A (equation (38) that models in which $k \ll k_{\min}$ generically give density power spectrum $\propto k^4$, irrespective of the slope of the tangled magnetic field power spectrum n. For $n \gtrsim -1.5$, the density power spectrum is dominated by the upper cut-off $k_{\max}$; in the other limit $k_{\min}$ determines the amplitude of the power spectrum. In Fig. 4, we show the power spectrum for two values of n for $B_0 = 10^{-9}$ G. For simplicity we take $f(t_0) = 5$. It is seen that if $n \gtrsim 1$ the density power spectrum at linear scales can get appreciable contribution from tangled magnetic fields. However results for these spectral indices depend strongly on the upper cut-off $k_{\max}$ and therefore are less reliable. Note that the value of B_0 needed to cause sufficient effect on the large scale structure is quite different from Sethi (2003). This is owing to the fact that $k_{\max}$ was taken to be $1\,\text{h Mpc}^{-1}$ in that work and fields were assumed to be locally generated, i.e., $f(t_0) = 1$.

A possible criticism of our analysis is the use of linear theory and neglect of the RHS of equation (4). Even though we are interested in density perturbations at linear scales at present, presence of the RHS of equation (4) mixes all modes of tangled magnetic fields and the velocity perturbations and in general cannot be neglected. Our preliminary

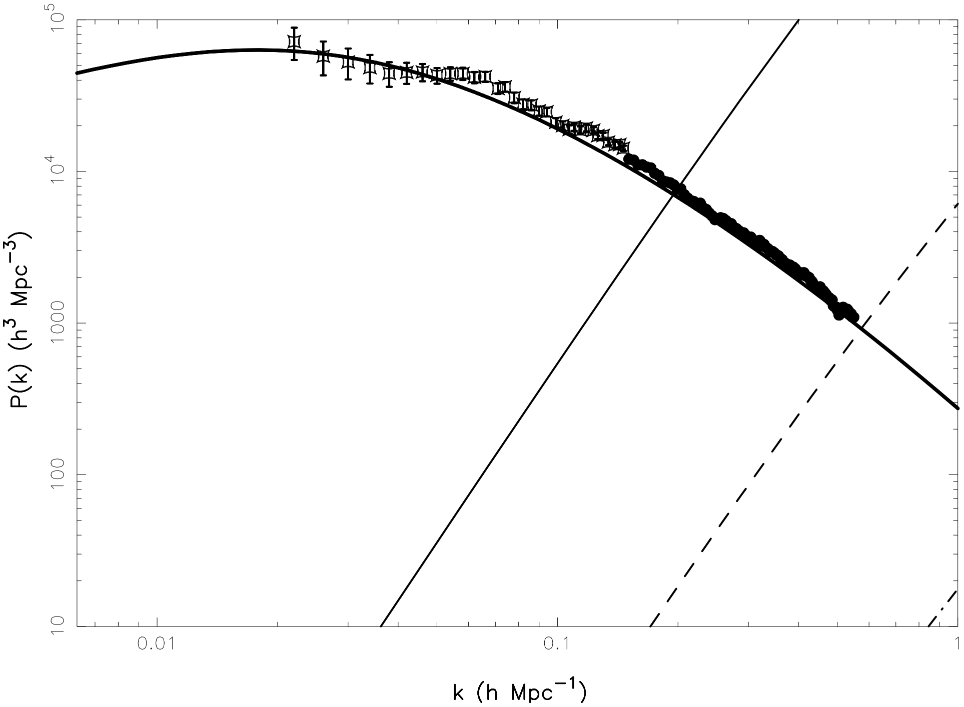

Figure 4. Same as Figure 3 for the model in which the tangled magnetic fields originate at $z \lesssim 10$ (see text for detail). $B_0 = 10^{-9}$ G and the curves correspond to different spectral index values: $n = 2$ (Solid line), $n = 1$ (dashed line).

calculations show that these terms are of order k times the velocity and magnetic field, which means that back reaction of velocity perturbations on the magnetic fields is of higher order than the density power spectrum and could be dropped for studying linear scales. We plan to study this issue in more detail in future. In particular these terms can be neglected if the density perturbation $\delta(\mathbf{k})$ is negligible for all scales in question. The smallest scale at which perturbations can collapse is the magnetic Jeans length $\simeq 100\,\text{kpc}(B_0/(10^{-9}\,\text{G}))$ (Subramanian & Barrow 1998). In practice it is however seen that neglect of non-linear terms to study perturbations at linear scales holds for a wide range of linear scales. For example the use of linear theory in the usual CDM model gives reasonable results for studying perturbations for $k \lesssim 0.2\,\text{h}^{-1}$Mpc which are quasi-linear at present, even though smaller structures could have collapsed at much higher redshifts. One case in which we are justified in neglecting the non-linear terms is when the final result can be shown to be nearly independent of the contribution of large k modes of the magnetic field. This as we discussed above is valid for $n \lesssim -1.5$ if the magnetic fields are generated in the early universe. In other cases neglect of this term should depend on both B_0 and n. Therefore our results on the effect of magnetic fields generated at low redshifts should be considered preliminary.

4. Conclusions

In this paper we studied the effect of tangled magnetic fields on the large scale structure in the universe. We calculated the power spectrum of the tangled magnetic fields and compared it with the observations at the present epoch. Our results can be summarized as:

- If the magnetic field originated in the very early universe. It is possible to construct models in which the shape of density power spectrum $\propto k$, i.e., it agrees with the observed power spectrum shape for $k \lesssim 0.02\,\mathrm{h}^{-1}\,\mathrm{Mpc}^{-1}$. However compatibility with observed CMBR anisotropies suggests that the density power spectrum from tangled magnetic field is smaller than the observed power spectrum by atleast two orders of magnitudes at linear scales ($k \lesssim 0.2\ \mathrm{h}^{-1}\,\mathrm{Mpc}^{-1}$) at present. Therefore very early universe tangled magnetic fields are unlikely to have important impact on the structures in the present universe.
- We consider a simple model in which the magnetic fields were generated with coherence scales $k \gtrsim 2\,\mathrm{h}^{-1}\,\mathrm{Mpc}^{-1}$ in the post-reionization epoch $z \lesssim 10$. In all such models the density power spectrum $\propto k^4$, i.e., the shape of the power spectrum is incompatible with the shape of the observed shape. It is possible to construct models in which the magnetic field can have important contribution to the density power spectrum for $B_0 \simeq 10^{-9}\,\mathrm{G}$. (It should be noted that the density power spectrum from initial conditions which could have originated during inflation adds to the magnetic field-induced density power spectrum as the density fields generated by these two processes are uncorrelated; see equation (11) and the discussion following it.) However these results are quite sensitive to the shape and the upper k cut-off of the tangled magnetic fields power spectrum, which are difficult to fix from either observations or theory.
- The redshift space effects from tangled magnetic fields have additional features owing to curl component of velocities generated by these fields. The curl component increases both the quadrupole (μ^2 term), hexadecapole (μ^4 term) of the redshift space power spectrum. For very early universe magnetic fields the curl component decays so it cannot have important contribution to the redshift space effects. For magnetic fields generated in the more recent epoch, the curl component of the velocity field can be comparable to the divergence component. In this case both quadropole and hexadecapole can be dominated by the curl component as opposed to the usual case of divergence collapse. This leads to the interesting possibility that most of the redshift space effects come from the curl component, and the usual way of determining Ω_m from the redshift space distortion is not entirely valid (Peacock *et al.* 2001). As noted above the density power spectrum from tangled magnetic fields can dominate the observed power spectrum for $B_0 \simeq 10^{-9}\,\mathrm{G}$, and hence can be used to probe tangled fields which are too small to be detected by other methods (see e.g., Sethi 2003)

In summary: Tangled magnetic fields are unlikely to have provided the initial conditions for the formation of presently-observed structure in the universe. In this paper we showed that this conclusion seems inevitable for magnetic fields generated in the very early universe. However we could only study a simple model of tangled magnetic fields which were generated at $z \lesssim 10$. It would be interesting to do a more detailed analysis of this scenario taking into account the non-linear effects.

Acknowledgements

One of us (SKS) would like to thank Kandaswamy Subramanian for many useful discussions, suggestions, and comments on the manuscript.

APPENDIX A

In this Appendix, we derive expressions for $P(k)$, $\langle \delta(\mathbf{k}) v_z(\mathbf{k}) \rangle$, $\langle (v_z(\mathbf{k}))^2 \rangle$ and also make an approximate analytical estimate of the small k-dependence of $P(k)$. The real space spatial density contrast and peculiar velocity component along the line of sight are given as:

$$\delta(\mathbf{x}) = \nabla \cdot [\mathbf{B} \times (\nabla \times \mathbf{B})],$$
$$\mathbf{v}(\mathbf{x}) \cdot \hat{\mathbf{z}} = [\mathbf{B} \times (\nabla \times \mathbf{B})] \cdot \hat{\mathbf{z}}. \tag{30}$$

Here $B \equiv B(\mathbf{x}, t_0)$, i.e., the value of magnetic field at the present epoch. The Fourier space expressions for the above fields are:

$$\delta(\mathbf{k}) = \int d^3k_1 [(\mathbf{k_1} \cdot \mathbf{B}(\mathbf{k} - \mathbf{k}_1))\ (\mathbf{k} \cdot \mathbf{B}(\mathbf{k}_1)) - (\mathbf{k_1} \cdot \mathbf{k})\ (\mathbf{B}(\mathbf{k_1}) \cdot \mathbf{B}(\mathbf{k} - \mathbf{k_1}))], \tag{31}$$

$$\mathbf{v}(\mathbf{k}) = -i \int d^3k_1 [(\mathbf{B}(\mathbf{k_1}) \cdot \mathbf{B}(\mathbf{k} - \mathbf{k_1}))\mathbf{k_1} - (\mathbf{k_1} \cdot \mathbf{B}(\mathbf{k} - \mathbf{k_1}))\mathbf{B}(\mathbf{k_1})]. \tag{32}$$

The volume element in the integrals can be simplified by choosing $\mathbf{k}$ to lie along the z-axis and $\hat{n}$ to lie in the x-z plane. We thus have,

$$\int d^3k_1 = \int dk_1 k_1^2 \int d\mu \int d\phi. \tag{33}$$

Here, $\mu \equiv \cos\ \theta$ (θ is the angle between k_1 and the z-axis) while ϕ is the azimuthal angle. In the integral, k_1 ranges from $k_{\rm min}$ to $k_{\rm max}$, μ from -1 to $+1$ and ϕ from 0 to 2π. Care has to be taken while evaluating multiple integrals formed from above (for e.g., $\langle \delta^2 \rangle$) since the presence of terms like $\delta(k_2 + k - k_1)$ after integrating over k_2 puts a constraint on the integration range of θ as well. Taking all this into account we can split the integration ranges for the cases of interest in this paper as follows:

For $k_{\rm min} = 0$ and $0 < k_1 < k_{\rm max}$,

$$\int d^3k_1 = \int_0^k dk_1 \int_{-1}^{+1} d\mu + \int_k^{k_{max}-k} dk_1 \int_{-1}^{+1} d\mu + \int_{k_{max}-k}^{k_{max}} dk_1 \int_{\mu_{max}}^{1} d\mu. \tag{34}$$

For $k_{\rm min} \neq 0$ and $0 < k_1 < k_{\rm min}$,

$$\int d^3k_1 = \int_{k_{\rm min}}^{k+k_{\rm min}} dk_1 \int_{-1}^{\mu_{\rm min}} d\mu + \int_{k+k_{\rm min}}^{k_{\rm max}-k} dk_1 \int_{-1}^{+1} d\mu + \int_{k_{\rm max}-k}^{k_{\rm max}} dk_1 \int_{\mu_{\rm max}}^{1} d\mu, \tag{35}$$

where $\mu_{\rm max} = (k^2 + k_1^2 - k_{\rm max}^2)/(2kk_1)$ and $\mu_{\rm min} = (k^2 + k_1^2 - k_{\rm min}^2)/(2kk_1)$.

To calculate $P(k)$ we take the ensemble average of $[\delta(\mathbf{k})]^2$. This product contains terms involving four point functions of $\mathbf{B}$. By assuming that $\mathbf{B}$ is Gaussian distributed in the ensembles such terms can be written as sums of products of two-point functions of **B**. Finally using equation (8) and simplifying, we arrive at the following expression for $P(k)$:

$$P(k)=\int_{k_{\rm min}}^{k_{\rm max}} dk_1 \int_{-1}^{+1} d\mu \frac{B^2(k_1)B^2(|\mathbf{k}-\mathbf{k_1}|)}{|\mathbf{k}-\mathbf{k_1}|^2}\,[2k^5k_1^3\mu + k^4k_1^4(1-5\mu^2) + 2k^3k_1^5\mu^3]. \tag{36}$$

We evaluate this double integral numerically. However we can analytically see the form for $P(k)$ when $k \ll k_{\rm max}$ both for $k_{\rm min} = 0$ as well as $k_{\rm min} \neq 0$ as follows:

For $k_{\rm min} = 0$ and $k \ll k_{\rm max}$, the relevant case when the magnetic fields originate in the early universe, the only major contribution to the $P(k)$ comes from the second integral in equation (34). We thus have to lowest order in $k/k_{\rm max}$,

$$P(k) \sim Ak^{2n+7} + Bk_{\rm max}^{2n+3}k^4 + Ck_{\rm max}^{2n+1}k^6 + \ldots(\text{higher powers of } k) \tag{37}$$

where, A, B and C are coefficients depending only on n. We thus see that for $n > -1.5$ the leading order term is proportional to k^4 whereas for $n < -1.5$ it is proportional to k^{2n+7}. In particular for $n = -2$, the dependence goes as k^3. Also, $P(k) \to k^1$ as $n \to -3$.

For $k_{\rm min} \neq 0$ and $k \ll k_{\rm min}$, the case if the magnetic fields are of more recent origin, the leading contribution to $P(k)$ comes from the third integral in equation (35). Thus, to lowest order in k we get,

$$P(k) \sim Ak^4(k_{\rm max}^{2n+3} - k_{\rm min}^{2n+3}) + \ldots(\text{higher powers of } k). \tag{38}$$

Thus, we see that with an infrared cutoff which is much larger than the wavenumber of interest, the dependence of $P(k)$ is generically k^4. The dependence on $k_{\rm max}$ and $k_{\rm min}$ is such that for $n > -1.5$, the value of $P(k)$ is determined by and increases with $k_{\rm max}$. In the other limit $P(k)$ is determined by $k_{\rm min}$. We now evaluate the correlation $\langle\delta(k)\ \mathbf{v}\cdot\hat{\mathbf{z}}\rangle$ We can show that it is simply proportional to $P(k)$ in the following way: From the assumptions of homogeneity and isotropy, we can write

$$\langle v_i(\mathbf{k})v_j(\mathbf{q})\rangle = \big(A(k^2)\ \delta_{ij} + B(k^2)\ k_ik_j\big)\ \delta^3(\mathbf{q}-\mathbf{k}) \tag{39}$$

where $A(k^2)$ and $B(k^2)$ are some as yet undetermined coefficients. Thus, using the continuity equation (equation 2):

$$\langle\delta(\mathbf{k})\ \mathbf{v}(\mathbf{k})\cdot\hat{\mathbf{n}}\rangle = -i\langle k_iv_iv_jn_j\rangle = -i\mathbf{k}\cdot\hat{\mathbf{n}}[A(k^2) + k^2B(k^2)]. \tag{40}$$

Similarly we get,

$$P(k) \equiv -\langle k_iv_ik_jv_j\rangle = -k^2[A(k^2) + k^2B(k^2)]. \tag{41}$$

Thus from these equations we get the following relation:

$$\langle \delta(\mathbf{k})\, \mathbf{v}(\mathbf{k}) \cdot \hat{\mathbf{n}} \rangle = i \frac{\mathbf{k} \cdot \hat{\mathbf{n}}}{k^2}\, P(k). \tag{42}$$

From this derivation equation (24) follows. Finally, this allows us to write $\langle (\mathbf{v}(\mathbf{k}) \cdot \hat{\mathbf{n}})^2 \rangle$ correlation:

$$\langle (\mathbf{v}(\mathbf{k}) \cdot \hat{\mathbf{n}})^2 \rangle = \int_{k_{\min}}^{k_{\max}} dq \int_{-1}^{+1} d\mu \frac{B^2(q) B^2(|\mathbf{k}-\mathbf{q}|)}{|\mathbf{k}-\mathbf{q}|^2} \Big[\cos^2\alpha \left(2k^3q^3\mu - 5k^2q^4\mu^2 + k^2q^4 - q^5k(\mu - 3\mu^3)\right) + q^5k(\mu - \mu^3)\Big]. \tag{43}$$

Here, α is the angle between $\mathbf{k}$ and $\hat{n}$.

References

Barrow, J. D., Ferreira, P. G., Silk, J. 1997, *Physical Review Letters*, **78**, 3610.
Blasi, P., Burles, S., Olinto, A. V. 1999, *ApJL*, **514**, L79
Colless, M. et al. 2001, *MNRAS*, **328**, 1039.
Efstathiou, G., in Schaeffer, R., Silk, J., Spiro, M., & Zinn-Justin, J. 1996, *ASP Conf. Ser.* 24: Cosmology and Large-scale Structure in the Universe
Freedman, W. L. *et al.* 2001, *ApJ*, **553**, 47.
Furlanetto, S. R., Loeb, A. 2001, *ApJ*, **556**, 619.
Hamilton, A. J. S. 1998, *ASSL* Vol. 231: *The Evolving Universe*, 185.
Hawkins, E. *et al.* 2002, astro-ph/0212375.
Jedamzik, K., Katalinić, V., Olinto, A. V. 2000, *Physical Review Letters*, **85**, 4, July 24, 2000, pp.700–703
Jedamzik, K., Katalinić, V., Olinto, A. V. 1998, *PRD*, **57**, 3264.
Kaiser, N. 1987, *MNRAS*, **227**, 1.
Kim, E., Olinto, A. V., Rosner, R. 1996, *ApJ*, **468**, 28.
Kim, K.-T., Kronberg, P. P., Giovannini, G., Venturi, T. 1989, *Nature*, **341**, 720.
Kosowsky, A., Loeb, A. 1996, *ApJ*, **469**, 1.
Kronberg, P. P. 1994, *Reports on Progress in Physics*, **57**, 325.
Kronberg, P. P., Simard-Normandin, M. 1976, *Nature*, **263**, 653.
Lahav, O. *et al.* 2002, *MNRAS*, **333**, 961.
Lahav, O., Rees, M. J., Lilje, P. B., Primack, J. R. 1991, *MNRAS*, **251**, 128.
Landau, L. D., Lifshitz, E. M. 1987, *Fluid Mechanics*, (Pergamon Press.)
Mason, B. S. *et al.* 2002, astro-ph/0205384.
Parker, E. N. 1979, Cosmical Magnetic Field: Their Origin and Their Activity, (Oxford University Press).
Peebles, P. J. E. 1980, *Large Scale Structure of the Universe*, (Princeton University Press).
Peacock, J. A. *et al.* 2001, *Nature*, **410**, 169.
Perlmutter, S. *et al.* 1999, *ApJ*, **517**, 565.
Percival, W. J. *et al.* 2001, *MNRAS*, **327**, 1297.
Ratra, B. 1992, *ApJL*, **391**, L1.
Rees, M. J., Reinhardt, M. 1972, *A & A*, **19**, 189.
Riess, A. G. *et al.* 1998, *AJ*, **116**, 1009.
Ruzmaikin, A. A., Sokolov, D. D., Shukurov, A. M. 1988, Moscow, Izdatel'stvo Nauka, 1988, 280 p.
Sethi, S. K. 2003, *MNRAS*, **342**, 962.
Spergel, D. N, *et al.* 2003, astro-ph/0302209.
Subramanian, K., Barrow, J. D. 2002, *MNRAS*, **335**, L57.

Sethi, S. K., Subramanian, K. 2003, in preparation
Subramanian, K., Barrow, J. D. 1998, *Physical Review Letters*, **81**, 3575.
Subramanian, K., Barrow, J. D. 1998, *PRD*, **58**, 83502.
Turner, M. S., Widrow, L. M. 1988, *PRD*, **37**, 2743.
Tytler, D., O'Meara, J. M., Suzuki, N., Lubin, D. 2000, *Physics Reports*, **333**, 409.
Vallée, J. P. 1990, *ApJ*, **360**, 1.
Wasserman, I. 1978, *ApJ*, **224**, 337.
Widrow, L. M. 2002, *Reviews of Modern Physics*, **74**, 775.
York, D. G. *et al.* 2000, *AJ*, **120**, 1579.
Zeldovich, I. B., Ruzmaikin, A. A., Sokolov, D. D. 1983, *The Fluid Mechanics of Astrophysics and Geophysics*. Volume 3, (New York: Gordon and Breach Science Publishers), 381 p.

J. Astrophys. Astr. (2003) **24,** 69–83

Studies of Clump Structure of Photodissociation Regions at Millimeter and Sub-millimeter Wavelengths

Abdul Qaiyum & Syed Salman Ali *Department of Physics, Aligarh Muslim University, Aligarh 202 002, India.*

Received 2002 December 21; accepted 2003 July 5

Abstract. To interpret the millimeter and sub-millimeter line emissions of atomic and molecular species from galactic and extragalactic photodissociation regions, warm gas components and molecular clouds, generally, escape probability formalism of Tielens & Hollenbach (herein referred as TH) are employed which is based on the assumption of plane parallel geometry of infinite slab allowing photons to escape only from the front. Contrary to the assumption observationally it is found that these lines are optically thin except OI(63μm) and low rotational transitions of CO and some other molecules. This observational evidence led us to assume that emitting regions are finite parallel plane slab in which photons are allowed to escape from both the surfaces (back and front). Therefore, in the present study escape of radiations from both sides of the homogeneous and also clumpy PDR/molecular clouds are taken into consideration for calculating the line intensities at millimeter and sub-millimeter wavelengths (hereinafter referred as QA). Results are compared with that of the TH model. It is found that thermal and chemical structures of the regions are almost similar in both the formalisms. But line intensities are modified by differing factors. Particularly at low density and low kinetic temperature and also for optically thin lines line intensities calculated from TH and QA model differ substantially. But at density higher than the critical density and also for optically thick lines TH and QA models converge to almost same values. An attempt has been made to study the physical conditions of the M17 region employing the present formalism.

Key words. Photodissociation region—clump structure—cooling lines —fine structure transitions and rotational transitions.

1. Introduction

During the last two decades theoretical attempts to interpret the observations from the photodissociation regions (PDRs), HII regions and reflection nebulae at millimeter and sub-millimeter wavelengths [CI (370 & 609 μm); OI (63 & 146 μm); CII (158 μm); SiII (35 μm); FeII (26 μm)]; and rotational lines of CO ($\Delta J = 1$ up to $J = 20$) have been made by Tielens & Hollenbach (1985 a,b); Stutzki *et al.* (1988); Wolfire *et al.* (1990); Castets *et al.* (1990); Tauber & Goldsmith (1990); Howe *et al.* (1991); Meixner *et al.* (1992); Meixner & Tielens (1993); Robert & Pagani (1993); Bennet *et al.* (1994);

Steiman-Cameron *et al.* (1997); Luhman *et al.* (1997); and Hermann *et al.* (1997); Kemper *et al.* (1999); Jackson & Kramer (1999) and Strorzer & Hollenbach (1999).

In theoretical studies of photodissociation regions, the model of Tielens & Hollenbach (1958a) (hereafter TH) has been extensively used to calculate the temperature and chemical structure (abundances of atomic, ionic and molecular species) of the region and also to calculate the line intensities of fine structure and rotational transitions of some of the atoms, ions and molecules, especially CO molecule. The PDR in the TH model is a homogeneous, semi-infinite, plane parallel slab illuminated on the non-infinite side by large flux of FUV ($6 < h\nu < 13.6$ ev) radiations (G_0 times more intense than the average interstellar radiation field 1.2×10^{-4} ergs s^{-1} cm^{-2} sr^{-1} of Habing 1968) and line emission takes place only towards the observer (semi-infinite assumption of deJong *et al.* (1980)). But now it has been established through the observations that most of the PDRs are clumpy in nature and some of the lines observed are also optically thin (i.e., line optical depth is less than unity). Therefore, homogeneous one-dimensional semi-infinite plane parallel geometry is no longer valid.

In the present study, PDR is supposed to be a finite plane parallel slab having clumps and inter-clumps mixed together. An attempt has been made to incorporate the escape of radiation from both sides of the region. To solve the radiative transfer in one-dimensional approach, the techniques of Averett & Hummer (1965) have been used. Further, the formalism of Boisse (1990) has been employed to compute the mean FUV radiation as a function of depth z, in two phase clumpy region. We apply them to solve radiation transfer through a region of high density, low filling material (clump) and low density, high filling factor (inter-clump). The nature of work is purely investigative, therefore, no attempt has presently been made to study the variety of PDRs. However, the present formalism has been employed to study the clumpy region of M17.

The mathematical formulation of the problem is discussed in section 2, physical parameters and assumptions presented in section 3 and results (hereinafter referred to as QA) and discussions are in section 4. The calculations are summarised in section 5.

2. Mathematical formulation of problem

The current interest in the problem of photodissociation regions, associated with the HII regions, requires methods to compute the following:

- Mean FUV intensity as a function of depth into the clumpy clouds to calculate the thermal and chemical structure of the region.
- Net radiation loss due to escape of radiation at millimeter and sub-millimeter wavelengths through the clumpy PDRs.

2.1 *FUV penetration through PDRs*

In the present study we use the formalism of Boisse (1990) to compute mean FUV intensity as a function of depth z, in a two phase clumpy region. We apply them to the case of UV radiative transfer through a region of high density, low filling factor material (the clump) and low density high filling factor (inter-clump). The derived solutions appear in pairs: one for the average intensity in the clump and other for average intensity in interclump phase.

According to Boisse (1990) the equation of radiative transfer for the case of isotropic scattering may be written as

$$\partial I(M,\theta,\varphi)/\partial S \; = -K(M)I(M,\theta,\varphi) + \omega K(M)J(M), \tag{2.1.1}$$

where $I(M,\theta,\varphi)$ is the specific intensity at a point M along a distance S defined by the angle θ and φ, $K(M)$ the extinction coefficient, ω the albedo of dust grains (K and ω being wavelength dependent) and $J(M)$ the mean intensity (average of I over θ and φ).

The average flux on a plane perpendicular to the incident photon as $\Psi^+(z)$ and $\Psi^-(z)$ in the forward and backward direction respectively are given by a pair of integrals with $(i, j = 0 \text{ or } 1)$ following Boisse (1990) as

$$\begin{aligned}\langle\Psi_i^+(z)\rangle = {}& \frac{2\pi\omega\, K_i}{K'' - K'}\int_0^z G_{ii}(z-z')\langle J_i(z')\rangle dz' \\ &+ \frac{2\pi\omega\, K_j}{K'' - K'}\int_0^z G_{ij}(z-z')\langle J_j(z')\rangle dz' + \langle\Psi_i^0(z)\rangle\end{aligned} \tag{2.1.2}$$

and

$$\begin{aligned}\langle\Psi_i^-(z)\rangle = {}& \frac{2\pi\omega\, K_i}{K'' - K'}\int_z^L G_{ii}(z'-z)\langle J_i(z')\rangle dz' \\ &+ \frac{2\pi\omega\, K_j}{K'' - K'}\int_z^L G_{ij}(z'-z)\langle J_j(z')\rangle dz \\ \langle\Psi^\pm(z)\rangle = {}& P_0\langle\Psi_0^\pm(z)\rangle + P_1\langle\Psi_0^\pm(z)\rangle.\end{aligned} \tag{2.1.3}$$

The subscripts 0 and 1 stand for clumpy and interclump. G_{ii} and G_{ij} are defined as $G_{ii} = G_{00}$ or G_{11} and $G_{ij} = G_{01}$ or G_{10} given as below:

$$G_{00}(x) = (\nu P_0 + K_1 - K')E_2(K' \mid x \mid) + (K'' - \nu P_0 - K_1)E_2(K'' \mid x \mid), \tag{2.1.4}$$

$$G_{01}(x) = (\nu P_1[E_2(K' \mid x \mid) - E_2(K'' \mid x \mid)], \tag{2.1.5}$$

$$G_{10}(x) = (\nu P_0[E_2(K' \mid x \mid) - E_2(K'' \mid x \mid)], \tag{2.1.6}$$

$$G_{11}(x) = (\nu P_1 + K_0 - K')E_2(K' \mid x \mid) + (K'' - \nu P_1 - K_0)E_2(K'' \mid x \mid). \tag{2.1.7}$$

The physical meaning of K'' is the transfer of radiation inside individual clump while K' describe the “clump to clump" transport. Its value is given by

$$\begin{aligned}K'^{('')} &= \frac{\nu + K_0 + K_1 - (+)\sqrt{(\nu + K_0 + K_1)^2 - 4K_0K_1 - 4\nu\langle K\rangle}}{2} \\ \langle K\rangle &= P_0K_0 + P_1K_1,\end{aligned} \tag{2.1.8}$$

where P is filling factor.

The average intensity of photons in the clump and interclump is simply given by

$$\begin{aligned}\langle J_i(z)\rangle = {}& \frac{\omega\, K_i}{2(K'' - K')}\int_0^L F_{ii}(z-z')\langle J_i(z')\rangle \\ &+ \frac{\omega\, K_i}{2(K'' - K')}\int_0^L F_{ij}(z-z')\langle J_i(z')dz' + \langle J_i^0(z)\rangle.\end{aligned} \tag{2.1.9}$$

The pair of subscripts i and j has the same meaning as defined earlier.

F_{ii} and F_{ij} have similar expression as the G_{ii} and G_{ij} except that $E_2(x)$ is replaced by $E_1(x)$. $\langle \Psi_i^0 \rangle$ is the unscattered photons equal to $4\pi \langle J_i^0(z) \rangle$. The initial value is taken as $\langle J_i^0(z) \rangle$ defined by

$$\langle J_i^0(z)\rangle = \frac{J_{in}}{(K'' - K')}\left[(\nu + K_j - K')e^{-k'z} + (K'' - \nu - K_j)e^{-k''z}\right], \qquad (2.1.10)$$

$$J_{in} = \frac{\Psi_{in}}{4\pi},$$

where Ψ_{in} is the incident flux; and pair (i and j) has the same meaning as defined earlier.

2.2 *Escape of radiation through PDRs*

The radiative transfer equation in a plane-parallel slab and isotropic source for distance z normal to the plane of stratification can be written as

$$\frac{\mu\, dI_\nu}{d\tau_\nu} \;=\; \Phi_\nu(x)[I_\nu(\tau_\nu, \mu) - S_\nu(\tau_\nu)], \qquad (2.2.1)$$

where

$$\tau_\nu \;=\; \int_z^\infty K_\nu(z)dz$$

and $\Phi_\nu(x)$ is a normalized profile function where x is a dimensionless variable measured with respect to the line center such that

$$\int_{-\infty}^{\infty} \Phi_\nu(x)\, dx \;=\; 1. \qquad (2.2.2)$$

Here

$$x = (\nu_s - \nu)/\Delta\nu_D$$

$$\Delta\nu_D \;=\; V_d\, \nu/c \quad \text{and} \quad V_d = (2KT + V_t^2)^{1/2},$$

ν is the frequency of the line observed $I_\nu(\tau_\nu, \mu)$ is the specific intensity of radiation for frequency ν at a point z in a direction of inclination $\theta(\mu = \cos\theta)$ to the normal and also depends on x but it is not shown as a function of x. The broadening of line is simply considered due to microturbulence (turbulence velocity V_t), which makes it convenient to work with in terms of Doppler width in the line profile. $S_\nu(\tau_\nu)$ is the local source function.

In case of an atmosphere with finite optical thickness t_ν equation reduces to

$$I_\nu^+(\tau_\nu, +\mu) = I_\nu^c(t_\nu, +\mu)e^{\frac{-(t_\nu - \tau_\nu)\Phi_\nu(x)}{\mu}} + \frac{\Phi_\nu(x)}{\mu}\int_{\tau_\nu}^{t_\nu} S_\nu(t)e^{\frac{-(t-\tau_\nu)\Phi_\nu(x)}{\mu}}dt, \qquad (2.2.3)$$

$$I_\nu^-(\tau_\nu, -\mu) = I_\nu^c(0, -\mu)e^{\frac{-(\tau_\nu)\Phi_\nu(x)}{\mu}} + \frac{\Phi_\nu(x)}{\mu}\int_0^{\tau_\nu} S_\nu(t)e^{\frac{-(\tau_\nu - t)\Phi_\nu}{\mu}}dt, \qquad (2.2.4)$$

$$\text{for } 0 \le \mu \le 1,$$

where I^+ and I^- symbolize the intensity towards observer and away from the observer $I_\nu^c(0, -\mu)$ and $I_\nu^c(t_\nu, \mu)$ are external source radiation at two faces of cloud (defined in terms of optical depth 0 as front face and t_ν as back face). Hereinafter these will be used as $I_\nu^c(o)$ and $I_\nu^c(t_\nu)$. The total radiation at any point inside the cloud at optical depth τ_ν after integrating over μ may be written as

$$\begin{aligned} I_\nu(\tau_\nu) = \frac{1}{2} I_\nu^c(0) E_2(\tau_\nu \Phi_\nu(x)) + \frac{1}{2} I_\nu^c(t_\nu) E_2((t_\nu - \tau_\nu)\Phi_\nu(x)) \\ + \frac{1}{2}\int_0^{\tau_\nu} S_\nu(t) E_1(\mid (\tau_\nu - t) \mid \Phi_\nu(x)) dt. \end{aligned} \tag{2.2.5}$$

The total intensity of a line at frequency ν averaged over the width can be written as

$$J_\nu(\tau_\nu) \; = \; \int_{-\infty}^{\infty} \Phi_\nu(x) I_\nu(\tau_\nu) \, dx, \tag{2.2.6}$$

here, $I_\nu(\tau_\nu)$ is a function of x also.

Finally after integration it comes out to be as

$$J_\nu \; = \; \frac{1}{2} I_\nu^c(0) \kappa_2(\tau_\nu) + \frac{1}{2} I_\nu^c(t_\nu) \kappa_2(t_\nu - \tau_\nu) + \int_0^{\tau_\nu} \kappa_1(\mid t - \tau_\nu \mid) S_\nu(t) dt, \tag{2.2.7}$$

where κ_1 and κ_2 in equation (2.2.7) are called the Kernel Function defined as

$$\kappa_1(\mid \tau_\nu - t \mid) = \frac{1}{2}\int_{-\infty}^{+\infty} \Phi_\nu^2(x) E_1(\Phi_\nu(x)(\mid t - \tau_\nu \mid)) \, dx, \tag{2.2.8}$$

$$\kappa_2(\tau_\nu) = \int_{-\infty}^{+\infty} \Phi_\nu(x) E_2(\Phi_\nu(x)\tau_\nu) \, dx, \tag{2.2.9}$$

$$\int_0^{t_\nu} \kappa_1(\tau_\nu - t) \, dt = 1 - \frac{1}{2}\kappa_2(\tau_\nu) - \frac{1}{2}\kappa_2(t_\nu - \tau_\nu). \tag{2.2.10}$$

For homogeneous and isothermal, which may exist locally, the above equations may be simplified as

$$J_\nu(\tau_\nu) = \beta(\tau_\nu) I_\nu^c(0) + \beta(t_\nu - \tau_\nu) I_\nu^c(t_\nu) + S_\nu(\tau_\nu)[1 - \beta(\tau_\nu) - \beta(t_\nu - \tau_\nu)], \tag{2.2.11}$$

where $\beta(\tau_\nu) = \frac{1}{2} K_2(\tau_\nu)$ is the escape probability that a photon escapes from a surface at an optical depth τ_ν from the surface. The value of J_ν for the semi-infinite plane parallel slab (i.e., $t_\nu \to \infty$) may be reduced as

$$J_\nu(\tau_\nu) \; = \; I_\nu^c(0)\beta(\tau_\nu) + S_\nu(1 - \beta(\tau_\nu)) \tag{2.2.12}$$

which is the expression used by deJong *et al.* (1980) (equation B-4 of Appendix B). Therefore, for optically thin cases where t_ν is finite the TH model can not be employed, instead the general expression as defined earlier (2.2.7) for J_ν should be used.

2.3 *Cooling efficiency*

The gas is generally cooled by hyperfine transitions of atoms, ions and rotational transitions of some of the molecules and its isotopes. The cooling efficiency is the function of level populations of different levels, which enter, in the cooling efficiency through the escape probability terms. To solve for level populations, statistical equilibrium for bound-bound levels m and n are established as

$$N_m(x)\left(\sum_{l=1}^{n} P_{lm}(x)\right) = \sum_{l=1}^{n} N_l(x)P_{lm}(x) \quad \text{for } l \neq m \tag{2.3.1}$$

where $N_m(x)$ is the number density of the species x in level m and $P_{lm}(x)$ is the rate coefficient for species x between levels l and m as

$$P_{lm} = B_{lm}J_\nu + C_{lm} \quad (m < l), \tag{2.3.2}$$

$$P_{ml} = A_{ml} + B_{ml}J_\nu + C_{ml} \quad (m > 1). \tag{2.3.3}$$

Here A and B are Einsteins coefficients for m and l transitions which correspond to frequency ν and C_{lm} and C_{ml} are the collisional excitation and deexcitation rates. The intensity of radiation J_ν is given by the expression as

$$\begin{aligned} J_\nu = {} & S_{ml}(\tau_\nu)[1-\beta(\tau_\nu)-\beta(t_\nu-\tau_\nu)] + I_\nu^c(0)\beta(\tau_\nu) + I_\nu^c(t_\nu)\beta(t_\nu-\tau_\nu) \\ & + \beta(\tau_\nu)\tau_\nu^d B(\nu, T_0) + \beta(t_\nu-\tau_\nu)\tau_\nu^d B(\nu, T_0), \end{aligned} \tag{2.3.4}$$

$$S_{ml} = 2h\nu_{ml}^3/(c^2(g_m N_l/g_l N_m - 1)). \tag{2.3.5}$$

Here $B(\nu, T_0)$ is the infrared radiation at frequency ν and temperature T_0, τ_ν^d is the optical depth at frequency ν due to dust.

Now the cooling efficiency in units of erg cm^{-3}sec^{-1} will become as

$$\Lambda_{ml} = N_m A_{ml} h\nu_{ml}\beta_{ml}^{\text{esc}}\left[1 - \frac{B(\nu, T_0)\beta(\tau_\nu)}{\beta_{ml}^{\text{esc}} S_{ml}}\right], \tag{2.3.6}$$

here, $\beta_{ml}^{\text{esc}} = \beta(t_\nu - \tau_\nu) + \beta(\tau_\nu)$.

In the limit $t_\nu \to \infty$ equation (2.3.6) is reduced to

$$\Lambda_{ml} = N_m A_{ml} h\nu_{ml}\beta(\tau_\nu)\left[1 - \frac{B(\nu, T_0)}{S_{ml}}\right]. \tag{2.3.7}$$

This is the same as equation (20) of deJong *et al.* (1980) used by Tielens & Hollenbach (1985a).

3. Physical parameters and assumptions

In the recent past a great deal of work has been done on M17 by Meixner & Tielens (1993). Madden *et al.* (1993); Robert & Pagani (1993); Meixner *et al.* (1992); Boreiko & Betz (1991); Stutzki *et al.* (1988); Harris *et al.* (1987); Rainey *et al.* (1987); Schulz & Krugel (1987); Zmuidzinas *et al.* (1986); Knee *et al.* (1985); and Thronson *et al.* (1983). Observationally it has been established that M17 is clumpy in nature. Most of the transitions at millimeter and sub-millimeter wavelengths e.g., CI(307 and 609μm), CII (158μm), OI (145μm), SiII(35μm) and high rotational transitions of CO molecules are optically thin except OI(63μm) and low lying rotational transitions of CO. In the light of these observational facts the semi-infinite slab of deJong *et al.* (1980), extensively used in the TH model, is not a safe assumption. Moreover, homogeneous cloud assumption is also not valid.

To take into account the observational facts the M17 is supposed to be clumpy in nature and to solve for escape probability the region is assumed to be finite slab. The relevant details of the mathematical formulations are discussed in section 2. The physical parameters of the study are discussed below.

- **FUV flux:** In order to study M17, FUV flux is taken 5.6×10^4 times more intense than the ambient interstellar field (1.2×10^{-4}ergs cm^{-2}sec^{-1} sr^{-1} of Habing (1968) from Meixner *et al.* (1992).
- **Line profile:** The line width is assumed to be mainly due to turbulent Doppler width in clump and interclump both. The turbulent velocities in clump and interclump are taken 1.5 and 7.8 km/sec respectively (Meixner & Tielene's 1992).
- **Density:** The clump and interclump are supposed to be imbedded and density of the regions are taken as a free parameter varied over a wide range ($100 \leq N \leq 10^7$ cm^{-3}). The purpose of variation in the density is only to see the qualitative behaviour of the cloud.
- **Attenuation:** The ultraviolet flux will be attenuated during the penetration deep into the cloud because of the dust and absorption by atoms, ions and molecules. The attenuation of radiation by dust is proportional to $\exp(-\tau_{uv})$ where τ_{uv} is the ultraviolet optical depth for ($912\ A^0 \leq \lambda \leq 2100 A^0$). The τ_{uv} depends upon the extinction coefficients K_ν and depth Z into the cloud from the boundary i.e., interface of HII/HI and for the present study we use

  $$\tau_{uv} = 4.2 \times 10^{-3} \mathrm{N\ Z}\ (1000/\lambda), \tag{3.1}$$

  (Meixner & Tielens 1993; Spitzer 1978).

  Further, to calculate the attenuation due to absorption in clump/interclump the abundances are first calculated by solving the coupled equations obtained from chemical equilibrium for atoms, ions and molecules. Absorption of radiation by neutral carbon, CO and H_2 has important bearing on the CII, CI, HI and H_2 abundances.
- **Thermal structure:** The heating mechanism discussed by Tielens & Hollenbach (1985) has been used. It is found that M17 is predominantly heated by FUV flux $\geq 912A^0$ mainly through photoelectric emission from the surface of dust grains. Deep inside the cloud other mechanism may be important too. The gas is generally cooled by the hyperfine transitions of atoms (CI and OI), ions (CII, SiII and FeII) and rotational transitions CO ($\Delta J = 1$ up to 20) and its isotopes and some other molecules. The cooling is the function of populations of different levels, which enters into the cooling rate equation through the probability of escape of radiation. To solve the level populations statistical equilibrium coupled equations are solved for different levels as discussed in section 2. The collisional rates are taken from Tielens & Hollenbach (1985).
- **Abundance:** In order to calculate the abundances of different species chemical equilibrium is solved at every point inside the cloud. The required reaction rates are taken from Miller *et al.* (1993) and Tielen & Hollenbach (1985).

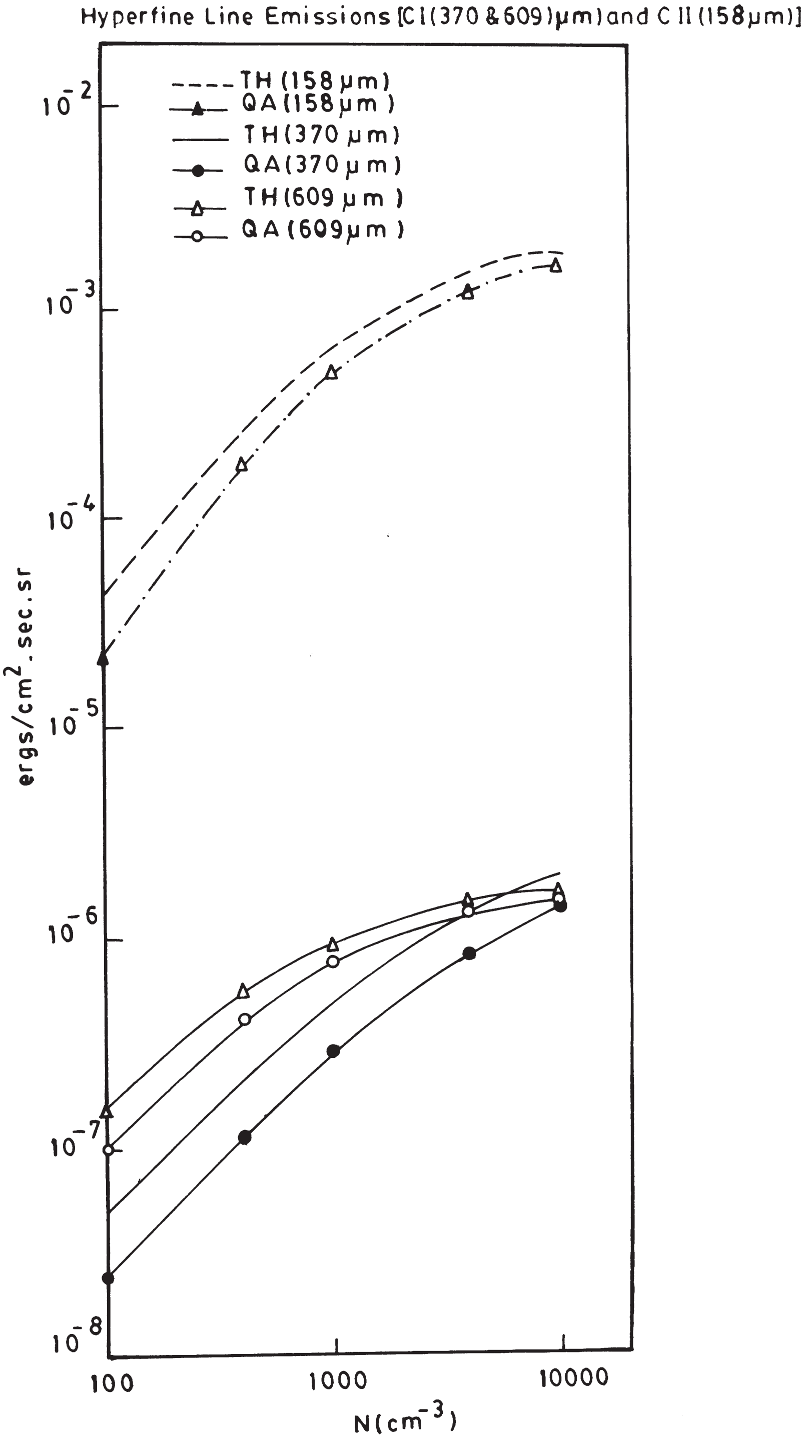

Figure 1. 'Intensity of line emission from interclump (ergs $\sec^{-1}\mathrm{cm}^{-2}\ \mathrm{sr}^{-1}$)' vs 'interclump density N(cm^{-3})' for $G_0 = 5.6 \times 10^4$ and clump density of $10^5\ \mathrm{cm}^{-3}$.

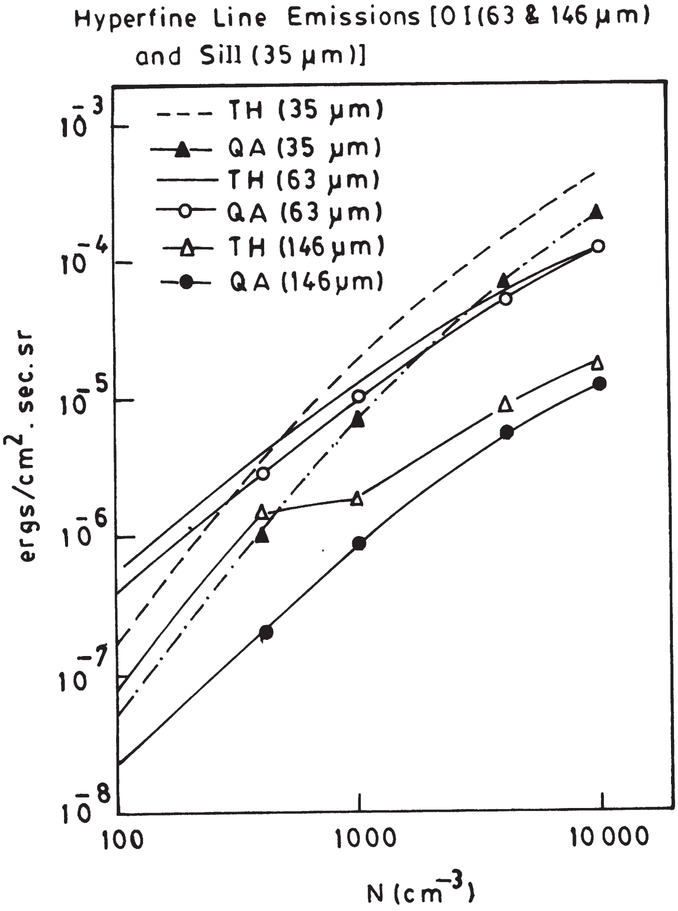

Figure 2. 'Intensity of line emission from interclump (ergs $\sec^{-1}\mathrm{cm}^{-2}\ \mathrm{sr}^{-1}$)' vs 'interclump density N(cm^{-3})' for $G_0 = 5.6 \times 10^4$ and clump density of $10^5\ \mathrm{cm}^{-3}$.

- **Filling factors:** The filling factors of the clump and interclump is based upon the size and density. If r_c is the average radius of the clump size distribution, the average length of the clump is defined as $4/3r_c \sim .32(P_0)^{1/3}$. Here P_0 is the volume filling factor. Generally the whole mass resides in clump as a result $P_0 n_c = n_{\mathrm{avc}}$ (average density). The interclump filling factor P_1 equals $(1 - P_0)$.

4. Results and discussion

For a comparative study of the TH model and present formalism (referred to as QA), calculations have been performed for line intensities of different cooling agents [CI (609μm and 370μm), CII (158μm), OI (146μm and 63μm), SiII(35μm) and rotational transitions of CO molecules]. These are plotted as a function of number density in the Figs. (1–3). It is quite clear from the figures that present calculations differ from those of TH model. The difference is large at low density where the radiation term dominates over the collisional one but the difference is narrowing down as den-

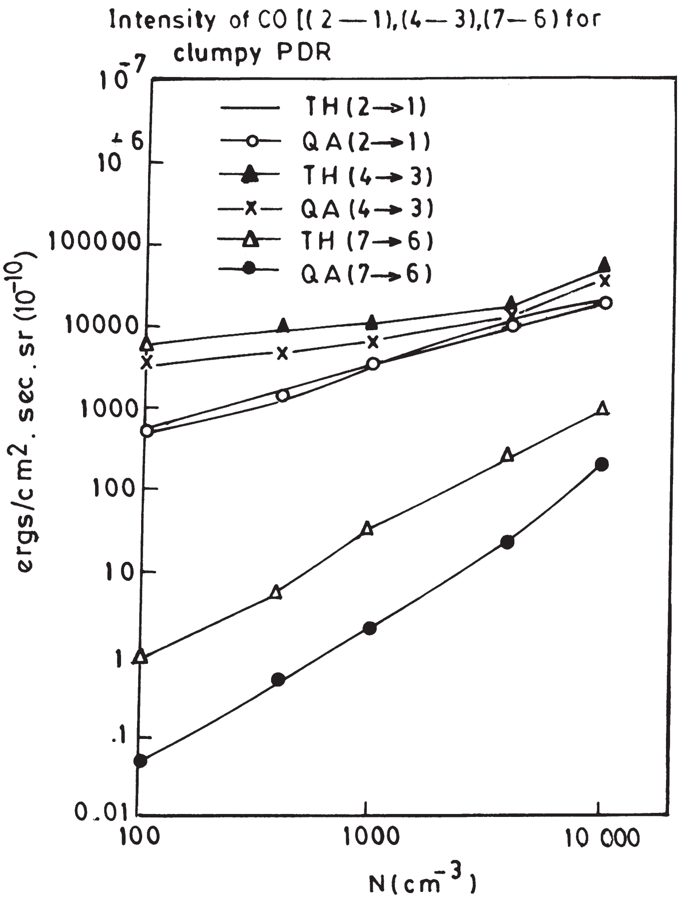

Figure 3. ‘Intensity of molecular lines from interclump (ergs $\sec^{-1}\mathrm{cm}^{-2}\ \mathrm{sr}^{-1}$)’ vs ‘interclump density $\mathrm{N}(\mathrm{cm}^{-3})$’ for $G_0 = 5.6 \times 10^4$ and clump density of $10^5\ \mathrm{cm}^{-3}$.

sity increases and finally both the curves merge together at densities higher than critical density. However, the behaviour of the optically thin lines differs from that of optically thick lines. Thus the optical depth parameter divides the PDR cooling lines into two groups: **(a)** Optically thin lines: [CI (609 μm and 370 μm) and CII (158 μm)] (Fig. 1), OI [(146μm) and SiII(35μm)] (Fig. 2) and [high rotational transitions of CO (e.g. 7→ 6 transitions)]: (Fig. 3) and **(b)** optically thick lines OI [(63μm)] (Fig. 2) and [low rotational transitions of CO (e.g., 2→ 1 and 4→3 transitions)] (Fig. 3).

It has been found that optically thin lines in QA model differ substantially (in some cases an order of magnitude) from that of TH model as long as radiation term dominates over the collisional one (Figs. 1, 2 and 3). In such circumstances assumption of semi-infinite slab will be erroneous and hence TH model cannot be employed. However, at density much higher than critical density of the line emission, line intensities calculated using TH and QA model yields the same value. However, for CO (14→13 transition) it has been observed that both the models differ by an order of magnitude even at sufficiently high density. For optically thick lines (Figs. 2, 3 and 4), no substantial

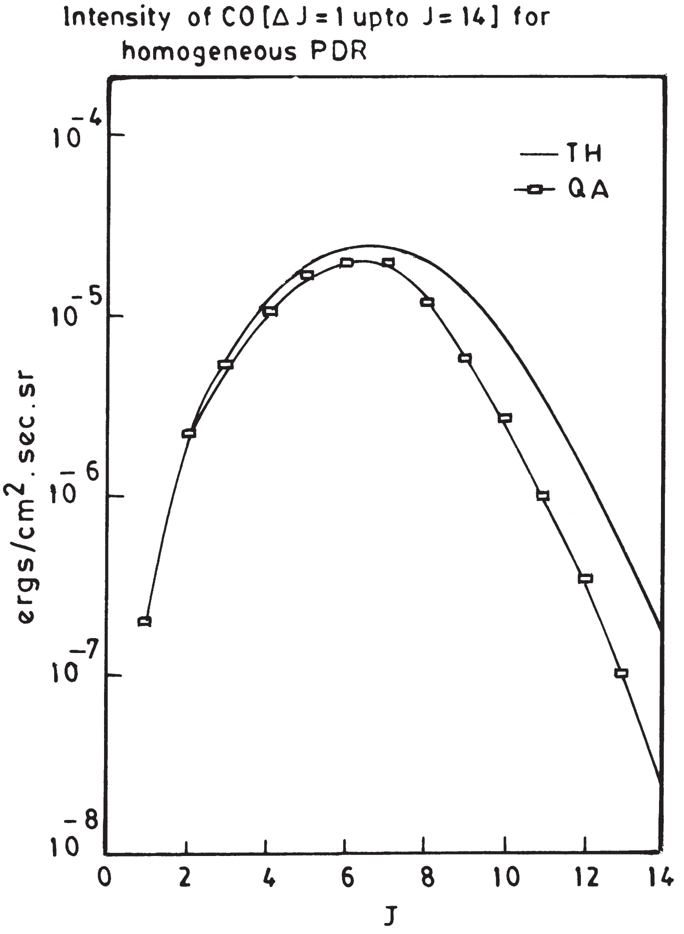

Figure 4. 'Intensity of lines (ergs $\sec^{-1}\mathrm{cm}^{-2}$ sr^{-1})' in homogeneous photodissociation region of density 10^5 (cm^{-3}) and $G_0 = 5.6 \times 10^4$.

difference is noticed. However, for sufficiently large optical depths ($t_\nu \rightarrow \infty$) the cloud is behaving like semi-infinite slab and equations (2.2.12 and 2.3.6) will be reduced to that of equations B-4 of Appendix B and 20 of deJong *et al.* (1980) and the present formalism will be reduced to TH model. Therefore for optically thick lines TH and QA model do not differ significantly. In Fig. 4, line intensity of various rotational transitions ($J + 1 \rightarrow J$) of CO molecule have been plotted for homogeneous PDR of density 10^5 cm^{-3} and $G_0 = 5.6 \times 10^4$. From the figure it is quite obvious that for high rotational transitions which are optically thin QA and TH models differ significantly, whereas the difference is narrowing down as we move towards the optically thick lines i.e., lower transitions.

The analysis of various fine structure lines and FIR continuum for $G_0 = 5.6 \times 10^4$ yields a density $\sim 4 \times 10^3$ and a temperature of ~ 300 K for atomic gas in homogeneous models. However, homogeneous models can not reproduce the spatial distribution of line emissions. The homogeneous PDR with typical density of 4×10^3 have an edge-on extension ~ 0.01 pc contrary to the observational facts. CII (158 μm)

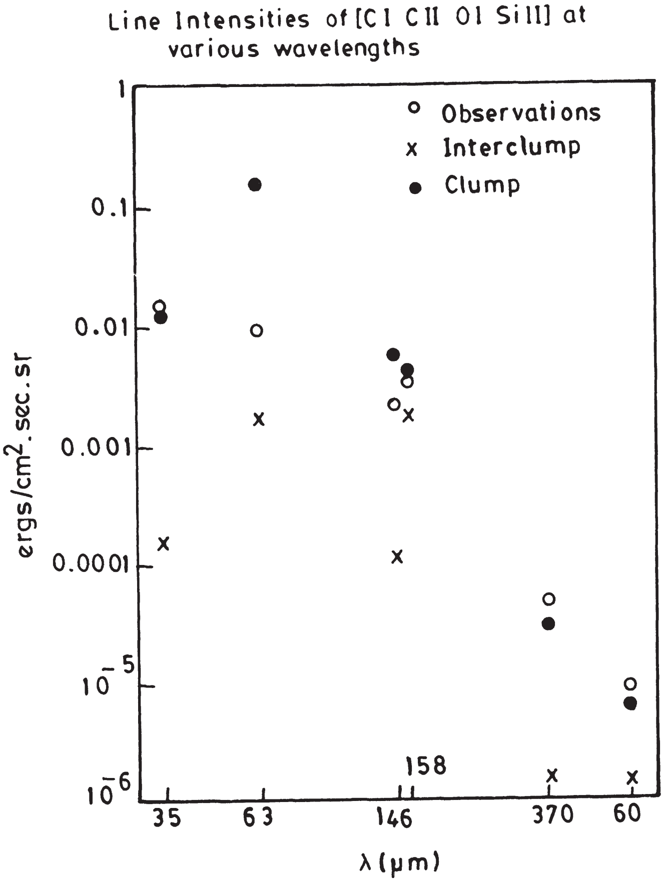

Figure 5. Calculated line intensities (ergs $\sec^{-1}\text{cm}^{-2}$ sr^{-1}) of fine structure line emissions of CI (370 and 609 μm), CII (158 μm), OI (163 and 146 μm) and SiII (35 μm) at various wavelengths noted against each atom and ion or interclump density = 4×10^3 (cm^{-3}) and clump density $= 6 \times 10^5(\text{cm}^{-3})$ and $G_0 = 5.6 \times 10^4$.

Observed values (references): [CI (370 μm) Zmuidzinas *et al.* (1986)], [CI (609 μm) Knee *et al.* (1985)], [CII (158 μm) Stutzki *et al.* (1988)], [OI (63 μm) Meixner *et al.* (1992)], [OI (146 μm) Meixner *et al.* (1992)] and [SiII (35 μm) Meixner *et al.* (1992)].

emission when viewed edge-on extends 1 PC to 4 PC in NGC 1977, Orion, NGC 2023, W3 and M17W (Stacey *et al.* 1993; Stutzki *et al.* 1988; Howe *et al.* 1991). The spatial distribution of CII (158 μm) line emission indicate a deep penetration of UV radiation into the region. Further observed velocity distribution is also found to be drastically different at locations of CII emissions (Meixner *et al.* 1992). These facts led to the assumption of two-component models of PDRs in the form of clump and interclump by Meixner & Tielens (1993).

Theoretical calculations have been performed for line intensities of FIR and sub-millimeter transitions to study the M17 region using the present formalism. For that purpose density is taken as free parameter. But turbulent velocities for clump and interclump are taken as 1.5 and 7.8 km/sec and $G_0 = 5.6 \times 10^4$ from Meixner *et al.* (1992). The calculated and observed line intensities at millimeter and sub-millimeter

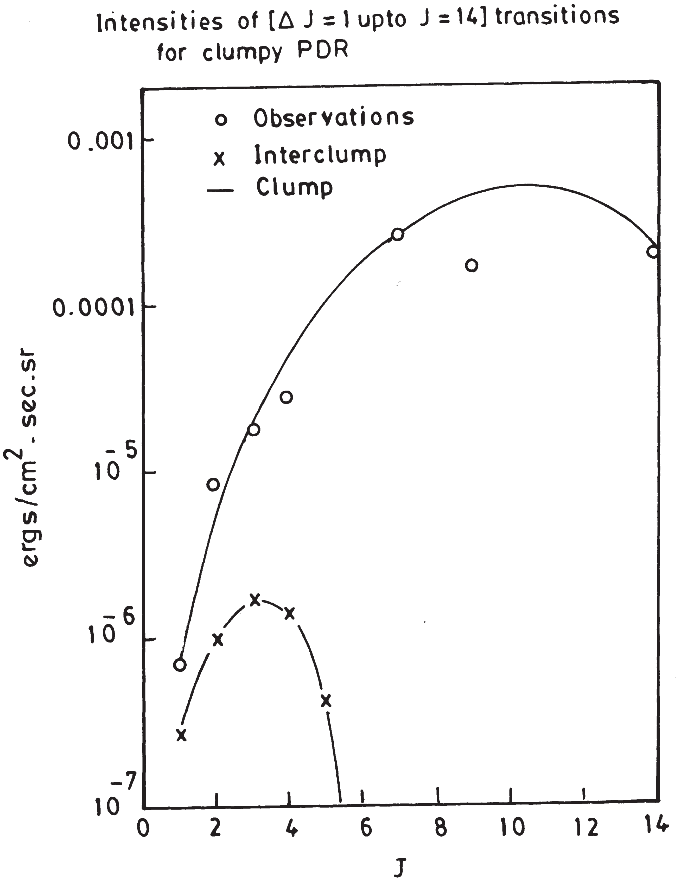

Figure 6. Calculated line intensities (ergs $sec^{-1}cm^{-2}$ sr^{-1}) for interclump density = 4×10^3 (cm^{-3}) and clump density $= 6 \times 10^5$(cm^{-3}) and $G_0 = 5.6 \times 10^4$ for various J and $\Delta J = 1$.

Observed values (references): [(1→ 0) Thronson *et al.* (1983)], [(2→ 1) Meixner *et al.* (1992)], [(3→ 2) Rainey *et al.* (1987)], [(4→ 3) Schulz & Krugel (1987)], [(7→ 6) Stutzki *et al.* (1988)], [(9→ 8) Boreiko & Betz (1991)] and [(14→ 13) Harris *et al.* (1987)].

wavelengths for hyperfine transitions of atoms [CI (370 and 609μm); OI (63 and 146μm)], ions [CII (158 μm); and SiII (35 μm)] and rotational transitions of CO ($1 \rightarrow 0,\ 2 \rightarrow 1,\ 3 \rightarrow 2,\ 4 \rightarrow 3,\ 7 \rightarrow 6,\ 9 \rightarrow 8$ and 14→ 13) are compared with that of the observed values in Figs. 5 and 6. The following conclusions may be drawn from these two figures:

- The contribution to the line intensities from the interclump is negligibly small as compared to that of the clump except CII (158 μm) in which case both are comparable (Fig. 5). This explains the large spatial extent observed for CII (158 μm) line.
- The line intensities of almost all the listed fine structure transitions from clump agree fairly well with the observations except OI (63 μm) (Fig. 5). In case of OI (63 μm) the interclump intensity is low enough than the clump but it is close to the observed value. Since the temperature of the interclump is found to be lower

than the clump it is highly probable that line OI (63 μ m) originating from clump may be absorbed. In such circumstances calculated intensity will come out to be close to the observed one.

- The line intensities for the rotational transitions of CO molecule are plotted in Fig. 6 for the levels up to $J = 14$ for the clump and interclump both. Observed lines are also plotted in the same figure. It is found that the line intensities from the clump agree fairly with those of observed values. However line intensities from interclump are negligibly small as compared to clump except for the lowest transition. However, first transitions of CO may be observed from the extended region. Meixner *et al.* (1992) have shown that $7 \rightarrow 6$ and $2 \rightarrow 1$ transitions of CO peak together. This has been confirmed from the calculations that both originate from clump. Further spatial extended observation of rotational transitions of CO will give more insight to the clump structure of the M17 region.
- The agreement of calculated values with those of the observations over a wide range of fine structure line emissions and rotational transitions favour clumpiness in the region and favoured densities for the clump and interclump regions are 6×10^5 and 4×10^3 cm^{-3} respectively.
- The values obtained by QA closely match with the results of Meixner & Tielens (1993) obtained earlier with a similar model (TH and Boisse formalism) for optically thin lines.

Acknowledgement

The authors acknowledge the Chairman, Department of Physics, Professor S. K. Singh for providing necessary computational facilities. Discussions with Mr. Badr-e-Alam were useful and we also wish to acknowledge his help in reading the manuscript.

References

Averett, E. H., Hummer, D. G. 1965, *Mon. Not. R. astr, Soc.*, **130**, 295.

Bennet, C. L., Fixsen, P. J., Mather, J. C., Moseley, S. H., Wright, E. L., Eplee Jr., R. E., Gales, J., Hawagama, T., Issacman R. B., Shafer R. A., Turpie K. 1994, *Astrophys. J.*, **434**, 587.

Boisse, P. 1990, *Astr. Astrophys.*, **228**, 483.

Boreiko, R. T., Betz, A. L. 1991, *Astrophys. J.*, **369**, 382.

Castets, A., Duvert, G., Durtey, A., Bally, J., Langer, W. D., Wilson, R. W. 1990, *Astron. Astrophys.*, **234**, 469.

deJong, T., Dalgarno, A., Boland, W. 1980, *Astr. Astrophys.*, **91**, 68.

Habing, H. J. 1968, *Bull. Astr. Inst. Netherlands* **19**, 421.

Harris, A. I., Stutzki, J., Genzel, R., Lugten, J. B., Stacey, G. J. and Jaffe, D. T. 1987, *Astrophys. J.*, **322**, L49.

Herrmann, F., Madden, S. C., Nikola, T. Poglitsch, A., Timmermann, R. 1997, *Astrophys. J.*, **481**, 343.

Howe, J. E., Jaffe, D. T., Genzel, R., Harris, A. I., Stacey, G. J., Stutzki, J. 1991, *Astrophys. J.*, **373**, 158.

Jackson, J. M., Kramer, K. E. 1999, *Astrophys. J.*, **512**, 260.

Kemper, C., Spaans, M., Jansen, D. J., Hogerheijde, M. R., van Dishoek, E. F., Tielens, A. G. G. M. 1999, *Astrophys. J.*, **514**, 649.

Knee, J., Blake, G. A., Phillips, T. G., Huggins, P. J., Beichman, C. A. 1985, *Astrophys. J.*, **299**, 967.

Luhman, M. L., Jaffe, D. T., Sternberg, A., Herrmann, F., Poglitsch, A. 1997, *Astrophys. J.*, **482**, 298.

Madden, S. C., Geis, N., Genzel, R., Herrmann, F., Jackson, J., Poglitsch, A., Stacey, G. J., Townes, C. H. 1993, *Astrophys. J.*, **407**, 579.
Meixner, M., Tielens, A. G. G. M. 1993, *Astrophys. J.*, **405**, 216.
Meixner, M., Haas, M. R., Tielens, A. G. G. M., Erickson, E. F., Werner, M. 1992, *Astrophys. J.*, **390**, 499.
Miller, Y., Fort, B., Kneib, J. 1993, *Astrophys. J.*, **407**, 33.
Rainey, R., White, G. J., Gately, I., Ilyashi, S. S., Kaifu, N., Griffin, M. J., Monteiro, T. S., Cronin, N. J., Scivetti, A. 1987, *Astron. Astrophys.*, **171**, 252.
Robert, C., Pagani, L. A. 1993, *Astron. Astrophys.*, **271**, 282.
Schulz, A., Krugel, E. 1987, *Astron. Astrophys.*, **171**, 252.
Spitzer Jr., 1978, *Physical Processes in the Interstellar Matter* (John Wiley).
Stacey, G. J., Jaffe, D. T., Geis, N., Genzel, R., Harris, A. I., Poglitsch, Stutzki, J., Townes, C. H. 1993, *Astrophys. J.*, **404**, 219.
Steiman-Cameron, T. Y., Haas, M. R., Tielens, A. G. G. M. 1997, *Astrophys. J.*, **478**, 261.
Strorzer, H., Hollenbach, D. 1999, *Astrophys. J.*, **515**, 669.
Stutzki, J., Stacey, G. J., Genzel, R., Harris, A. I., Jaffe, D. T., Lugten, J. B. 1988, *Astrophys. J.*, **332**, 379.
Tauber, J., Goldsmith, P. F. 1990, *Astrophys. J.*, **356**, L63.
Thronson Jr., H. A., Lada, C. J. 1983, *Astrophys. J.*, **291**, 175.
Tielens, A. G. G. M., Hollenbach, D. 1985, *Astrophys. J.*, **291**, 722.
Wolfire, M. G., Tielens, A. G. G. M., Hollenbach, D. 1990, *Astrophys. J.*, **358**, 116.
Zmuidzinas, J., Betz, A. L., Goldhaber, D. M. 1986, *Astrophys. J.*, **307**, L75.

J. Astrophys. Astr. (2003) **24,** 85–97

Comparing Maps to Symplectic Integrators in a Galactic Type Hamiltonian

N. D. Caranicolas & N. J. Papadopoulos *Department of Physics, Section of Astrophysics, Astronomy and Mechanics, University of Thessaloniki, 540 06 Thessaloniki, Greece.*
e-mail: caranic@astro.auth.gr

Received 2003 March 31; accepted 2003 June 27

Abstract. We obtain the $x - p_x$ Poincare phase plane for a two dimensional, resonant, galactic type Hamiltonian using conventional numerical integration, a second order symplectic integrator and a map based on the averaged Hamiltonian. It is found that all three methods give good results, for small values of the perturbation parameter, while the symplectic integrator does a better job than the mapping, for large perturbations. The dynamical spectra are used to distinguish between regular and chaotic motion.

Key words. Galaxies: orbits—regular and chaotic motion maps: averaged Hamiltonian—stability.

1. Introduction

About four decades ago most astronomers believed that stellar orbits in elliptical galaxies were regular. Recent observations, both, from the Hubble Space telescope as well as from ground-based telescopes, revealed that the star density in elliptical and S0 galaxies rises towards the centre in a power low cusp (see Byun *et al.* 1996). Those observations strongly suggest that a large number of orbits passing through the centre of the galaxy must be chaotic.

The work presented here exploits recently developed tools from galactic dynamics as well as from non linear dynamics, in order to better understand the properties of orbits in a simple local galactic Hamiltonian describing motion near the centre of an elliptical galaxy. Among others, we shall try to find the fraction of chaotic vs regular orbits and how it changes using different methods to obtain the corresponding Poincare phase plane.

Our dynamical model is given by the equation

$$V = \frac{1}{2}\left(x^2 + 4y^2\right) - \epsilon\left[\alpha x^4 y^2 + \beta\left(x^4 + y^4\right)\right], \tag{1}$$

where α and β are parameters while ϵ is the perturbation strength.

The following lines of arguments justify the choice of the potential (1).

(i) This potential is a two dimensional perturbed harmonic oscillator and can be derived by expanding global potentials near an equilibrium point, that is the centre of the galaxy.

(ii) The potential describes motion near the centre of an elliptical galaxy and displays chaotic motion. As it was mentioned before, observations suggest that a number of orbits in the central regions of elliptical galaxies are chaotic. Therefore, equation (1) seems to be a good description for the behavior of orbits in the central parts of an elliptical galaxy.

(iii) The fourth and sixth order terms have been included in order to justify the symmetry of the elliptical galaxy. In particular the coupling sixth order term is the basic term that was selected in order to produce the desired 1:2 resonant results for the map.

Potentials of the form (equation 1), that is potentials made up of perturbed harmonic oscillators are among the most studied in non-linear dynamics (see Elipe 2001; Elipe & Deprit 1999; Caranicolas & Innanen 1992).

The paper is organized as follows: The map and the position of periodic orbits are given in section 2. In section 3 we compare the Poincare phase planes obtained by conventional numerical integration, the symplectic integrator and the map. In section 4 we compare the dynamical spectra for different types of orbits obtained by the above three methods. Finally, section 5 contains a discussion and the conclusion of this work.

2. The map and the position of periodic orbits

The Hamiltonian to the potential (equation 1) is

$$H = \frac{1}{2}\left(p_x^2 + p_y^2\right) + V = h, \tag{2}$$

where p_x, p_y are the momenta per unit mass conjugate to x and y while h is the numerical value of H. In order to obtain the averaged Hamiltonian we follow the steps described in (Caranicolas 1990).

The averaged Hamiltonian is

$$\frac{3\epsilon\beta}{2}\left[J^2 + \frac{(\Lambda - J)^2}{16}\right] + \epsilon\alpha J^2(\Lambda - J)\left[\frac{3}{8} - \frac{1}{16}\cos 4\theta\right], \tag{3}$$

while the corresponding map reads

$$\begin{aligned} J_{n+1} &= J_n + f(J_{n+1}, \theta_n) \\ \theta_{n+1} &= \theta_n + S(J_{n+1}) + g(J_{n+1}, \theta_n), \end{aligned} \tag{4}$$

where

$$\begin{aligned} f(J,\theta) &= -\frac{1}{4}\epsilon\alpha J^2(\Lambda - J)\sin 4\theta \\ S(J) &= \frac{3\epsilon\alpha J}{8}(2\Lambda - 3J) + \frac{3}{16}\beta\epsilon(17J - \Lambda), \\ g(J,\theta) &= -\frac{1}{16}\epsilon\alpha J(2\Lambda - 3J)\cos 4\theta \end{aligned} \tag{5}$$

and we have set $\Lambda = h$. The fixed points of (4) are at

$$(\mathbf{i})\ J = \frac{51\beta + 10\alpha\Lambda - \sqrt{-180\alpha\beta\Lambda + (51\beta + 10\alpha\Lambda)^2}}{30\alpha}, \tag{6}$$

when $\theta = k\pi/4$ and $k = 0, 2, 4, 6, \ldots$

$$(\mathbf{ii})\ J = \frac{51\beta + 14\alpha\Lambda - \sqrt{-252\alpha\beta\Lambda + (51\beta + 14\alpha\Lambda)^2}}{42\alpha}, \tag{7}$$

when $\theta = (k+1)\pi/4$ and $k = 0, 2, 4, 6, \ldots$

$$(\mathbf{iii})\ J = 0, \quad \text{for any} \quad \theta. \tag{8}$$

We consider positive values for β while α is negative because, when α is negative, the system displays considerable chaotic motion. We have four resonant fixed points (i) and four resonant fixed points (ii). It is well known that the map can also give the stability of the resonant periodic points (i) and (ii). Algebraic calculations show that the corresponding indices of stability are too lengthy expressions to be given analytically and it is better to be calculated numerically for each case using the particular values of the parameters.

3. The structure of phase plane

Let us now come to see the structure of the $x - p_x$ Poincare phase plane of the Hamiltonian equation (2). In order to visualize the properties of orbits of the system we decided to use three different ways to obtain the corresponding phase plane, that is conventional numerical integration, a second order symplectic integrator and the map. Symplectic integrations are widely used to study problems in non linear dynamics and celestial mechanics. The most popular algorithm is the second-order symplectic integrator. The reader can find further details on symplectic integrators in (Feng & Qin 1987).

Figures 1, 2 and 3 show the $x - p_x$ phase plane of the system, derived by numerical integration, symplectic integrator and the map respectively. The values of the parameters are $\alpha = -1.5$, $\beta = 0.1$, $\epsilon = 0.05$, $\Lambda = 2$. In the case of the map, we return to the original x, p_x variables through $x = (2J)^{1/2}\cos\theta$, $p_x = -(2J)^{1/2}\sin\theta$. It is evident that in all three cases the corresponding phase planes look very similar. All orbits seem to be regular while the chaotic areas, if any, are negligible.

Figures 4, 5 and 6 are the same as figures 1, 2 and 3 but for $\epsilon = 0.30$. Here things look different. One observes that the majority of orbits are regular while there is a considerable chaotic layer around the separatrix. The chaotic layer obtained by numerical integration and the symplectic integrator is about the same width while that obtained by the map is thicker and distorted. One also observes that the inner invariant curves in all three cases look very similar while the outer invariant curves, derived using the map, are “more circular” than those obtained by numerical integration or using the symplectic integrator.

Our numerical calculations suggest that, for small values of the perturbation parameter ϵ, all three methods give very good results. In this case we believe that one must prefer to use the map, because the map gives also analytical results for the position and the stability characteristics of the resonant periodic orbits. Furthermore, the map is generally faster than the other two methods. For large values of the perturbation parameter, one must prefer the method of symplectic integrator, because it gives better results than the map and it is generally faster than numerical integration. Here, we must emphasize that the symplectic integrator does a better job in cases when there are large chaotic regions where the map fails to describe the true phase plane of the system (see figures 6 and 7 in Caranicolas & Vozikis 1999).

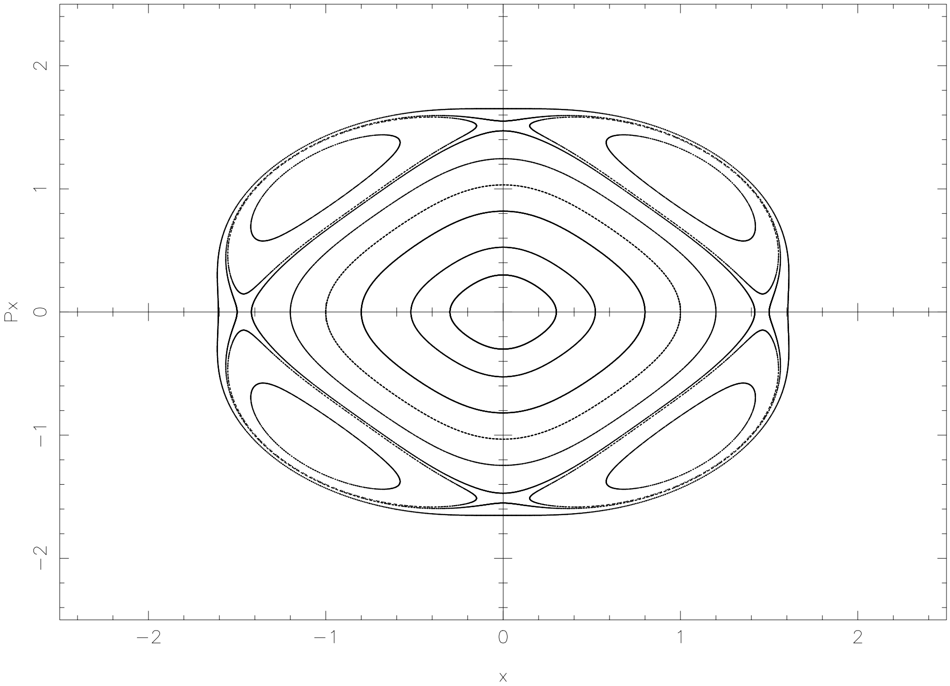

Figure 1. The $x - p_x$ phase plane of the Hamiltonian (2) derived by numerical integration. The values of the parameters are $\epsilon = 0.05,\ h = 2, \alpha = -1.5, \beta = 0.1$.

4. Comparison of dynamical spectra

In this section we shall use the new dynamical spectrum, introduced by Karanis & Caranicolas (2002), to distinguish between regular and chaotic in the Hamiltonian (equation 2). Furthermore, we shall compare the spectra produced by numerical integration, the symplectic integrator and the map. In order to help the reader, we give the definition of the new spectrum.

We define the parameter r as

$$r_i = \frac{x_i}{p_{iy}}, \tag{9}$$

where x_i, p_{iy} are the successive values of the coordinate x and the momentum p_y per unit mass, conjugate to coordinate y, on the $x - p_x$ phase plane, respectively. We call the dynamical spectrum of the parameter r, its distribution function

$$S(r) = \frac{\Delta N(r)}{N dr}, \tag{10}$$

where $\Delta N(r)$ is the number of values of r in the intervals $(r, r + dr)$ after N iterations.

Figures 7(a–c) show the $S(r)$ spectrum for a regular orbit derived using numerical integration (figure 7a), the symplectic integrator (figure 7b) and the map (figure 7c). Initial conditions are $x = 0.4$, $p_x = 0$, while the number of iterations is $N = 20000$. The values of the parameters are $\alpha = -1.5$, $\beta = 0.1$, $\epsilon = 0.05$, $\Lambda = 2$. One observes

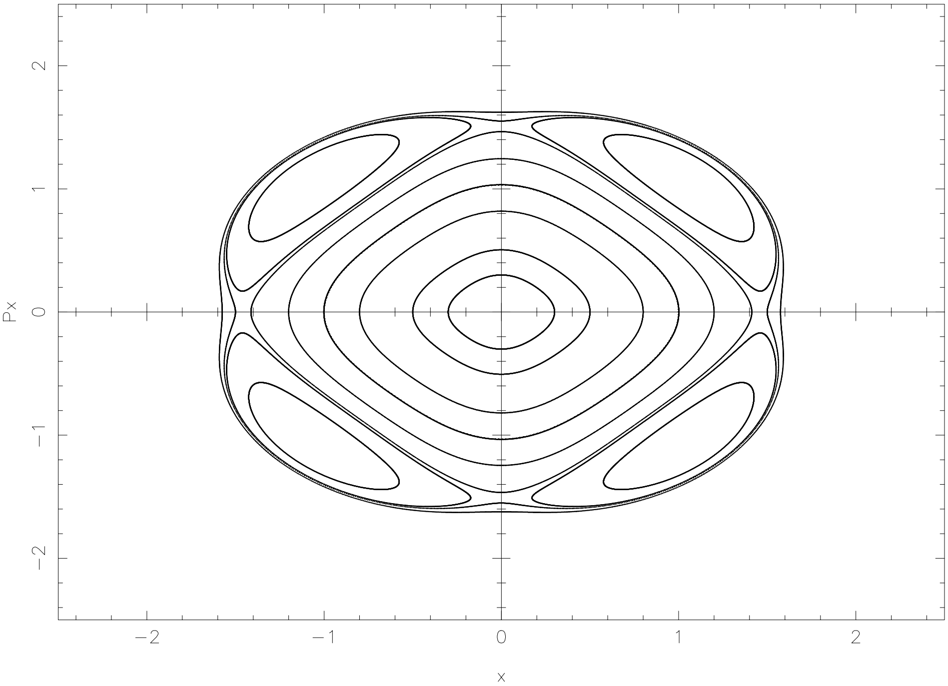

Figure 2. The $x - p_x$ phase plane of the Hamiltonian (2) derived using the symplectic integrator. The values of the parameters are as in Fig. 1.

that all three spectra are well defined "U type" spectra, which are typical for regular motion. Note that the three spectra are very similar.

Figures 8(a–c) show the $S(r)$ spectrum for a regular orbit producing two islands. Initial conditions are $x = 1.4$, $p_x = 0.8$, while the number of iterations is $N = 20000$. The values of the parameters are as in figure 7. Again figure 8(a) was derived using numerical integration, (figure 8b) using the symplectic integrator and (figure 8c) using the map. In all three cases we observe two separate "U type" spectra. It is well known (see Karanis & Caranicolas 2002) that the $S(r)$ spectrum signals island motion. Here we must remember that it is not possible to tell from the number of spectra what the real number of islands is. In the present case, we have two spectra corresponding to the two islands, because the two islands do not produce overlapping projections on the x-axis. Note that the three double spectra are of the same type but one can see some differences. The spectra produced by the map are wider than those produced by the two other methods. Furthermore the spectra derived using the symplectic integrator are similar to those produced by numerical integration but appear more crispy.

Figures 9(a–c) show the $S(r)$ spectrum for a chaotic orbit. The initial conditions are $x = 1.4$, $p_x = 0$ for the figure 9(a) and 9(b), which are produced by numerical integration and the symplectic integrator, while for the figure 9(c) produced by the map the initial conditions are $x = 1.57$, $p_x = 0$. This happens because the chaotic layer appears for different initial conditions in the map. The number of iterations is $N = 20000$ in all cases. The values of the parameters are the same as in figure 7, except for the value of ϵ which is 0.30. As one can see, in all cases the spectrum is a typical chaotic spectrum with a large number of small as well as large peaks.

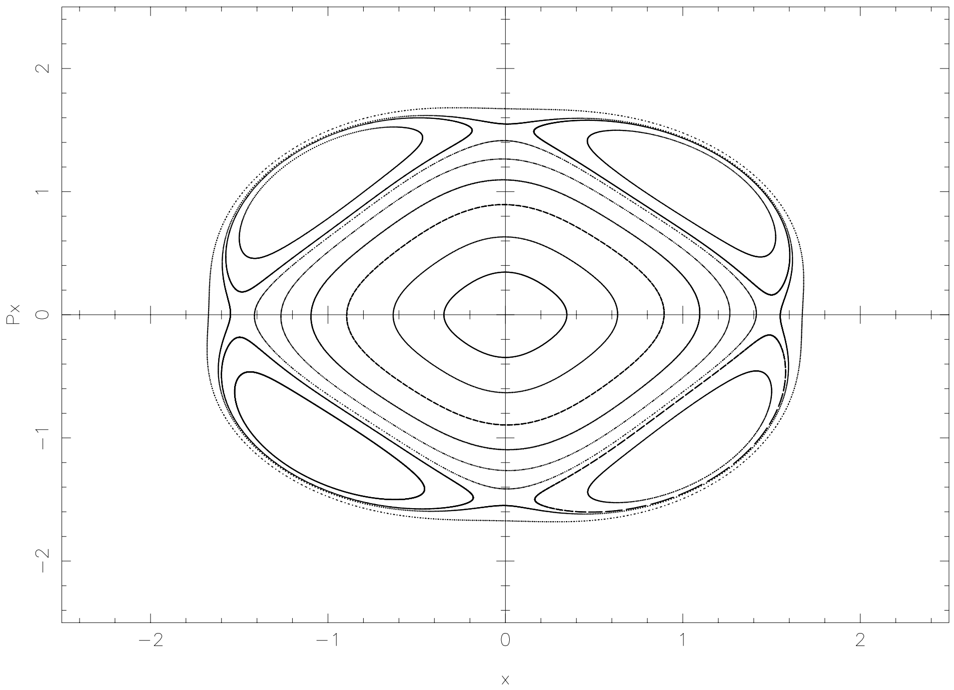

Figure 3. The $x - p_x$ phase plane of the Hamiltonian (2) derived using the map. The values of the parameters are as in Fig. 1.

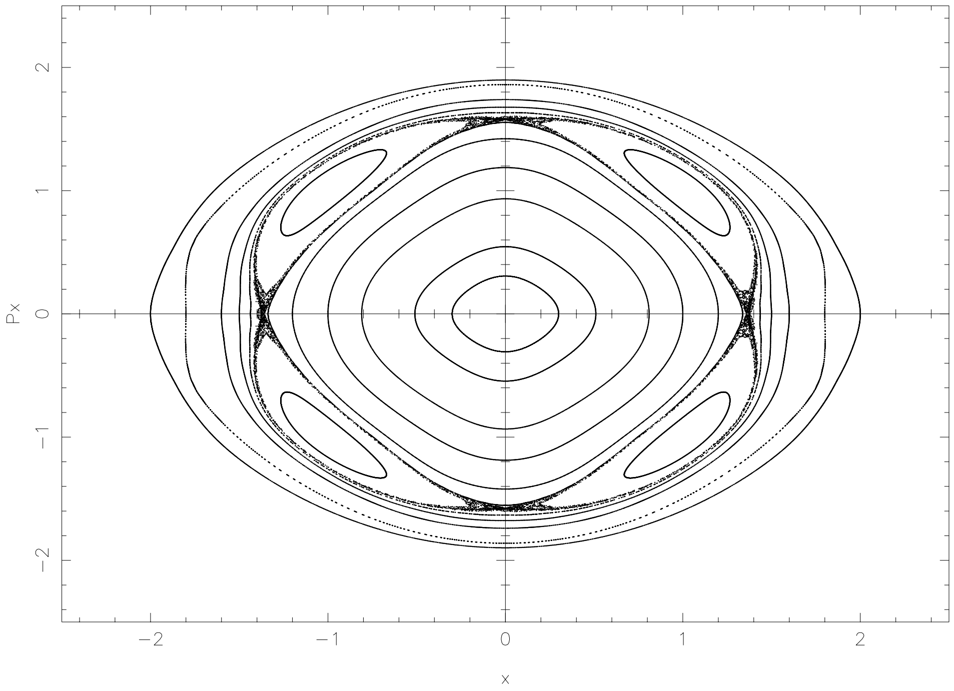

Figure 4. Same as Fig.1 when $\epsilon = 0.30$.

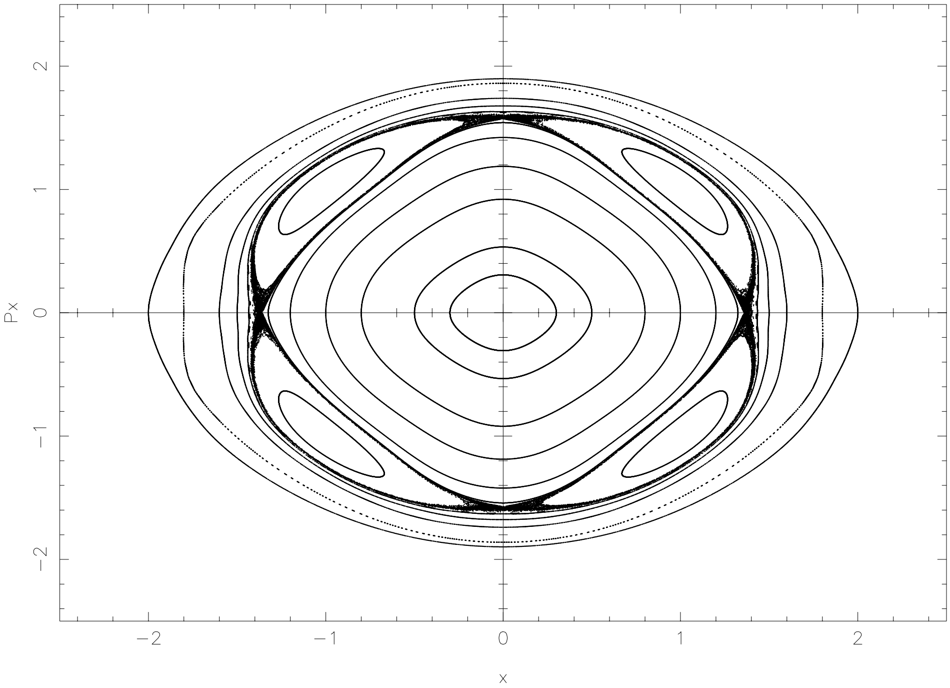

Figure 5. Same as Fig. 2 when $\epsilon = 0.30$.

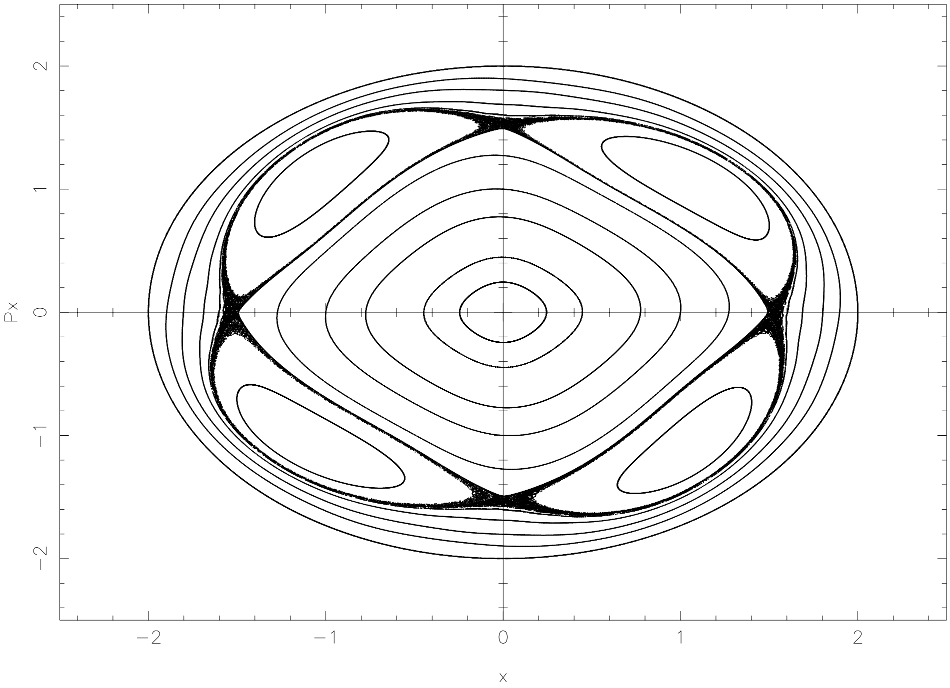

Figure 6. Same as Fig. 3 when $\epsilon = 0.30$.

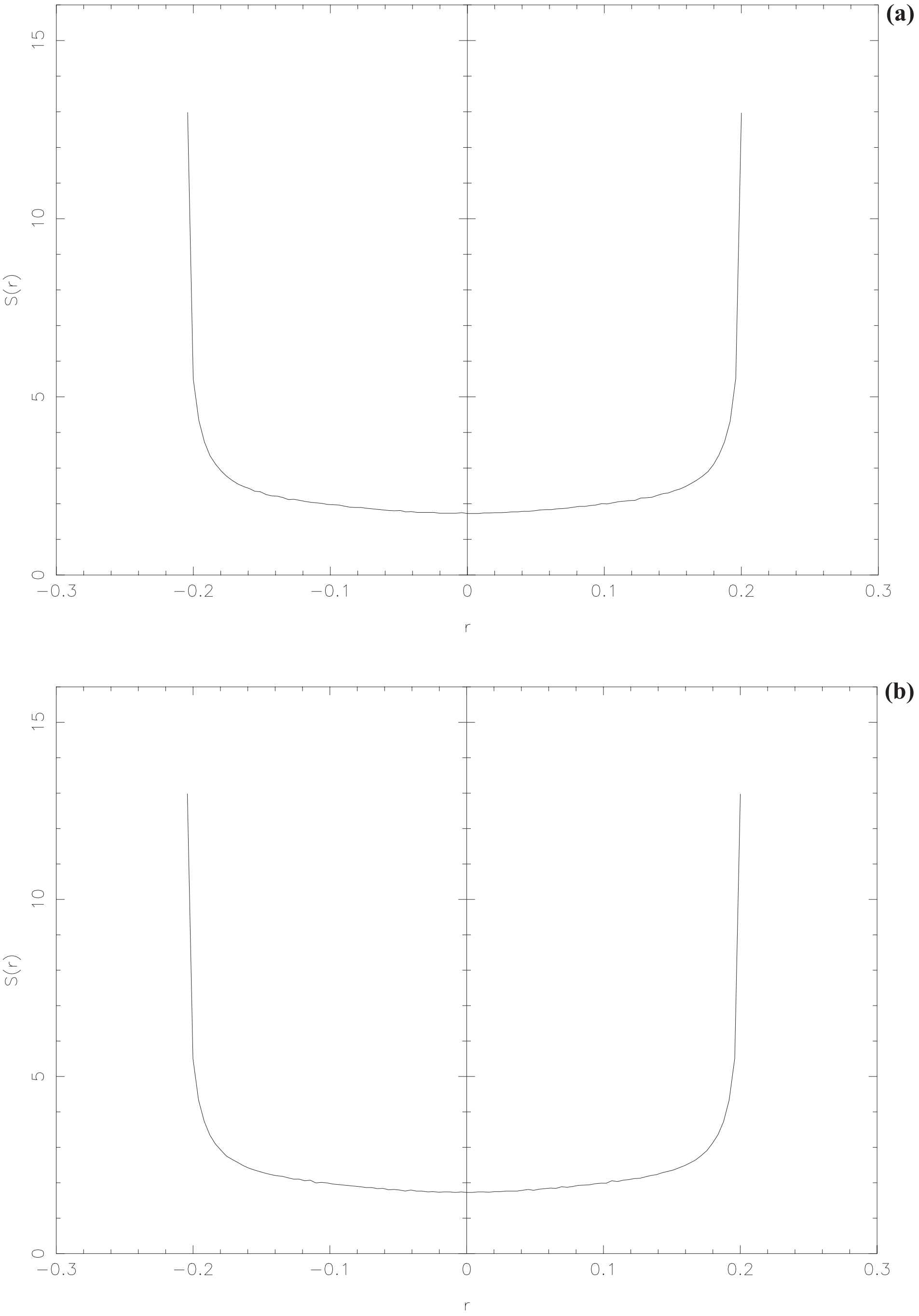

Figure 7 (a and b)**.** (*Continued*)

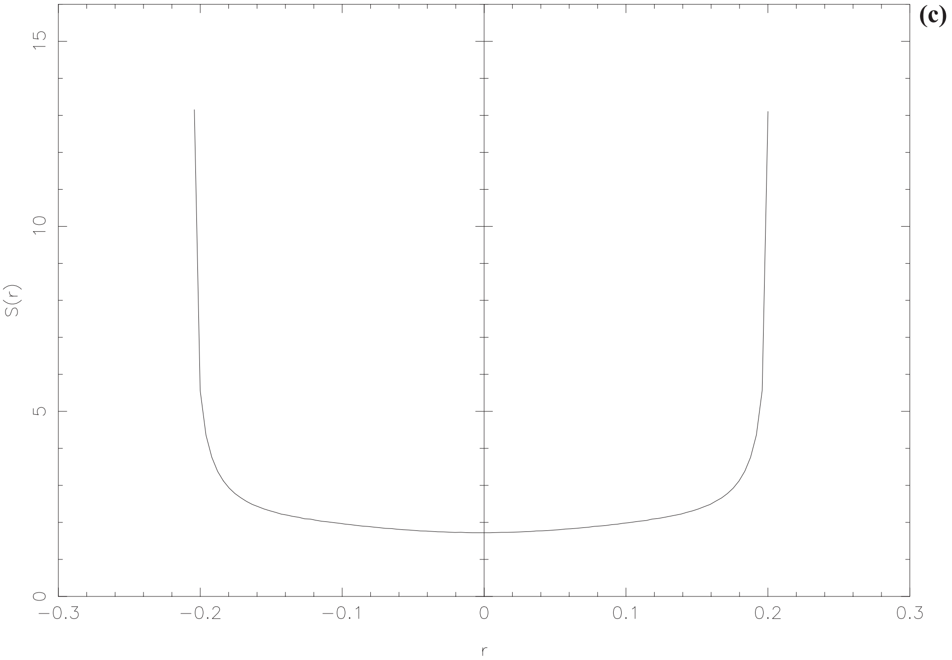

Figure 7 (a–c). The $S(r)$ spectrum for a regular orbit described in text. **(a)** Numerical integration; **(b)** Symplectic integrator; **(c)** Map. The values of the parameters are as in Fig.1.

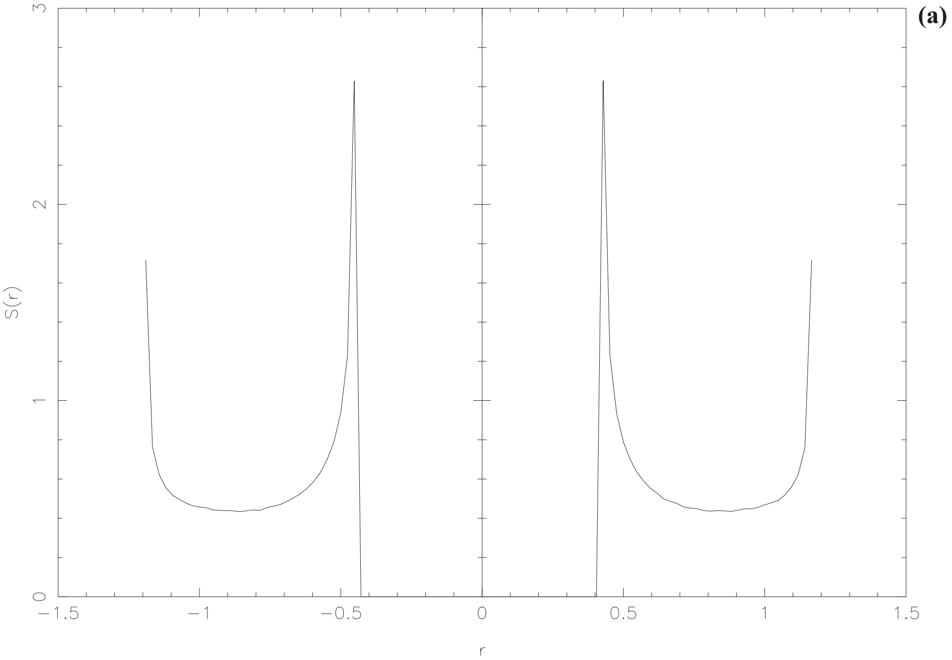

Figure 8(a). (*Continued*)

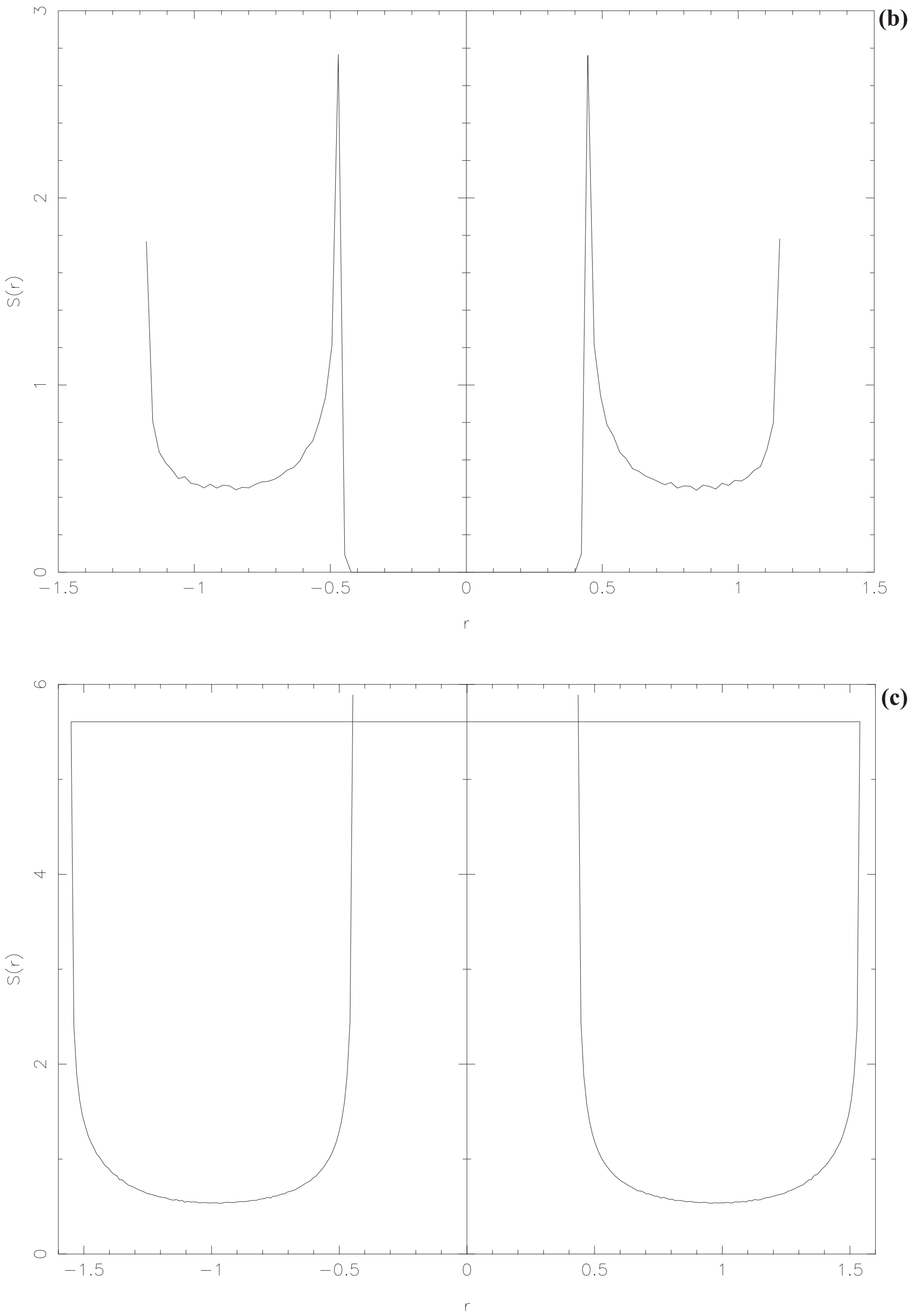

Figure 8 (a–c). The $S(r)$ spectrum for a regular orbit producing two islands. **(a)** Numerical integration; **(b)** Symplectic integrator; **(c)** Map. The values of the parameters are in Fig. 1.

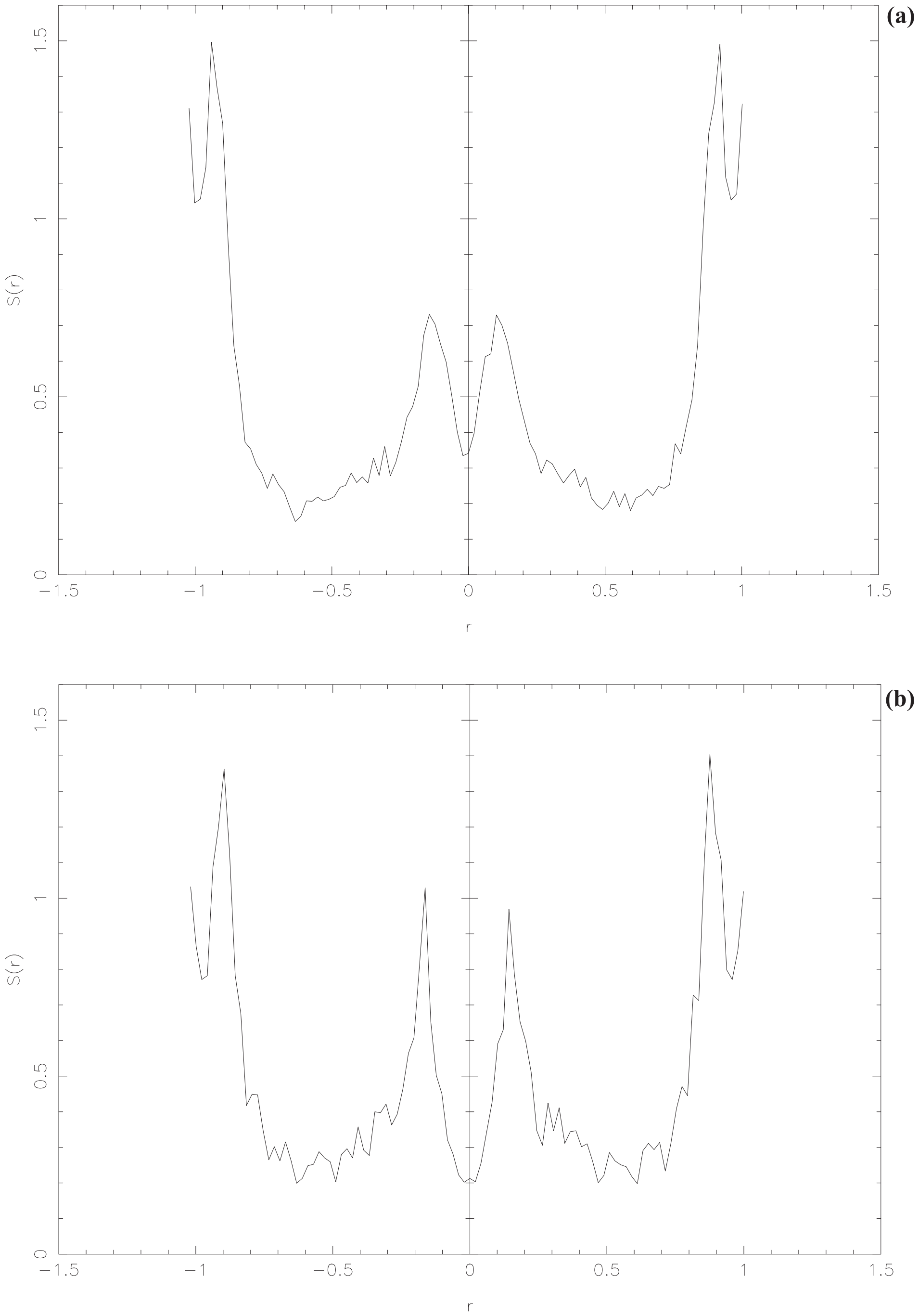

Figure 9 (a and b)**.** (*Continued*).

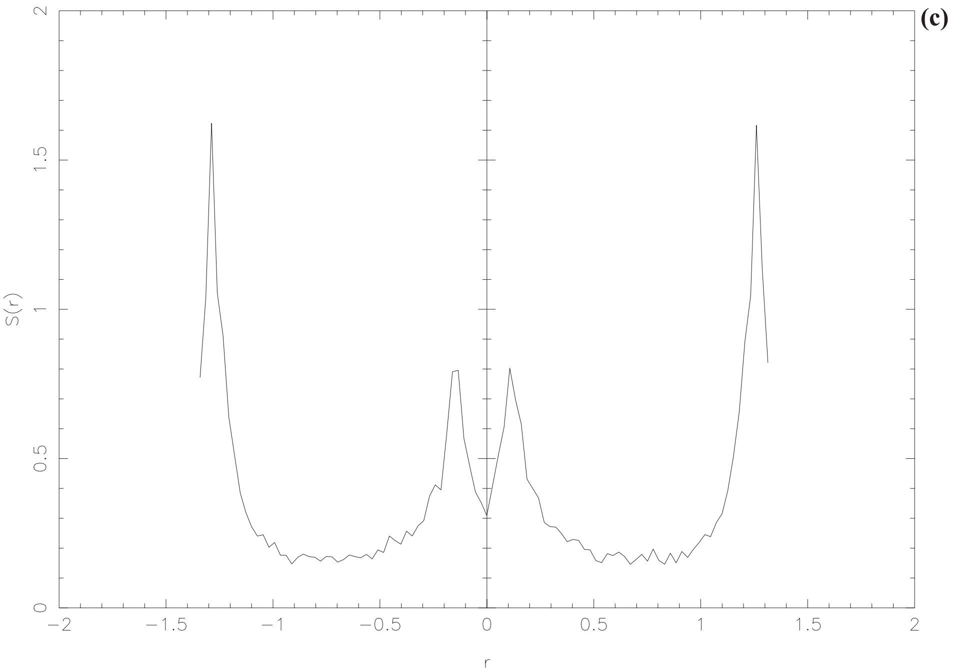

Figure 9 (a–c). The $S(r)$ spectrum for a chaotic orbit described in text. **(a)** Numerical integration; **(b)** Symplectic integrator; **(c)** Map. The values of the parameters are $\epsilon = 0.30$, $h = 2$, $\alpha = -1.5$, $\beta = 0.1$.

5. Discussion

In this paper we have studied the properties of orbits in the Hamiltonian system (equation 2) which can be considered to describe motion in the central parts of an elliptical galaxy. In order to obtain our results we have used the $x - p_x$ phase plane, which was obtained using three different numerical methods, that is conventional numerical integration, symplectic integrator and a map based on the averaged Hamiltonian. The conventional numerical integration was made using a Bulirsh–Stoer method in double precision and the accuracy of the calculations was checked by the constancy of the energy integral which was conserved up to the fifteenth significant figure.

If we accept the idea that the results of the conventional numerical integration are those displayed by the real system, then the symplectic integrator and the map give similar results, when small values of the perturbation parameter ϵ are used. For large values of the perturbation parameter, the phase plane derived by the symplectic integrator is similar to that found by conventional numerical integration, while that obtained by the map shows some differences mainly near the separatrix, where chaotic regions are observed.

Given the above, one concludes, that for weak perturbations one must prefer the map which gives fast results as well as additional analytical results for the position of the periodic orbits. For large perturbations, it is better to use the symplectic integration because it gives results similar to those given by conventional numerical integration but it is generally faster than numerical integration.

Symplectic integrators are very useful in many problems in Solar System Dynamics, where fast and accurate integrations algorithms are needed (see Saha and Tremaine 1992 and references therein). Experience gained from this research suggests that the symplectic integrator does a very good job in galactic dynamics as well. The authors are not aware of any other similar comparative study published before.

In order to see the behaviour of orbits from another point of view and to compare the corresponding results obtained by the three different methods, we decided to find the $S(r)$ spectrum for a number of orbits. Our numerical calculations show that the spectra, obtained by all three methods, corresponding to regular motion, that is box orbits producing invariant curves closing around the central invariant point, are very similar. On the other hand for island and chaotic motion there are some differences in the corresponding spectra. Anyway, for island and chaotic motion, the spectra derived using the symplectic integrator seem to be closer to those derived by conventional numerical integration than to those obtained by the map.

Acknowledgement

The authors would like to thank the referee for very useful suggestions and comments.

References

Byun, Y. I. *et al.* 1996, *AJ*, **111**, 1818.
Caranicolas, N. D. 1990, *Cel. Mech.* **47**, 87.
Caranicolas, N. D. and Innanen, K. A. 1992, *Astron. J.* **103**, 1308.
Caranicolas, N. D., Vozikis, Ch. 1999, *Astron. Astrophys.* **349**, 70.
Elipe, A., Deprit, A. 1999, *Mech. Res. Com.* **26**, 635.
Elipe, A. 2001, *Math. Comp. Sim.*, **57**, 217.
Feng, K. and Qin, M. In: *Lecture notes in mathematics*, Vol. **1297** (Springer, Berlin, 1987) pp. 1–37.
Karanis, G. I., Caranicolas, N. D. 2002, *Astron. Nach.* **323**, (1), 3.
Saha, P., Tremaine, S. 1992, *AJ*, **104,** 1633.

J. Astrophys. Astr. (2003) **24,** 99–109

The Mass/Eccentricity Limit in Double Star Astronomy

J. Dommanget *Observatoire Royal de Belgique, 3, avenue Circulaire, B-1180 Bruxelles, Belgique.*

Received 2003 July 30; accepted 2003 October 3

Abstract. A research that we conducted in 1963 on the evolution of the binaries based on the available orbital data to obtain a philosophical degree, led to the establishment of an interesting and new diagram between the logarithm of the total mass and a particular parameter X, bound to the areal constant. This appeared to have a real physical significance but the basic observational material was insufficiently extended to assure its undeniable existence. In 1981, a new research based on a more extended orbital material, has confirmed this diagram. Presently, another important increase in the orbital material and the availability of highly accurate trigonometric parallaxes produced by the Hipparcos satellite, gave us the opportunity to confirm once more the stability of this diagram. This last research is here described.

Key words. Stellar evolution—statistics—binaries.

1. First research

The discovery by W. Doberck in 1878, of a *period/eccentricity* correlation amongst the visual double star orbits caught the attention of many astronomers. In 1910, a similar correlation was shown amongst the spectroscopic orbits by W. W. Campbell (1910), H. Ludendorff (1910), Fr. Schlesinger and R. H. Baker (1910), extending the known visual correlation towards the small periods. But the global correlation covering altogether the visual and spectroscopic orbits has been later particularly debated, since the various selection effects existing in the statistical material that appeared were able to explain the observed phenomenon.

Nevertheless, despite the substantial and regular increase of the observational material with time (Fig. 1), the stability of the "plotting" of the correlation appeared evident (J. Dommanget 1963, 1964). It incited us to believe in its reality and to try to explain it from a new and original point of view: *the evolution of the double systems under the effect of a secular mass-loss*.

We started from the principle that in the two bodies problem, if there exists a secular and *isotropic* mass-loss, the gravitational force between the two bodies even when decreasing, remains central and the areal constant is conservative. We thus considered this areal constant as the invariable parameter allowing to characterize each binary during its evolution.

To realize this research, we have established a file of the orbits of 212 visual pairs and 98 spectroscopic ones selected for their quality.

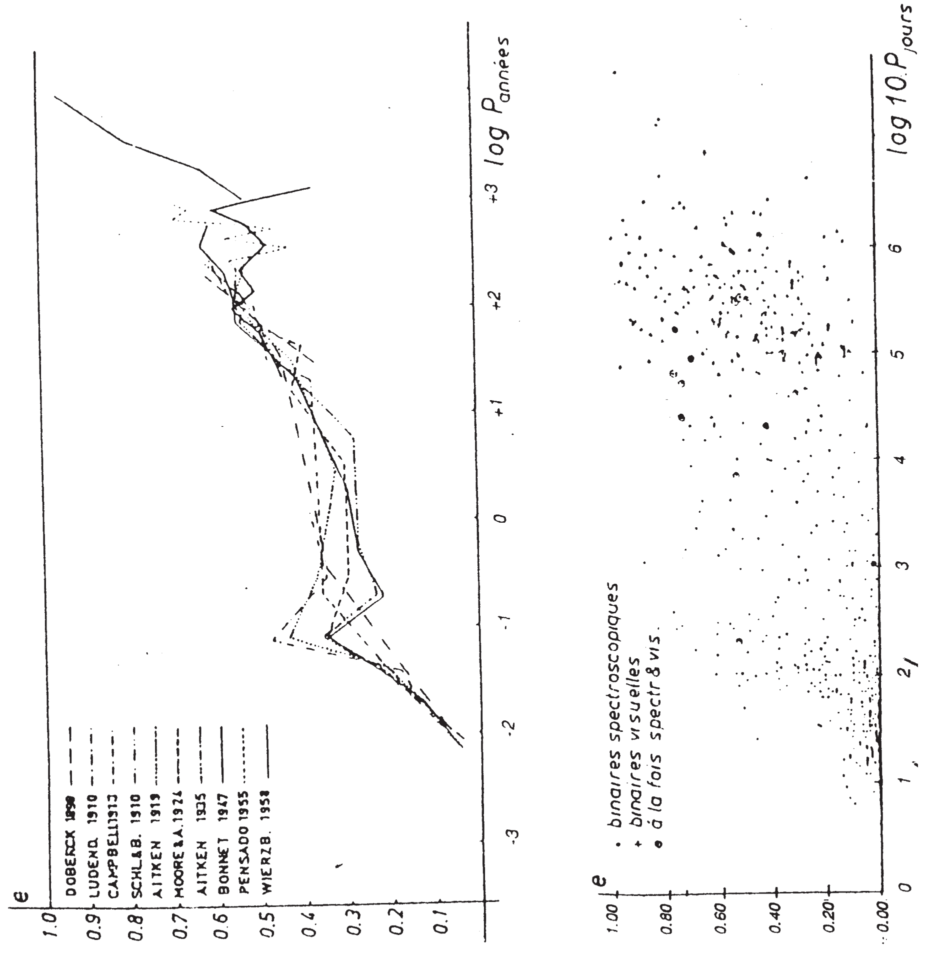

Figure 1. Successive period-eccentricity correlations proposed by various authors from 1898 to 1958.

The ignorance of trigonometric or spectroscopic parallaxes for many of these systems – essential for the computation of the semi-axis major and thus of the areal constant in astronomical units – has been the most important stumbling-block.

In order to evade this difficulty, we systematically used the dynamical parallaxes because they are available for each orbit and because they have a uniform accuracy *independent of their distance*, being uniquely based on the period, the semi-axis major and, through the mass-luminosity relation, on the apparent magnitude and the spectral classification.

We then discovered a particular distribution (Fig. 2) seeming to exist between the logarithm of the total mass: $\log \mathcal{M}_{AB}$ and the expression $X = \log P - 3 \log C$ which may be written

$$X = -2 \log \mathcal{M}_{AB} - 1.5 \log(1 - e^2) - 3 \log 2\pi, \tag{1}$$

the areal constant being

$$C = 2\pi A^2 (1 - e^2)^{1/2} / P. \tag{2}$$

This result allowed us to conceive an orbital evolution due to mass-loss, from the systems having short period and little eccentricity towards those having large period and showing larger eccentricity. The period-eccentricity correlation should thus have been explained.

2. Second research

Twenty years later, the availability of a more extended visual material (551 visual orbits) confirmed this result (Dommanget 1981) and has permitted definition of the *boundary* limiting the region of the stellar systems in the diagram ($\log \mathcal{M}_{AB}/X$) by the equation

$$e^{2.8} \mathcal{M}_{AB} = 3.60. \tag{3}$$

Its tracing is represented in Fig. 3 and goes along the points given in Table 1.

Table 1.

e	$\log \mathcal{M}_{AB}$	X
0.4	1.67	−5.62
0.5	1.40	−5.00
0.6	1.18	−4.45
0.7	0.99	−3.93
0.8	0.83	−3.39
0.9	0.68	−2.67
0.95	0.62	−1.04
0.96	0.606	+0.48

In this second research, the parallaxes once more have been the dynamical parallaxes for the same reasons as explained before.

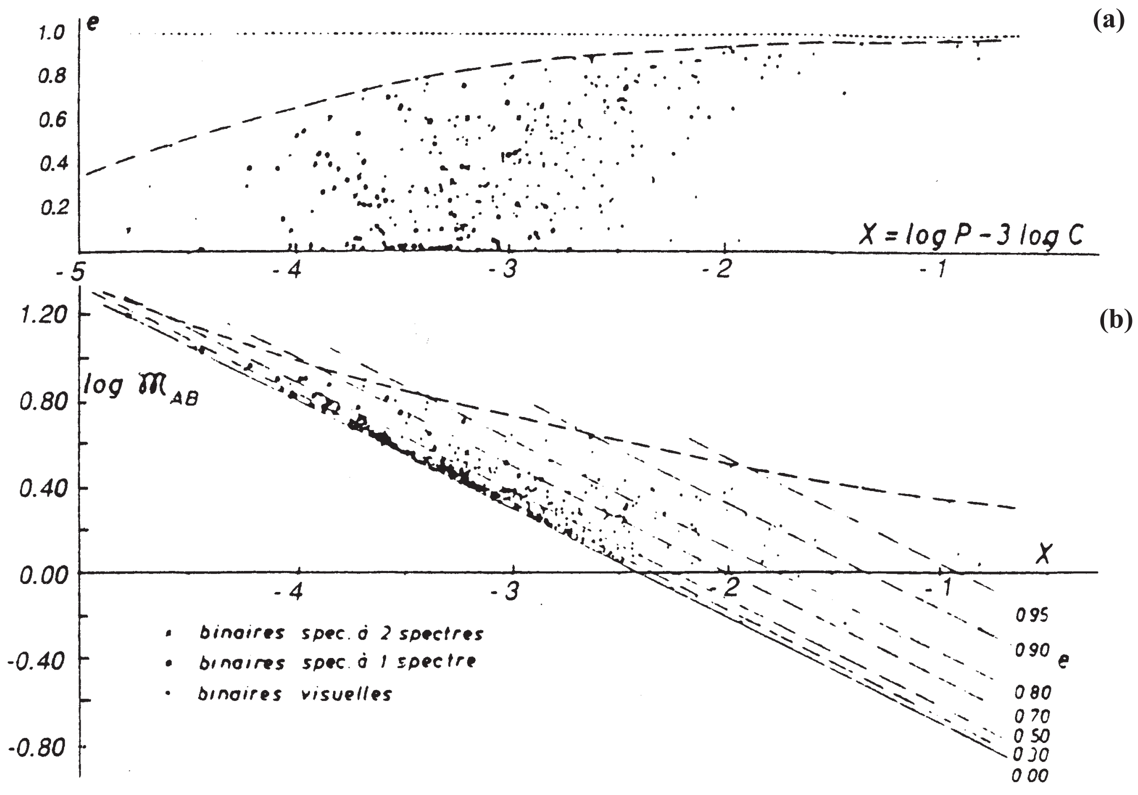

Figure 2. Diagrams representing on the basis of the orbital material available in 1963: **(a)** the eccentricity (e) as a function of the X parameter and **(b)** the $\log \mathcal{M}_{AB}$ values as a function of this same parameter (Dommanget 1963).

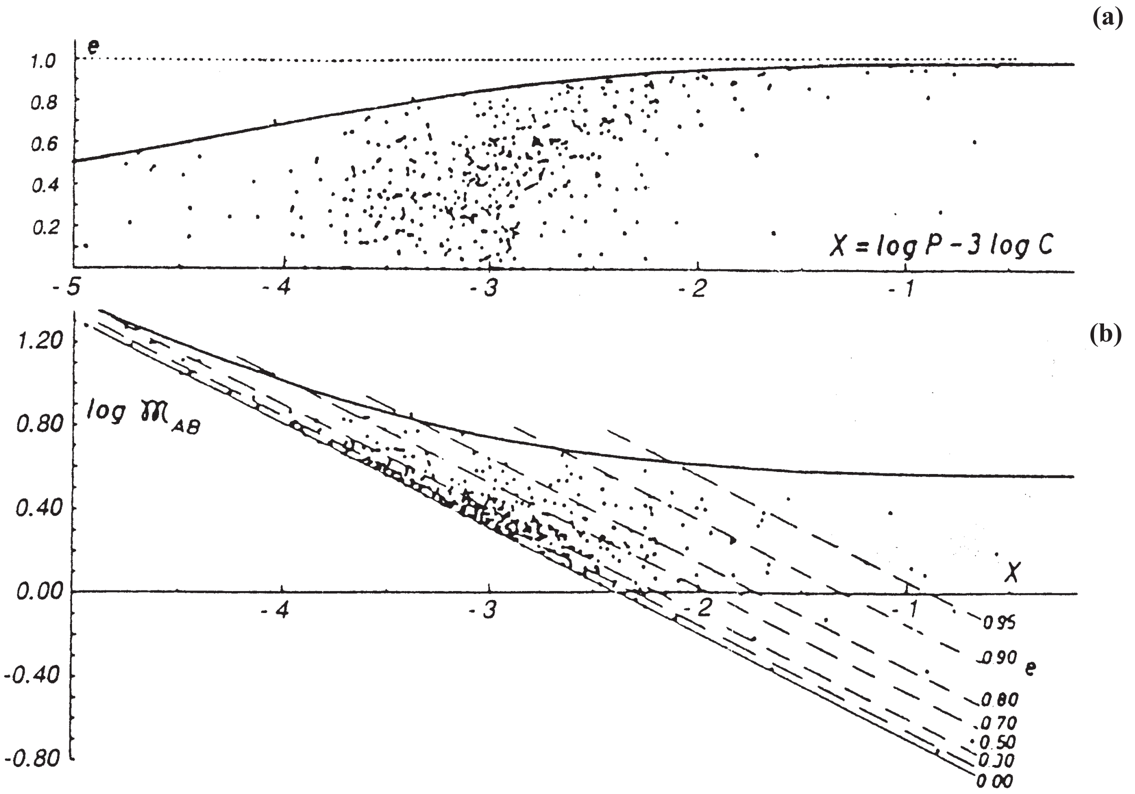

Figure 3. Diagrams representing on the basis of the orbital material available in 1981: **(a)** the eccentricity (e) as a function of the X parameter and **(b)** the $\log \mathcal{M}_{AB}$ values as a function of this same parameter (Dommanget 1981).

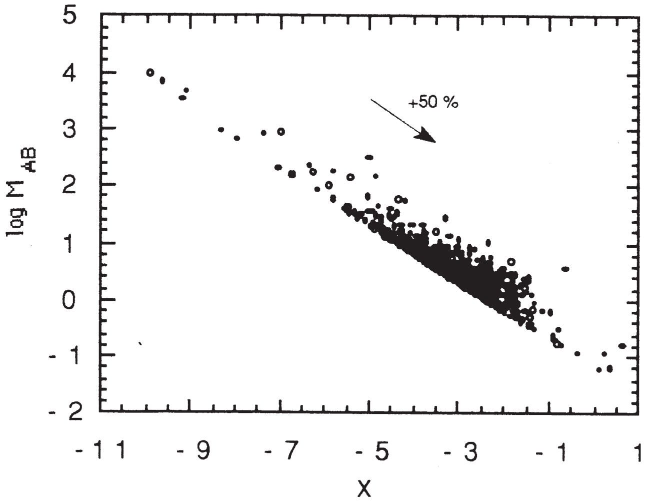

Figure 4. The arrow represents the displacement of the representing point due to an error of $+50\%$ on the parallax.

3. Third research

Now, another two decades later, it appeared essential to verify whether the new available orbital material would again confirm this result. This material now contains 1.471 visual binaries (5th catalogue of the USNO, 2001) of which 1.341 have parallaxes (not negative!) observed by Hipparcos (ESA, 1997). When eliminating the astrometric pairs (code 9 in the catalogue) because they do not permit a correct computation of the areal constant as well as of their total mass (*photocentric* semi axis-major), there remains a file of 1.120 orbits leading to the diagram of Fig. 4.

A quick look at this diagram shows that this file should be considered with great caution. It contains for instance systems having unacceptable masses reaching some 100 to more than 1000 solar units ($\log \mathcal{M}_{AB} > 2.0$) probably because too important relative errors on often too small parallaxes or in some cases because unsatisfactory orbital elements. These cases had of course to be rejected.

To eliminate the systems of which parallaxes are too inaccurate, one could either retain only those at less than 100 parsecs, the errors on π remaining then in general less than 20%, or suppress those individually showing errors superior than 20%. One should remark that an error such as $+50\%$ – classical for many cases of our file – leads to a displacement of the position of the representing point in the diagram ($\log \mathcal{M}_{AB}$,X) simultaneously of -0.65 in $\log \mathcal{M}_{AB}$ and of $+1.30$ in X. Such a displacement is illustrated by the arrow seen in the upper part of Fig. 4.

As a matter of fact a variation $d\pi$ in the parallax, gives by differentiating the expression of the logarithm of the total mass

$$d \log \mathcal{M}_{AB} = -3 \times 0.4343\, d\pi/\pi = -1.30 \times d\pi/\pi. \tag{4}$$

To eliminate the prohibitive systems, we finally adopted the limit of 20% because it allows to eliminate the most flagrant cases when simultaneously it tolerates keeping an extended file of some 897 cases (when keeping the systems at less than 100 parsecs, the file contains only 708 cases). The resulting diagram is given in Fig. 5.

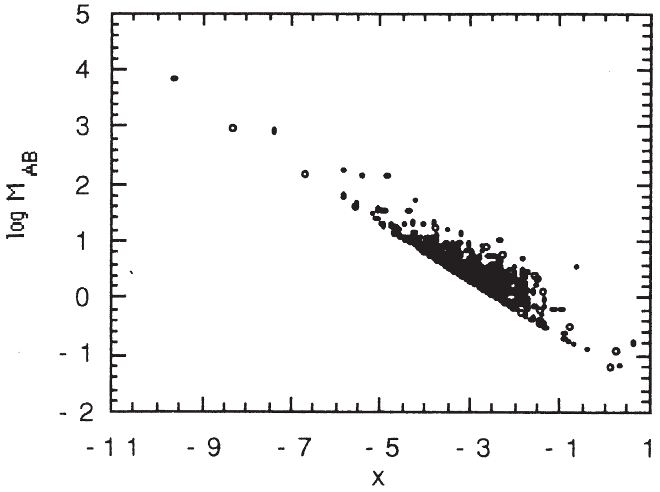

Figure 5. Identical diagram as that of Fig. 4 after suppressing the systems showing an error on the parallax larger than 20%.

Now, in order to permit a valuable comparison with our preceeding results only based on orbits of good quality and *satisfying the mass-luminosity relation* (dynamical parallax) we only retained those satisfying this propriety at best. Therefore, we thought we would characterize this quality by comparing the absolute magnitudes of the components computed by the direct way (parallaxes and apparent magnitudes) to those obtained through the use of the orbital elements (P and a) and the concerned relation. The more these values are near each other the more coherent are the observational data and this relation.

The considered equations are the following

(1) by the "direct" way (parallax and apparent magnitudes)

$$M_d = m + 5 + 5 \log \pi, \tag{5}$$

(2) by the "orbital" way (orbit and mass-luminosity relation)
computation of $\mathcal{M}_{AB}$ by the third law of Kepler,
computation of the mass ratio by the relation

$$\log \mathcal{M}_B/\mathcal{M}_A = -a.\Delta M_{\text{bol}}, \tag{6}$$

(with $a = 0.1117^*$)
computation of the individual mass of component A by

$$\mathcal{M}_A = \mathcal{M}_{AB}/(1 + \mathcal{M}_B/\mathcal{M}_A), \tag{7}$$

and computation of its absolute magnitude by

$$M_o = M_{\text{bol},A} - C_A = 4.77 - 8.9525 \log \mathcal{M}_A - C_A. \tag{8}$$

---

[*] Coefficient of the Baize-Romani mass-luminosity relation (1943): $\log \mathcal{M} = -0.1117(M_{\text{bol}} - 4.77)$. (Any other recent relation does not carry along any noticeable difference in the computations).

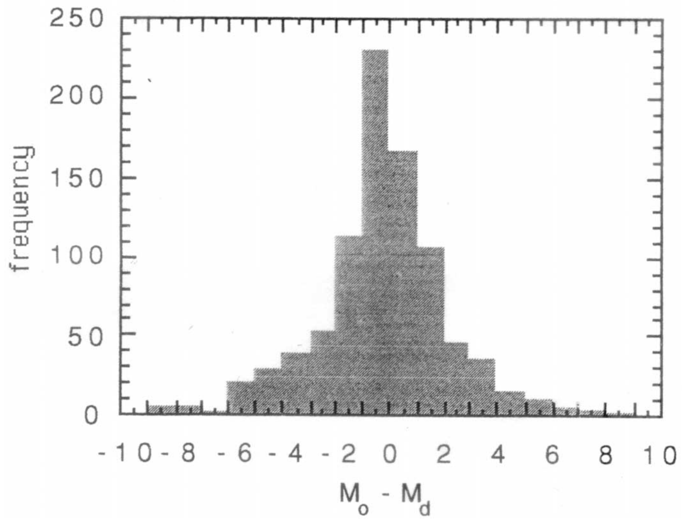

Figure 6. Distribution diagram of the differences $M_o - M_d$ for our finally 897 retained orbits.

C_A being the bolometric correction following Baize (1943). In view of a rough computation and because of the always too many unknown spectral classes for the individual components, we neglected the bolometric correction which in any case generally does not exceed 2 magnitudes. Moreover, we have only taken into account the results found for the principal component.

The difference between these two values of the absolute magnitude may be considered as a parameter of the coherence between the orbital and spectrophotometric data for each case. The histogram of Fig. 6 shows the distribution of the values of this difference for the 897 orbits of our file.

One may see that these are practically all – as absolute values – less than 10 magnitudes. But it appears evident that values of this order are prohibitive and that the smaller they are, the more confident we may be in their corresponding cases. The problem thus consists in choosing the most judicious limiting value for ΔM.

Having tried various values in decreasing the order such as: $\Delta M < 6$ magnitudes (Fig. 7(a) – 858 cases); $\Delta M < 4$ magnitudes (Fig. 7(b) – 784 cases) and $\Delta M < 2$ magnitudes (Fig. 7(c) – 613 cases), we concluded to an acceptable agreement for this last value between the distribution of the representative points and the curve of equation (3) previously found, if we eliminate some *non double* systems in view to be in the same conditions we imposed in our two preceeding researches.

We recall that the selection of the orbits has thus very similarly been made in 1963, 1981 and 2003:

- choice of the best available parallaxes (dynamical in 1963 and 1981; absolute and trigonometric from Hipparcos in 2003);
- orbital elements in agreement with the mass-luminosity relation (dynamical parallaxes in 1963 and 1981; coherence between direct and orbital absolute magnitude in 2003);
- elimination of the known multiple systems.

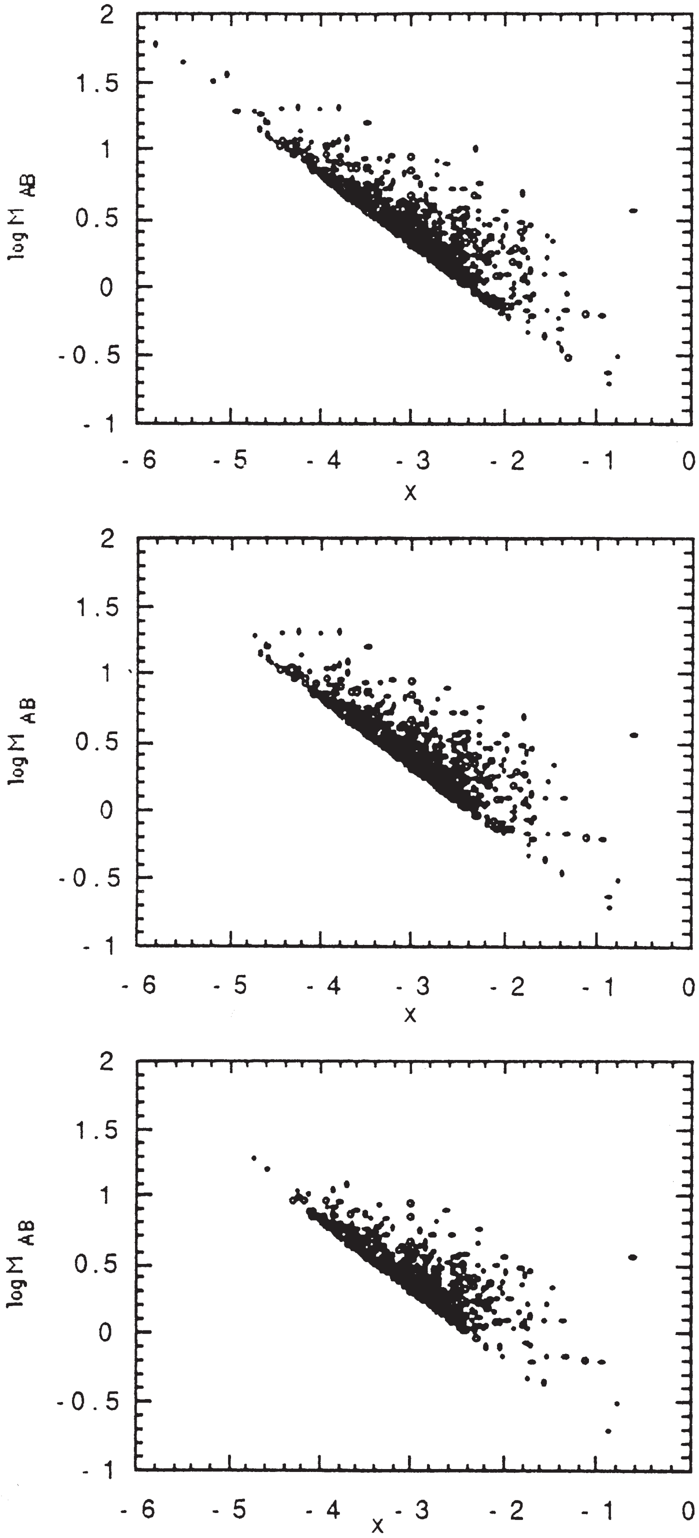

Figure 7. Diagrams respectively obtained with the conditions $\Delta M < 6$, $\Delta M < 4$, $\Delta M < 2$.

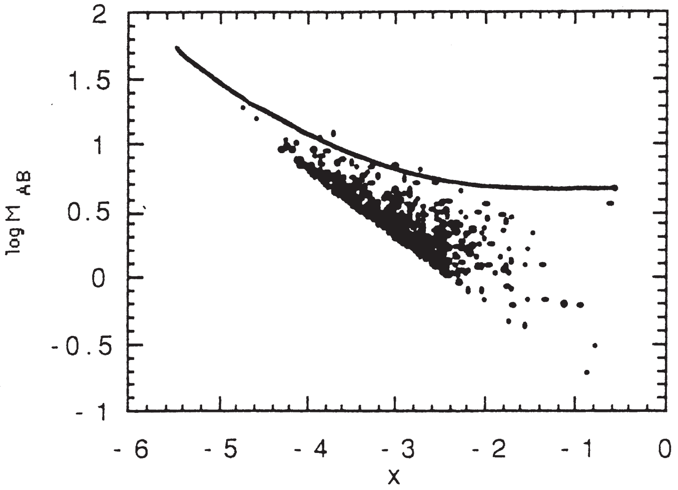

Figure 8. Diagram showing for the actual material, the values of $\log \mathcal{M}_{AB}$ as a function of the parameter X (to be compared with the diagrams of figures 2b and 3b).

Doing so, we found the diagram of Fig. 8 where the "boundary" could be expressed by equation

$$e^{3.40}\mathcal{M}_{AB} = 3.60, \tag{9}$$

to be compared with equation (3) which is practically identical in drawings.

Actually, its plotting goes then along the points given in table 2.

Table 2.

e	$\log \mathcal{M}_{AB}$	X
0.470	1.67	−5.57
0.565	1.40	−4.94
0.655	1.18	−4.39
0.745	0.99	−3.85
0.831	0.83	−3.29
0.920	0.68	−2.54
0.958	0.62	−2.01
0.967	0.606	−1.83

4. Conclusion

Neither the increase of the number of the computed orbits, nor the "switch" from the dynamical parallaxes to the trigonometric ones produced by Hipparcos seems to have perceptively modified their distribution in the diagram ($\log \mathcal{M}_{AB}$, X). The boundary expressed by equation (9) appears more and more to have a real physical significance which should thus be considered in any research about the evolution of the binaries *even if it is not based on a secular and isotropic mass-loss.*

5. Acknowledgement

We are much grateful to our colleague Thierry Pauwels for his help.

References

Baize, P. 1943, Les masses des étoiles et la relation empirique masse-luminosité; *L'Astronomie*, **57,** p. 101.

Campbel, W. W. 1910, Second catalogue of spectroscopic binary stars; *Lick Observatory Bulletin*, **6,** p. 17.

Doberck, W. 1878, On double star orbits; *Astronomische Nachrichten*, **91,** p. 317.

Dommanget, J. 1963, Recherches sur l'évolution des étoiles doubles par voie statistique et par application de la mécanique des masses variables; *Annales de l'Observatoire Royal de Belgique, 3*$^{\text{me}}$ *série, IX, fasc.* **1,** pp. 92.

Dommanget, J. 1964, Les étoiles doubles et l'évolution stellaire; *Ciel et Terre*, **80,** 9–10, pp. 315–338; *Comm. de l'Obs. R. de Belg.*, n$^{\text{o}}$ 232.

Dommanget, J. 1981, Is this diagramme an argument for binary orbital evolution? *Colloque UAI n*$^{\text{o}}$ 59, pp. 507–513; *Comm. de l'Obs. R. de Belg., Série B*, 119.

ESA. 1997, The Hipparcos and Tycho Catalogues, European Space Agency, SP 1200 (17 volumes).

Ludendorff, H. 1910, Zur Statistik der spektroskopischen Doppelsterne; *Astronomische Nachrichten*, **184,** p. 373.

Schlesinger, Fr., Baker, R. H. 1910, A comparative study of spectroscopic binaries; Publication of the Allegheny Observatory, **1,** p. 135.

USNO 2001, Double star CD, ORB5/ = Fifth Catalog of Orbits of Visual Binary Stars.